

INVESTIGATION OF PLASMON-POLARITONS AND PHONON-POLARITONS IN HEXAGONAL
BORON NITRIDE / METAL NANOPATTERN LAYERED DEVICES

by

DERMOT JIM THOMAS HENEGHAN

(Under the Direction of William Michael Dennis)

ABSTRACT

Plasmon-polaritons and phonon-polaritons and their interactions are investigated in a suite of devices that combine a hexagonal boron nitride (hBN) thin film with a nanopatterned metal film in a layered structure. Thin hBN layers have been shown to support highly confined hyperbolic phonon-polaritons that propagate with a low group velocity, making them of interest for light guiding and sensor applications. Localized plasmon resonances in nanopatterned metal films can exhibit subwavelength-scale confinement as well as a high local field strength that is of import to imaging and sensor applications. Three device geometries were investigated in this dissertation: (i) an hBN layer on a nanopatterned square array of cross apertures in a gold layer; (ii) an hBN layer on a nanopatterned hexagonal array of circular apertures in a silver layer; (iii) an hBN layer on a nanopatterned square array of gold crosses separated from a ground plane by a dielectric spacer. The interaction of these devices with infrared radiation was investigated using electromagnetic simulations that utilize the Finite-Difference Time-Domain (FDTD) method. Both far-field and near-field properties were calculated and analyzed, enabling the features due to plasmon-polaritons and phonon-polaritons, individually, to be distinguished and the coupling between these excitations to be explored and characterized.

INDEX WORDS: Plasmonics, Metamaterials, Hexagonal Boron Nitride (hBN), Plasmons, Phonons, Polaritons, Plasmon-Polaritons, Phonon-Polaritons, Perfect Absorber, Computational Electrodynamics, Transfer Matrix Method, Finite-Difference-Time-Domain (FDTD) Method, Graphical Processing Unit (GPU) Acceleration

INVESTIGATION OF PLASMON-POLARITONS AND PHONON-POLARITONS IN HEXAGONAL
BORON NITRIDE / METAL NANOPATTERN LAYERED DEVICES

by

DERMOT JIM THOMAS HENEGHAN

B.Sc., University of Limerick, 2008

M.Sc., University of Limerick, 2011

A Dissertation Submitted to the Graduate Faculty
of The University of Georgia in Partial Fulfillment

of the

Requirements for the Degree

DOCTOR OF PHILOSOPHY

ATHENS, GEORGIA

2022

© 2022

Dermot Jim Thomas Heneghan

All Rights Reserved

INVESTIGATION OF PLASMON-POLARITONS AND PHONON-POLARITONS IN HEXAGONAL
BORON NITRIDE / METAL NANOPATTERN LAYERED DEVICES

by

DERMOT JIM THOMAS HENEGHAN

Major Professor: William Michael Dennis

Committee: Michael Geller
Heinz-Bernd Schüttler

Electronic Version Approved:

Ron Walcott
Vice Provost for Graduate Education and Dean of the Graduate School
The University of Georgia
May 2022

Dedication

To those that helped me along the way

Acknowledgments

To the friends I made in the UGA Ultimate Frisbee Club. You provided an outlet for a wide variety of my extracurricular ambitions. Many of you invited me into your homes and lent me your parents for a few hours. Thank you to those who let me coach them. Coaching the UGA C team was rewarding in a way I never anticipated. I am proud of each of you.

To my friends. The Blind Pig crew, an immensely supportive group of men who made me feel there would always be a net below me. Mike Hurley and my fellow alumni of 13 The Park, thank you for providing a tether to the ground, a structure of support and the discretion to know which was needed. To the gamers both in Limerick and Athens thank you for the healthy social environment. Those I made in the Athens and Jersey City service industry. You provided a needed perspective of the world outside the Physics building.

The UGA Department of Physics and Astronomy for the support *in* the Physics building. My fellow graduate students. Thank you for the support and friendship during this shared experience.

To my family. My sisters thank you for providing support during the hardest times and cheering me on as I approach the finish. My parents, thank you for the support. I am grateful for the wisdom provided.

Finally thank you to my advisor Bill Dennis. A scientist who saw my potential under the unfinished edges. Having someone with a shared appreciation of *An Roinn Oideachais'* Mathematics Tables was always a comfort. Thank you for instilling the importance of professionalism and the value of getting the finer details correct.

Contents

Acknowledgments	v
1 Introduction	1
2 Methods	6
2.1 Introduction	6
2.2 Materials Models	11
2.3 Sources	18
2.4 Boundary Conditions	21
2.5 Sensors	27
2.6 Parallelization	29
2.7 In-House Code Design	31
2.8 Analysis Tools	33
3 Coupling of phonon-polaritons with plasmon-polaritons in a layered device comprising hBN on a nanopatterned square array of cross apertures in a Au layer	37
3.1 Introduction	37
3.2 Preliminary Measurements	39
3.3 Peak Finding	45
3.4 Far-Field Analysis	47

3.5	Near-Field Analysis	50
3.6	Conclusions	61
4	Coupling of phonon-polaritons with plasmon-polaritons in a layered device comprising hBN on a nanopatterned hexagonal array of circular apertures in a Ag layer	63
4.1	Introduction	63
4.2	Preliminary Measurements	64
4.3	Far-Field Analysis	71
4.4	Near-Field Analysis	73
4.5	Conclusions	81
5	Coupling of phonon-polaritons with plasmon-polaritons in a layered device comprising hBN on a nanopatterned square array of Au crosses suspended over a ground plane	84
5.1	Introduction	84
5.2	Preliminary Measurements	85
5.3	Far-Field Analysis	89
5.4	Near-Field Analysis	92
5.5	Conclusions	101
6	Conclusions	102
A	The Z-Transform	118

List of Figures

2.1	Diagram of the Yee Cell. The \mathbf{H} and \mathbf{E} components are offset in space by half a spatial step.	8
2.2	Real and imaginary fits of the Debye-Drude model (Eq. 2.13) to the wavelength dependent dielectric function data as tabulated in the supplemental materials of the paper by Ciesielski <i>et al.</i> [74]	16
2.3	Results published by Caldwell <i>et al.</i> , [13], showing the reflection spectra for various thicknesses of hBN. As can be seen the Lorentzian lineshape changes dramatically with variance in the thickness of the hBN layer due to a change in $\gamma_{x,y}(d_{\text{hBN}})$,	17
2.4	(a) Reflectance spectra for various thicknesses of hBN. The dots are digitized data from Caldwell <i>et al.</i> , [13], the solid lines are the spectra calculated using the transfer matrix method. (b) A log-log power law fit to the calculated values of $\gamma_{x,y}(d_{\text{hBN}})$, (c) Reflection, transmission and absorptance spectra for an infinite sheet of 80 nm thick hBN in a vacuum. These data were obtained using the Lorentz parameter $\gamma_{x,y}(d_{\text{hBN}})$ calculated in pane (b). The dark lines were calculated using the transfer matrix method while the bright lines were calculated using the in-house FDTD code developed for this dissertation.	19
2.5	Anatomy of a typical simulation used to calculate an absorptance spectrum.	29
2.6	Colormap figure produced for near-field analysis.	30
2.7	Visualization of the CPU and GPU processes for updating the Yee Grid.	31

2.8	A block diagram showing the steps taken during the main FDTD update loop.	32
2.9	Key steps taken to initialize the FDTD grid before the main FDTD update loop.	33
2.10	Key steps performed by the main in-house code.	34
2.11	(a) Planar view of a Au cross shaped aperture along the xy -plane. Field polarization is indicated by the black arrows. (b) Cross sectional view of the same structure displayed in pane along the yz -plane (a). Field polarization is indicated by the white arrows. Materials are differentiated by color. In this figure the tan represents PML, magenta represents hBN, gold represents Au, light blue represents SiO_2 , and black represents vacuum. Green and red lines indicate the positions of cross sectional and planar frequency domain colormaps respectively, of the kind displayed in Fig. 2.6.	35
2.12	(a) Imaginary E_y field lineout data from the device studied in Chapter 3. (b) The spatial Fourier transform of the data from pane (a)	36
2.13	Figure from Bylinkin <i>et.al.</i> , [82]. The imaginary component of the AFM measurements of an hBN ribbon over SiO_2 and the spatial Fourier transform of that data.	36
3.1	Frequency domain color map of hBN film atop of nanopatterned (a square array of holes) etched into a gold (Au) film which was deposited on a fused silica (SiO_2) substrate. The color scale in this figure is normalized to 0.25 the maximum $ \mathbf{E} $ value obtained from Fig. 3.2 (d), this was done in order to enhance the contrast.	38
3.2	Frequency domain color map of hBN film atop of nanopatterned (a square array of crosses) etched into a gold (Au) film which was deposited on a fused silica (SiO_2) substrate. The color scale in this figure is normalized to 0.25 the maximum $ \mathbf{E} $ value obtained from pane (d), this was done in order to enhance the contrast in Fig 3.2.	38

3.3 Schematic of the hBN/Au structure simulated in this chapter. (a) Planar view at the hBN/Au interface. (b) Cross-sectional view. CPML: Convolutional perfectly matched layer boundary conditions are imposed at the z -direction boundaries. Periodic boundary conditions are imposed at the x and y boundaries. The unit cell lengths in the x - and y - directions are d_x and d_y , respectively. The layer thicknesses are $d_{\text{VAC}} = 0.87 \mu\text{m}$, $d_{\text{hBN}} = 80 \text{ nm}$, $d_{\text{SiO}_2} = 1.0 \mu\text{m}$, $d_{\text{Au}} = 50 \text{ nm}$. The length of the long segments of the cross pattern is $l = 0.8 d_x = 0.8 d_y$ while the width of the cross is $w = 0.15 d_x = 0.15 d_y$. The distance between the centers of neighboring crosses is $d_{\text{CC}} = d_x = d_y$. The directions of the \mathbf{E} -field, \mathbf{H} -Field and propagation vector \mathbf{k} are shown in both panes.	43
3.4 The spectra for the BD at a range of d_{CC} values. (a) Reflectance spectra. (b) Transmittance spectra. (c) Absorptance spectra. The vertical black dashed lines in this figure indicate the position of the hBN TO and LO phonon frequencies, at $\omega_{\text{TO}} = 1370 \text{ cm}^{-1}$ and $\omega_{\text{LO}} = 1610 \text{ cm}^{-1}$, respectively.	44
3.5 The spectra for the UCDI at a range of d_{CC} values. (a) Reflectance spectra. (b) Transmittance spectra. (c) Absorptance spectra. The vertical black dashed lines in this figure indicate the position of the hBN TO and LO phonon frequencies, at $\omega_{\text{TO}} = 1370 \text{ cm}^{-1}$ and $\omega_{\text{LO}} = 1610 \text{ cm}^{-1}$, respectively.	45
3.6 The spectra for the CD at a range of d_{CC} values. (a) Reflectance spectra. (b) Transmittance spectra. (c) Absorptance spectra. The vertical black dashed lines in this figure indicate the position of the hBN TO and LO phonon frequencies, at $\omega_{\text{TO}} = 1370 \text{ cm}^{-1}$ and $\omega_{\text{LO}} = 1610 \text{ cm}^{-1}$, respectively.	46
3.7 The dependence of the plasmon resonance frequency on d_{CC} for the bare device (BD). A power law was fit to the data for the purpose of interpolation. The resulting fit was extremely close to linear.	47
3.8 Mode locations for the $d_{\text{CC}} = 3.15 \mu\text{m}$ CD.	48

3.9 (a) The absorptance spectrum of the BD for a range of d_{CC} values. (b) The absorptance spectra of the UCDI. (c) The absorptance spectra of the CD. The gray dotted curve in pane (c) depicts the absorption spectra for the UCDII with $d_{CC} = 3.14 \mu\text{m}$. The vertical black dashed lines in this figure indicate the position of the hBN TO and LO phonon frequencies as described in the main text.	50
3.10 (a) Absorptance spectra for the UCDI vs $\frac{2\pi}{d_{CC}}$ plotted as a color map. The symbols indicate the peaks in the absorptance spectra. The triangular symbols are due to Rayleigh anomalies, while the square symbols indicate the plasmon-polariton, which shifts linearly with $\frac{2\pi}{d_{CC}}$. (b) Absorptance spectra for the CD vs $\frac{2\pi}{d_{CC}}$ plotted as a color map. The symbols indicate the peaks/shoulders in the absorptance spectra. The triangular symbols are due to Rayleigh anomalies, while the square symbols show the interaction between plasmon-polariton in the nanopatterned Au film and the bulk phonon-polariton in the hBN. The interpretation of the features labeled by the circular symbols are given in the main text.	51
3.11 Background subtracted and normalized planar and cross-sectional colormaps of the field magnitude for the BD, UCDI, UCDII, and CD with $d_{CC} = 3.14 \mu\text{m}$. Panes (a) – (h) were excited below the reststrahlen band at $\nu = 1200 \text{ cm}^{-1}$. The white lines in the planar colormaps panes (a) – (d) indicate the location of the cross-sectional colormaps in (e) – (h). Panes (i) – (p) were excited in the reststrahlen band at $\nu = 1500 \text{ cm}^{-1}$. The white lines in the planar colormaps panes (i) – (l) indicate the location of the cross-sectional colormaps in (m) – (p). Panes (q) – (x) were excited above the reststrahlen band at $\nu = 1700 \text{ cm}^{-1}$. The white lines in the planar colormaps panes (q) – (t) indicate the location of the cross-sectional colormaps in (u) – (x).	53

3.12 (a) Lineouts of the magnitude of the electric field for a range of excitation frequencies in the reststrahlen band $\nu = 1490 - 1570 \text{ cm}^{-1}$. The circular dots indicate peaks in the lineout. (b) Dispersion curve constructed from the peak data in pane (a). (c) Lineouts of the y -component of the electric field for a range of excitation frequencies in the reststrahlen band $\nu = 1490 - 1570 \text{ cm}^{-1}$. The circular dots indicate peaks in the lineout. (d) Dispersion curve constructed from the peak data in pane (c). The inserts in panes (b) and (d) show the position of the lineouts in panes (a) and (c).	55
3.13 Phonon-polariton dispersion curves in the CD. (a) Black curve – lower scale: The far-field absorptance spectrum. Red curve – upper scale: The magnitude of the excitation field used to generate the data in the following panes. (b) E_y lineouts (at the position of the white lines in Fig. 3.11) for frequencies in the range $\nu = 1000 - 1800 \text{ cm}^{-1}$ with a spectral resolution of 1 cm^{-1} . The spatial extent of the data displayed in this pane is from the center to the edge of the unit cell to avoid duplication. The white dotted line in this pane indicates the boundary between vacuum and Au. (c) The spatial Fourier transform of the (full spatial lineout) data presented in pane (b). This data has been interpolated using a cubic spline algorithm. The resulting plot of $ E_y(q, \omega) $ enables the phonon-polariton dispersion curves to be visualized. The red and green theoretical dispersion curves are calculated as described in the text. The red dots are the dispersion curve data from Fig. 3.12 (b). (d) The spectral content of the data in pane (c) obtained by integrating over q	57

3.14 Vacuum/hBN/Vacuum/SiO ₂ and Vacuum/hBN/Au/SiO ₂ phonon-polariton signal strength and frequency dependence in the CDs as a function of d_{CC} . (a) The spatial Fourier transform of the Vacuum/hBN/Vacuum/SiO ₂ masked data from pane Fig. 3.13 (b). The green theoretical dispersion curves are for the Vacuum/hBN/Vacuum/SiO ₂ system. (c) The spatial Fourier transform of the Vacuum/hBN/Au/SiO ₂ masked data from pane Fig. 3.13 (b). The red theoretical dispersion curves are for the Vacuum/hBN/Au/SiO ₂ system. Pane (c) is the same as pane (a), but for the $d_{CC} = 3.94 \mu\text{m}$ device. Pane (d) is the same as pane (b), but for the $d_{CC} = 3.94 \mu\text{m}$ device. (e) Green: The integrated Vacuum/hBN/Vacuum/SiO ₂ phonon-polariton signal strength plotted as a function of d_{CC} . Red: The integrated Vacuum/hBN/Au/SiO ₂ phonon-polariton signal strength plotted as a function of d_{CC} . (f) Blue: The far-field absorptance spectra from Fig. 3.9 integrated over the spectral region of the reststrahlen band plotted as a function of d_{CC} . (g) Green: The frequency at which the peak of the Vacuum/hBN/Vacuum/SiO ₂ phonon-polariton signal strength occurs plotted as a function of d_{CC} . Red: The frequency at which the peak of the Vacuum/hBN/Au/SiO ₂ phonon-polariton signal strength occurs plotted as a function of d_{CC} . (h) Blue: The peak of the high frequency far-field absorptance band from Fig. 3.9. The lines in panes (e), (f), (g) and (h) are guides to the eye.	60
---	----

4.1 Schematic of the hBN/Ag structure simulated on this work. (a) Plane view at the hBN/Ag interface. The symmetry reduced unit cell is outlined in red. (b) Cross-sectional view. CPML: Convolutional perfectly matched layer boundary conditions terminated the z -direction boundaries. Periodic boundary conditions terminated the x and y boundaries. The unit cell lengths in the x - and y -directions are d_x and d_y , respectively. The layer thicknesses beyond the CPMLs were $d_{\text{VAC}} = 0.87 \mu\text{m}$, $d_{\text{hBN}} = 80 \text{ nm}$, $d_{\text{Si}} = 1.0 \mu\text{m}$, $d_{\text{Ag}} = 50 \text{ nm}$. The radius of the holes is $r_C = 0.68 \mu\text{m}$. The distance between the centers of the cylindrical holes is $d_{\text{CC}} = d_x$, $d_y = \sqrt{3}d_{\text{CC}}$. The directions of the \mathbf{E} -field, \mathbf{H} -Field and propagation vector \mathbf{k} is shown in both panes.	65
4.2 The spectra for the BD at a range of d_{CC} values. (a) Reflectance spectra. (b) Transmittance spectra. (c) Absorptance spectra. The vertical black dashed lines in this figure indicate the position of the hBN TO and LO phonon frequencies.	69
4.3 The spectra for the UCDI at a range of d_{CC} values. (a) Reflectance spectra. (b) Transmittance spectra. (c) Absorptance spectra. The vertical black dashed lines in this figure indicate the position of the hBN TO and LO phonon.	70
4.4 The spectra for the CD at a range of d_{CC} values. (a) Reflectance spectra. (b) Transmittance spectra. (c) Absorptance spectra. The vertical black dashed lines in this figure indicate the position of the hBN TO and LO phonon frequencies.	71
4.5 (a) The absorptance spectrum of the BD for a range of d_{CC} values. (b) The absorptance spectra of the UCDI. (c) The absorptance spectra of the CD. The vertical black dashed lines in this figure indicate the position of the hBN TO and LO phonon frequencies as described in the main text.	73

4.6 (a) Absorptance spectra for the UCDI as a function of $\frac{2\pi}{d_{CC}}$ plotted as a color map. The symbols indicate the peaks in the absorptance spectra. The triangular symbols are due to Rayleigh anomalies, while the square symbols indicate the plasmon-polariton, which shifts inversely to increases in d_{CC} . (b) Absorptance spectra for the CD as a function of $\frac{2\pi}{d_{CC}}$ plotted as a color map. The symbols indicate the peaks/shoulders in the absorptance spectra. The triangular symbols are due to Rayleigh anomalies, while the square symbols show the interaction between plasmon-polariton in the nanopatterned Au film and the bulk phonon-polariton in the hBN.	74
4.7 Background subtracted and normalized planar and cross-sectional colormaps of the $ E $ field with for the BD, UCDI, UCDII, and CD with $d_{CC} = 2.38 \mu\text{m}$. Simulations in this figure used an x -polarized source. Panes (a) – (h) were excited below the reststrahlen band at $\nu = 1200 \text{ cm}^{-1}$. The white lines in the planar colormaps panes (a) – (d) indicate the location of the cross-sectional colormaps in (e) – (h). Panes (i) – (p) were excited in the reststrahlen band at $\nu = 1500 \text{ cm}^{-1}$. The white lines in the planar colormaps panes (i) – (l) indicate the location of the cross-sectional colormaps in (m) – (p). Panes (q) – (x) were excited above the reststrahlen band at $\nu = 1700 \text{ cm}^{-1}$. The white lines in the planar colormaps panes (q) – (t) indicate the location of the cross-sectional colormaps in (u) – (x).	75

4.8 Background subtracted and normalized planar and cross-sectional colormaps
of the $|E|$ field with for the BD, UCDI, UCDII, and CD with $d_{CC} = 2.38 \mu\text{m}$.
Simulations in this figure used an x -polarized source. Panes (a) – (h) were
excited below the reststrahlen band at $\nu = 1200 \text{ cm}^{-1}$. The white lines in the
planar colormaps panes (a) – (d) indicate the location of the cross-sectional
colormaps in (e) – (h). Panes (i) – (p) were excited in the reststrahlen band
at $\nu = 1500 \text{ cm}^{-1}$. The white lines in the planar colormaps panes (i) – (l)
indicate the location of the cross-sectional colormaps in (m) – (p). Panes
(q) – (x) were excited above the reststrahlen band at $\nu = 1700 \text{ cm}^{-1}$. The
white lines in the planar colormaps panes (q) – (t) indicate the location of the
cross-sectional colormaps in (u) – (x).

77

4.9 (a) CD with $d_{CC} = 2.38 \mu\text{m}$ lineouts of the magnitude of the electric field for a
range of excitation frequencies in the reststrahlen band $\nu = 1490 – 1570 \text{ cm}^{-1}$.
(c) CD with $d_{CC} = 2.38 \mu\text{m}$ lineouts of the z -component of the electric field
for a range of excitation frequencies in the reststrahlen band $\nu = 1490 –$
 1570 cm^{-1}

78

4.10 Phonon-polariton dispersion curves in the CD with $d_{\text{CC}} = 2.38 \mu\text{m}$. (a) The far-field absorption spectrum. (b) E_z lineouts along the $y = 0 \mu\text{m}$ line for frequencies in the range $\nu = 1000 - 1800 \text{ cm}^{-1}$ with a spectral resolution of 1 cm^{-1} . The spatial extent of the data displayed in this pane is from the center to the edge of the unit cell to avoid duplication. The white dotted line in this pane indicates the boundary between vacuum and Ag. (c) The spatial Fourier transform of the (full spatial lineout) data presented in pane (b). This data has been interpolated using a cubic spline algorithm. The resulting plot of $|E_z(q, \omega)|$ enables the phonon-polariton dispersion curves to be visualized. The red and green theoretical dispersion curves are calculated as described in the text. (d) The spectral content of the data in pane (c) obtained by integrating over q .

5.1 Schematic of the hBN/Au structure simulated in this chapter. (a) Planar view at the hBN/Au interface. (b) Cross-sectional view. CPML: Convolutional perfectly matched layer boundary conditions are imposed at the z -direction boundaries. Periodic boundary conditions are imposed at the x and y boundaries. The unit cell lengths in the x - and y - directions are d_x and d_y , respectively. The layer thicknesses are $d_{\text{VAC}} = 0.62 \mu\text{m}$, $d_{\text{hBN}} = 80 \text{ nm}$, $d_{\text{Au}} = 0.1 \mu\text{m}$, $d_{\text{SiO}_2} = 0.196 \mu\text{m}$, $d_{\text{Gr}} = 0.1 \mu\text{m}$, $d_{\text{Si}} = 0.604 \mu\text{m}$. The length of the long segments of the cross pattern is $l = 0.8 d_x = 0.8 d_y$ while the width of the cross is $w = 0.16 d_x = 0.16 d_y$. The distance between the centers of neighboring crosses is $d_{\text{CC}} = d_x = d_y$. The directions of the \mathbf{E} -field, \mathbf{H} -Field and propagation vector \mathbf{k} are shown in both panes.	86
5.2 The spectra for the BD at a range of d_{CC} values. (a) Reflectance spectra. (b) Transmittance spectra. (c) Absorptance spectra. The vertical black dashed lines in this figure indicate the position of the hBN TO and LO phonon frequencies.	89
5.3 The spectra for the UCDI at a range of d_{CC} values. (a) Reflectance spectra. (b) Transmittance spectra. (c) Absorptance spectra. The vertical black dashed lines in this figure indicate the position of the hBN TO and LO phonon.	90
5.4 The spectra for the CD at a range of d_{CC} values. (a) Reflectance spectra. (b) Transmittance spectra. (c) Absorptance spectra. The vertical black dashed lines in this figure indicate the position of the hBN TO and LO phonon frequencies.	91
5.5 (a) The absorptance spectrum of the BD for a range of d_{CC} values. (b) The absorptance spectra of the UCDI. (c) The absorptance spectra of the CD. The vertical black dashed lines in this figure indicate the position of the hBN TO and LO phonon frequencies as described in the main text.	92

5.6	(a) Absorptance spectra for the UCDI as a function of $\frac{2\pi}{d_{CC}}$ plotted as a color map. The symbols indicate the peaks in the absorptance spectra. The square symbols indicate the plasmon-polariton, which shifts inversely to increases in d_{CC} . (b) Absorptance spectra for the CD as a function of $\frac{2\pi}{d_{CC}}$ plotted as a color map. The symbols indicate the peaks/shoulders in the absorptance spectra. The square symbols highlight the interaction between plasmon-polariton in the nanopatterned Au film and the bulk phonon-polariton in the hBN.	93
5.7	Background subtracted and normalized planar and cross-sectional colormaps of the field magnitude for the BD, UCDI, UCDII, and CD with $d_{CC} = 2.70 \mu\text{m}$. Panes (a) – (h) were excited below the reststrahlen band at $\nu = 1200 \text{ cm}^{-1}$. The white lines in the planar colormaps panes (a) – (d) indicate the location of the cross-sectional colormaps in (e) – (h). Panes (i) – (p) were excited in the reststrahlen band at $\nu = 1500 \text{ cm}^{-1}$. The white lines in the planar colormaps panes (i) – (l) indicate the location of the cross-sectional colormaps in (m) – (p). Panes (q) – (x) were excited above the reststrahlen band at $\nu = 1700 \text{ cm}^{-1}$. The white lines in the planar colormaps panes (q) – (t) indicate the location of the cross-sectional colormaps in (u) – (x).	94
5.8	(a) CD with $d_{CC} = 2.70 \mu\text{m}$ lineouts of the magnitude of the electric field for a range of excitation frequencies in the reststrahlen band $\nu = 1440 - 1510 \text{ cm}^{-1}$. (b) CD with $d_{CC} = 2.70 \mu\text{m}$ lineouts of the z -component of the electric field for a range of excitation frequencies in the reststrahlen band $\nu = 1440 - 1510 \text{ cm}^{-1}$. The circular dots indicate peaks in the lineout. (d) Dispersion curve constructed from the peak data in pane (c). The inserts in panes (b) and (d) show the position of the lineouts in panes (a) and (c).	96

5.9 Phonon-polariton dispersion curves in the CD with $d_{CC} = 2.70 \mu\text{m}$. (a) The far-field absorption spectrum. (b) E_z lineouts along the $x = 0 \mu\text{m}$ line for frequencies in the range $\nu = 1000 - 1800 \text{ cm}^{-1}$ with a spectral resolution of 1 cm^{-1} . The spatial extent of the data displayed in this pane is from the center to the edge of the unit cell to avoid duplication. The white dotted line in this pane indicates the boundary between vacuum and Au. (c) The spatial Fourier transform of the (full spatial lineout) data presented in pane (b). This data has been interpolated using a cubic spline algorithm. The resulting plot of $ E_z(q, \omega) $ enables the phonon-polariton dispersion curves to be visualized. The red and green theoretical dispersion curves are calculated as described in the text. (d) The spectral content of the data in pane (c) obtained by integrating over q .	97
---	----

5.10 Vacuum/hBN/Vacuum/SiO₂/Au/Si and Vacuum/hBN/Au/SiO₂/Au/Si phonon-polariton signal strength and frequency dependence in the CDs as a function of d_{CC} . (a) The spatial Fourier transform of the Vacuum/hBN/Vacuum/SiO₂/Au/Si masked data from pane Fig. 5.9 (b). The green theoretical dispersion curves are for the Vacuum/hBN/Vacuum/SiO₂/Au/Si system. (c) The spatial Fourier transform of the Vacuum/hBN/Vacuum/SiO₂/Au/Si masked data from pane Fig. 5.9 (b). The red theoretical dispersion curves are for the Vacuum/hBN/Vacuum/SiO₂/Au/Si system. Pane (c) and (d) are the same as pane (a) and (b), but for the $d_{CC} = 2.94 \mu\text{m}$ device. (e) Green: The integrated Vacuum/hBN/Vacuum/SiO₂/Au/Si phonon-polariton signal strength plotted as a function of d_{CC} . Red: The integrated Vacuum/hBN/Vacuum/SiO₂/Au/Si phonon-polariton signal strength plotted as a function of d_{CC} . (f) Blue: The far-field absorptance spectra from Fig. 5.5 integrated over the spectral region of the reststrahlen band plotted as a function of d_{CC} . (g) Green: The frequency at which the peak of the Vacuum/hBN/Vacuum/SiO₂/Au/Si phonon-polariton signal strength occurs plotted as a function of d_{CC} . Red: The frequency at which the peak of the Vacuum/hBN/Vacuum/SiO₂/Au/Si phonon-polariton signal strength occurs plotted as a function of d_{CC} . (h) Blue: The peak of the high frequency far-field absorptance band from Fig. 5.5. The lines in panes (e), (f), (g) and (h) are guides to the eye.

Chapter 1

Introduction

In this dissertation, plasmon-polaritons, phonon-polaritons and their interactions were investigated in a suite of structures that combine a hexagonal boron nitride (hBN) thin film with a nanopatterned metal film in a layered device.

Hexagonal boron nitride (hBN) is a technologically important material with the same structure as graphite. This interesting material exhibits excellent optical properties with potential for a wide range of optical device applications [1]. In particular, hBN layers have been shown to support highly confined phonon-polaritons that are of interest for light guiding applications [2]. Surface plasmon-polaritons are electromagnetic excitations that exist at the interface between a metal and a dielectric material, while localized plasmon resonances can exhibit subwavelength-scale confinement combined with a high local field strength and are of import to imaging and sensor applications [3, 4].

Polaritons are quasiparticles resulting from hybrid modes of photons and charge dipole excitations in crystalline structures [5]. The two most common types of polaritons are phonon-polaritons [5–7] and surface plasmon-polaritons [8], both of which are relevant to this study. First discovered by Ritchie in 1957 [9], plasmon-polaritons were observed to propagate along surfaces of conducting thin films [10]. These surface-plasmon-polaritons (SPPs) remain trapped on the surface due to resonant interactions with the free electrons of the conductor.

Of particular interest to this work are localized surface plasmon resonances, which can couple to a wide variety of nanoscale structures [11]. The confinement of radiation to scales below the diffraction limit has become the primary focus of modern nanophotonics [12, 13].

In order to develop scalable quantum-photonic technologies, on-chip integration of the photonic components is required. Such devices have applications in subwavelength imaging [14, 15], biosensing [16–18], thin film sensing [19] and quantum information [20–22]. After its discovery, much interest was shown in the study of graphene as a medium for tunable photon-plasmon coupling at the mid-infrared range [23]. However, in the second decade of this century there has been a rapidly increasing number of papers in the study of non-graphene two-dimensional materials [22]. In 2014, surface phonon-polaritons (SPPs) were observed in hexagonal boron nitride (hBN), these excitations exhibited higher confinement and lower losses than SPPs in graphene [24]. That same year Caldwell *et al.* demonstrated a strong confinement regime up to $\lambda/86$ [13]. This advantageous property is due to the hyperbolic nature of hBN’s permittivity tensor which contains oppositely signed principal components within the mid-infrared range [25]. While other artificial hyperbolic materials have been demonstrated, they suffer from higher losses and increased fabrication costs in comparison to natural hBN [26–28]. Since the phonons in hBN have excitation frequencies in the mid-infrared similar to the plasmons in graphene, hBN has the potential to be used in similar devices to those fabricated using graphene, for example, solar panels [29]. While hBN’s ability to endure temperatures up to 1773 K makes it a versatile material for high temperature applications [30, 31], this shared absorptance range also allows for graphene-hBN hetero-devices [32, 33]. Proximity effects due to layered hBN-graphene interactions have been shown to lead to the formation of secondary Dirac points [34–36]. Such properties are of use for breaking of time-reversal-symmetry [37–39], enabling the study of the quantum Hall effect [34–36], tunable superconductivity [39], and topological currents and states [40, 41]. Graphene’s high tunability allows such devices to couple into a greater spectral range, while hBN’s higher quality factor enables the transport of SPPs at a higher

efficiency with lower levels of damping [25, 33, 42, 43]. However, given the plasmon losses due to electron scattering by thermal phonons it is necessary to reduce dielectric losses by reducing damping [43].

One such solution for reducing this dielectric loss is to use a hetero device that incorporates a metallic diffraction grating underneath a hBN layer. Zhao and Zhang demonstrated near-perfect absorptance in hBN/metal gratings due to hyperbolic phonon-plasmon polariton coupling [44]. Recently Yang *et al.* [45] reported the coupling of phonon-polaritons between a hexagonal pattern of circular cavities in SiO₂. The experimental observations in this work used a diffraction grating constructed of a hexagonal pattern of holes in an Au film under an 80 nm thick layer of hBN and over a SiO₂ substrate. Up until recently it had been difficult to observe many of the finer near field spectral features of hBN devices due to lack of access to powerful broadband IR laser sources to effectively couple with optical phonons [45–47]. Recent work has shown scattering-type scanning near-field optical microscopy (s-SNOM) to be a powerful tool to observe, manipulate and quantify polariton coupling in hBN based heterostructures [19, 48]. Related studies investigating phonon-plasmon coupling using Fourier-transform infrared (FTIR) spectroscopy have been performed on polymethyl methacrylate (PMMA) [49, 50].

Optical metamaterials are artificially engineered periodic structures designed to exhibit optical properties not otherwise found in nature. Metamaterials have been used to realize applications such as negative refraction [51] and ultrahigh absorption [52]. Plasmonic metamaterials which support localized surface plasmon resonances can confine electromagnetic fields at a subwavelength scale, thereby enhancing the near-field coupling effects and light-matter interactions [49]. By varying geometrical parameters metamaterial devices have been shown to have highly tunable plasmonic resonances [53]. Coupling between plasmonic resonances and material phonon resonances through near-field interactions can give rise to a splitting of plasmon-phonon modes with anti-crossing behavior [54, 55]. Strong coupling can be controlled using the capacitance of metamaterial nanocavities [56]. Several studies

have been performed on hBN-metamaterial devices. These include arrays of hBN nanoparticles [13], an hBN sheet over a triangular lattice of circular apertures in SiO₂ [45], and hBN/metal-grating anisotropic structures [44].

In this dissertation, computer simulations were performed using the Finite-Difference Time-Domain (FDTD) method as detailed in Chapter 2. Initially proposed by Yee in 1966 [57] the popularity of this method has grown in parallel with the dramatic advances in computational power over the last several decades. In addition, the general applicability of the FDTD method enables a wide range of possible device specifications including feature size, pitch length, component material, and thickness to be simulated. The FDTD simulations reported in this dissertation provide detailed three-dimensional spatial information on the vector components of the electric fields within a series of multilayer (dielectric, hBN, metal) devices and enabled the coupling between plasmon-polaritons in the metallic layer and phonon-polaritons in the hBN layer to be investigated in detail.

Three classes of device geometries were investigated in this dissertation: (i) an hBN layer on a nanopatterned square array of cross apertures in a gold layer; (ii) an hBN layer on a nanopatterned hexagonal array of circular apertures in a silver layer and (iii) an hBN layer on a nanopatterned square array of gold crosses separated from a ground plane by a dielectric spacer. It was considered to be of primary importance that all these classes of devices be physically realizable. The hBN layer on a nanopatterned square array of cross apertures in a gold layer devices were selected because they exhibited smooth Gaussian-like absorption spectra with well separated Rayleigh anomalies in most cases as detailed in Chapter 3. The hBN layer on a nanopatterned hexagonal array of circular apertures in a silver layer devices were selected to emphasize how changes in symmetry, metallic layer and substrate impact the device performance. Furthermore, the circular aperture / hexagonal lattice symmetry acts as a prototype for multiple fascinating nanostructures that can be realized experimentally using shadow-sphere lithography [58]. Finally, the hBN layer on a nanopatterned square array of

gold crosses separated from a ground plane by a dielectric spacer devices are examples of an intriguing class of devices that exhibit near unity [59] or perfect absorptance [52, 60].

The organization of this dissertation is as follows: Chapter 2 reviews the Finite-Difference Time-Domain (FDTD) Method. The materials models used in this dissertation are described as is the implementation of the in-house GPU accelerated FDTD code. The steps taken to validate this code are also discussed. Chapter 3 describes the FDTD simulations performed on the class of devices that comprise an hBN layer on a nanopatterned square array of cross apertures in a gold layer. Chapter 4 describes the FDTD simulations performed on the class of devices that comprise an hBN layer on a nanopatterned hexagonal array of circular apertures in a silver layer. Chapter 5 describes the FDTD simulations performed on the class of devices that comprise an hBN layer on a nanopatterned square array of gold crosses separated from a ground plane by a dielectric spacer. In Chapters 3, 4, and 5, the FDTD method is used to investigate interaction of infrared radiation with the respective device classes in both the far-field and near-field regimes. Finally, Chapter 6 presents the conclusions of this dissertation.

Chapter 2

Methods

2.1 Introduction

Computational electromagnetics (CEM) is the process of modeling the interaction of electromagnetic fields with physical objects and environments. In most cases this involves using numerical methods to solve the Maxwell equations. For a subset of problems with specific geometric and electromagnetic properties exact analytical solutions can be found. However, for many non-symmetric structures or complex devices no such analytical solution exists. CEM methods provide solutions to electromagnetic problems which cannot be solved analytically. The transfer matrix method (TMM) [61] is one such method for analyzing the propagation of electromagnetic radiation through a stratified medium. This method is well established and relatively undemanding on computational resources. In this dissertation the method was very useful for the validation of material models and calculating model parameters during this dissertation. However, for devices lacking uniformity in more than one dimension the TMM is unable to provide solutions.

An alternate method is the finite element method (FEM). This method involves dividing the simulation space into a collection of finite spatial subdomains to form a mesh. The FEM solves the differential form of the Maxwell equations for each finite element of the mesh

by fitting a variational functional [62]. The FEM will select a functional with a minimum corresponding to a solution of the differential equation for that finite element. The equations are then recombined into a global system of equations for the final calculation. The FEM is able to handle more complex geometries than the TMM and is most often formulated in the frequency domain [63], although hybrid FEM-time-domain methods also exist. FEM is often used in the field of radio-frequency electromagnetics [63]. However, FEM meshes become very complex for large geometries, leading to slow convergence and long solution times [64].

Along with methods such as the TMM and FEM, several other popular CEM methods include the method of moments [65], the discontinuous time-domain method [66], and the pseudo-spectral spatial domain[67]. While these methods are effective, the FDTD method has a number of properties that were beneficial for simulating devices studied in this dissertation. The time-domain nature of FDTD, unlike it's frequency domain counterparts, allows for broadband simulation while also allowing for the portrayal of specific frequency responses in post processing analysis. The FDTD method is accurate, robust, and mature. Unlike the FEM, where the numerical complexity scales exponentially with spatial grid size, the FDTD method scales linearly [68]. The FDTD method has been used to simulate macro scale objects, such as low visibility aircraft, scattering radar waves, as well as smaller scale objects, such as cell phone signals interacting with human brain tissue and nano scale structures interacting with infrared scale wavelengths. Sources of error are well understood and methods have been developed to circumvent or account for these errors.

The Finite-Difference Time-Domain (FDTD) method uses the finite-difference approximation to discretize the differential operators in the Maxwell curl equations on a grid staggered in space and time. The \mathbf{H} and \mathbf{E} fields are computed on a regular grid using a leap-frogging in time approach. The \mathbf{H} and \mathbf{E} grids are offset by $\Delta k/2$ relative to each other as shown in Fig. 2.1, where $k = x, y, z$ and Δk is the spatial discretization in that dimension. The \mathbf{H} and \mathbf{E} grids are evaluated $\Delta t/2$ apart in time where Δt is the temporal discretization. This scheme provides second-order accuracy while using first-order numerical

differentiation. Initially proposed by Yee in 1966 [57], the popularity of the method has grown in parallel to the advances in computing over the last several decades. The time-domain nature of FDTD means that several frequencies of interest can be studied from a single simulation by using a broadband source. The FDTD method gives control over the parameter space to simulate a range of possible device specifications including feature size, electromagnetic source shape, and a wide range of material models. Another benefit of the leap-frogging algorithm for solving the \mathbf{H} and \mathbf{E} grids is it means the FDTD method is ideal for parallelization.

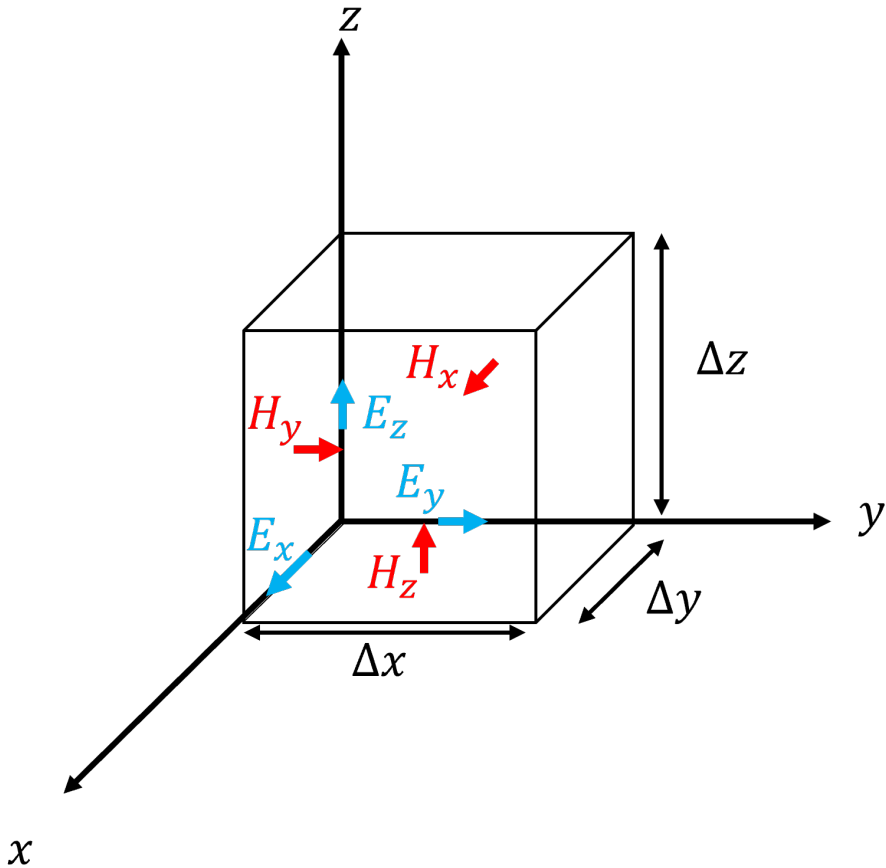


Figure 2.1: Diagram of the Yee Cell. The \mathbf{H} and \mathbf{E} components are offset in space by half a spatial step.

The formulation of the FDTD update equations begins with the Maxwell curl equations in the form

$$\nabla \times \mathbf{E} = -\frac{\partial \mathbf{B}}{\partial t}, \quad (2.1)$$

$$\nabla \times \mathbf{H} = \frac{\partial \mathbf{D}}{\partial t}. \quad (2.2)$$

The electric constitutive relation

$$\mathbf{D}(\omega) = \boldsymbol{\epsilon}(\omega) \cdot \mathbf{E}(\omega), \quad (2.3)$$

is also an important equation in the FDTD method. Through this equation the material models for a wide range of materials can be incorporated. Several examples of how this was accomplished in this dissertation are discussed later in this chapter. The magnetic constitutive equation

$$\mathbf{B}(\omega) = \boldsymbol{\mu}(\omega) \cdot \mathbf{H}(\omega), \quad (2.4)$$

is an important equation to consider for the formulation of the FDTD update equations. For all materials studied in this dissertation the relative magnetic permeability $\boldsymbol{\mu}_r(\omega) = \boldsymbol{\mu}(\omega)/\mu_0$ is essentially unity for the frequency ranges studied. This enabled the magnetic field times the permeability of free space to be substituted for the magnetic induction

$$\mathbf{B}(\omega) = \mu_0 \mathbf{H}(\omega), \quad (2.5)$$

in all cases. While many applications utilize the FDTD method derived from the Maxwell curl equations written in \mathbf{B} , when simulating non-magnetic materials it is best practice to include the relation in Eq. 2.4. This is done to reduce computational burden in terms of processing and memory requirements. In order to make \mathbf{D} and \mathbf{H} of comparable magnitude, \mathbf{E} and \mathbf{D} are scaled according to $\mathbf{E} \rightarrow \sqrt{\frac{\mu_0}{\epsilon_0}} \mathbf{E}$ and $\mathbf{D} \rightarrow \sqrt{\epsilon_0 \mu_0} \mathbf{D}$. This scaling removes a factor of ϵ_0 from the equations in the following sections.

Using the H_x field component as an example, the finite-difference approximation is applied to Faraday's law (Eq. 2.1) for a non-magnetic material is

$$\frac{H_x^{t+\frac{\Delta t}{2}}(x + \frac{\Delta x}{2}, y + \frac{\Delta y}{2}, z + \frac{\Delta z}{2}) - H_x^{t-\frac{\Delta t}{2}}(x + \frac{\Delta x}{2}, y + \frac{\Delta y}{2}, z + \frac{\Delta z}{2})}{\Delta t} \approx -c_0 \left(\frac{E_z(x, y + 1, z) - E_z^t(x, y, z)}{\Delta y} - \frac{E_y(x, y, z + 1) - E_y^t(x, y, z)}{\Delta z} \right), \quad (2.6)$$

where the (x, y, z) represents the grid location of the field component and the superscript represents the current time iteration. Faraday's law is then rearranged into the FDTD update equation for the H_x component

$$H_x^{t+\frac{\Delta t}{2}}\left(x + \frac{\Delta x}{2}, y + \frac{\Delta y}{2}, z + \frac{\Delta z}{2}\right) = H_x^{t-\frac{\Delta t}{2}}\left(x + \frac{\Delta x}{2}, y + \frac{\Delta y}{2}, z + \frac{\Delta z}{2}\right) + c_0 \Delta t \left[\frac{(E_y^t(x, y, z + 1) - E_y^t(x, y, z))}{\Delta z} - \frac{(E_z^t(x, y + 1, z) - E_z^t(x, y, z))}{\Delta y} \right], \quad (2.7)$$

The ratio of the temporal to the spatial time step is governed by the Courant stability condition $\Delta t \leq \frac{1}{c_0 \sqrt{\frac{1}{\Delta x^2} + \frac{1}{\Delta y^2} + \frac{1}{\Delta z^2}}}$ [69]. Similarly the update equation for the D_x component is

$$D_x^t(x, y, z) = D_x^{t-1}(x, y, z) + c_0 \Delta t \left[\frac{\left(H_z^{t-\frac{\Delta t}{2}}(x, y + \frac{\Delta y}{2}, z) - H_z^{t-\frac{\Delta t}{2}}(x, y - \frac{\Delta y}{2}, z) \right)}{\Delta y} - \frac{\left(H_y^{t-\frac{\Delta t}{2}}(x, y, z + \frac{\Delta z}{2}) - H_y^{t-\frac{\Delta t}{2}}(x, y, z - \frac{\Delta z}{2}) \right)}{\Delta z} \right], \quad (2.8)$$

As is convention, the $\pm \frac{\Delta x}{2}, \pm \frac{\Delta y}{2}, \pm \frac{\Delta z}{2}$ and $\pm \frac{\Delta t}{2}$ steps will be assumed for all magnetic field indexes for the remainder of this dissertation.

For the simulations performed in this dissertation it is assumed that no charge or current sources are present. Thus the Maxwell divergence equations become $\nabla \cdot \mathbf{B} = 0$, and $\nabla \cdot \mathbf{D} = 0$.

While the FDTD algorithm need not explicitly enforce these relations, under the condition that no charge is present, as they are a direct consequence of the Maxwell curl equations, it is vital that the FDTD spatial lattice be structured such that they are *implicitly* satisfied. Section 3.6.9 of reference [70] provides proof of this satisfaction by the Yee grid and algorithm by taking the time derivative of the total electric flux density over the surface of a single Yee cell, as shown in Fig 2.1, and showing that

$$\frac{\partial}{\partial t} \iint_{\text{Yee cell}} \mathbf{D} \cdot d\mathbf{S} = 0, \quad (2.9)$$

for all time steps.

All the data from FDTD simulations in this dissertation were produced using an in-house FDTD code written specifically for this dissertation. To produce a functional tool for the devices studied in this dissertation several factors needed to be included. To simulate materials with discrete translational symmetry, a method for periodic boundaries was included. To prevent errors caused by boundary reflections in the simulation, multiple formulations for absorbing boundaries were trialed. To excite various optical features at different wavelengths, different options for applying and shaping source functions were utilized. To observe different types of data, several sensors were developed that output information in both the time and frequency-domains. To increase simulation speed the code was accelerated using Nvidia GPU hardware. Finally, to analyze the data produced by the code several tools were developed to aid in their visualization and understanding.

2.2 Materials Models

Various material models were adapted for use in the FDTD method for this dissertation. As all materials were non-magnetic the physics of this adaptation was applied via the constitutive relation $\mathbf{D}(\omega) = \epsilon_0 \epsilon_r(\omega) \mathbf{E}(\omega)$. Materials with low variation of $\epsilon(\omega)$ in the frequency

range studied were modeled an an idealized constant value for ε_r . For dispersive materials frequency-domain models were converted into the time-domain using the Z -transform method to derive auxiliary differential equations [71–73]. The models converted included, the Drude, Debye-Drude, and Lorentz models. The parameters used in these models were obtained by fitting the model reflectance spectrum calculated by the transfer matrix method [61] to published data sets using a nonlinear least squares method. The reflectance spectrum is calculated from the TMM using

$$R = \left| \frac{\eta_0 - Y}{\eta_0 + Y} \right|^2, \quad Y = \frac{\eta_2 \cos \delta + i \sin \delta}{\eta_2 \cos \delta + \frac{i \eta_2}{\eta_1} \sin \delta}, \quad (2.10)$$

$$\eta_1 = \eta_0 \sqrt{\varepsilon_{\text{hBN}}(\omega)}, \quad \delta = \frac{\omega d}{c_0} \sqrt{\varepsilon_{\text{hBN}}(\omega)} \cos \theta,$$

where the admittance, η , is the reciprocal optical impedance, η_0 is optical admittance of free-space, η_b is optical admittance of the substrate, c_0 is the speed of light in a vacuum, and $\eta_2 = \eta_0 \eta_b$.

The majority of dispersive materials in this dissertation were simulated using one or a combination of three important generic classes of material model: (1) the Debye relaxation model, (2) the Drude model of metals, and (3) the Lorentz model. These models could be applied isotropically or anisotropically. As these models are defined in the frequency-domain it was necessary to convert them into a form that could be solved in the time-domain. To do this the Z -transform method was used [71–73]. The Z -transform is a method used in signal processing that converts a discrete-time signal, which is a sequence of real or complex numbers, into a complex frequency-domain representation. It can be considered as a discrete-time equivalent of the Laplace transform. In this dissertation it was utilized to derive update equations from frequency domain material models. Further discussion of this method can be found in Appendix A of this dissertation.

2.2.1 Debye Model

Debye media are characterized by a complex-valued, frequency domain susceptibility that has one or more poles at separate frequencies. for a Debye medium having P poles the dielectric function can be expressed as

$$\varepsilon_r(\omega) = \varepsilon_\infty + \sum_{p=1}^P \frac{\Delta\varepsilon_p}{1 - i\omega\tau_p}, \quad (2.11)$$

where ε_∞ is the dielectric function at infinity, $\Delta\varepsilon_p$ is the change in relative permittivity due to the Debye pole, and τ_p is the pole relaxation time. This model was not used on its own and was not Z -transformed for this dissertation.

2.2.2 Drude Model

At optical wavelengths it is important to treat electromagnetic wave interactions with metals using a dispersive formulation to properly account for the physics of internal electron motion. At a macroscopic scale, the Drude model is a widely accepted model for such an application. For a single-pole Drude medium the relative permittivity is expressed as

$$\varepsilon_r(\omega) = \varepsilon_\infty - \frac{\omega_p^2}{\omega^2 + i\nu_c\omega}, \quad (2.12)$$

where ω_p is the plasma frequency, and ν_c is the inverse relaxation time. This model was not used on its own and was not Z -transformed for this dissertation.

2.2.3 Debye-Drude Model

In the metals modeled in this dissertation a better fit to the published dielectric data was obtained by using a combined Debye-Drude model of the form

$$\varepsilon_r(\omega) = \varepsilon_\infty + \frac{\varepsilon_s - \varepsilon_\infty}{1 - i\omega\tau_0} - \frac{\sigma}{i\omega\varepsilon_0}, \quad (2.13)$$

where ε_s is the static dielectric constant, and σ is the conductivity of the metal. When the Z-transform was applied the resulting update equations for each field component were

$$E_{m,n,p}^t = \frac{D_{m,n,p}^t - I_{m,n,p}^{t-1} - e^{-\frac{dt}{\tau_0}} S_{m,n,p}^{t-1}}{C}, \quad (2.14)$$

$$I_{m,n,p}^t = I_{m,n,p}^{t-1} + \frac{\sigma dt}{\varepsilon_0} E_{m,n,p}^t, \quad (2.15)$$

$$S_{m,n,p}^t = e^{-\frac{dt}{\tau_0}} S_{m,n,p}^{t-1} + \frac{(\varepsilon_s - \varepsilon_\infty) dt}{\tau_0} E_{m,n,p}^t, \quad (2.16)$$

$$C = \varepsilon_\infty + \frac{\sigma dt}{\varepsilon_0} + \frac{(\varepsilon_s - \varepsilon_\infty) dt}{\tau_0}, \quad (2.17)$$

where m , n , and p are the $x-$, $y-$, and $z-$ coordinates, respectively, and t is the temporal step.

2.2.4 Lorentz Model

Lorentz media are characterized by a complex valued, frequency-domain susceptibility function that has one or more pairs of complex-conjugate poles. For a Lorentz medium with a single pole pair the relative permittivity is expressed as

$$\varepsilon_r(\omega) = \varepsilon_\infty + \frac{(\varepsilon_s - \varepsilon_\infty)\omega_\nu^2}{\omega_\nu^2 - i\gamma_\nu\omega - \omega^2}, \quad (2.18)$$

where ω_ν is the Lorentz resonant frequency, and γ_ν is the damping constant. When the Z-transform was applied the resulting update equations for each field component were

$$E_{m,n,p}^t = (D_{m,n,p}^t - S_{m,n,p}^{t-1}) / \varepsilon_\infty, \quad (2.19)$$

$$S_{m,n,p}^t = S_{m,n,p}^{t-1} C_1 - S_{m,n,p}^{t-2} C_2 + C_3 E_{m,n,p}^{t-1}, \quad (2.20)$$

$$C_1 = 2e^{-\frac{\gamma_\nu dt}{2}} \cos \left(\omega_\nu dt \sqrt{1 - \left(\frac{\gamma_\nu}{2\omega_\nu} \right)^2} \right), \quad (2.21)$$

$$C_2 = e^{-\gamma_\nu dt}, \quad (2.22)$$

$$C_3 = e^{-\frac{\gamma_\nu dt}{2}} \sin \left(\omega_\nu dt \sqrt{1 - \left(\frac{\gamma_\nu}{2\omega_\nu} \right)^2} \right) \frac{\omega_\nu dt (\varepsilon_s - \varepsilon_\infty)}{\sqrt{1 - \left(\frac{\gamma_\nu}{2\omega_\nu} \right)^2}}. \quad (2.23)$$

2.2.5 Diagonally Anisotropic Materials

In the case of a general anisotropic media the dielectric tensor acts on the constitutive relation as

$$\mathbf{D}(\omega) = \varepsilon_0 \begin{pmatrix} \varepsilon_x(\omega) & 0 & 0 \\ 0 & \varepsilon_y(\omega) & 0 \\ 0 & 0 & \varepsilon_z(\omega) \end{pmatrix} \mathbf{E}(\omega), \quad (2.24)$$

where $\varepsilon_x(\omega)$, $\varepsilon_y(\omega)$ and $\varepsilon_z(\omega)$, are the dielectric functions in the principal directions. Evaluating Eq. 2.24 gives

$$D_x(\omega) = \varepsilon_x(\omega) E_x(\omega), \quad (2.25)$$

$$D_y(\omega) = \varepsilon_y(\omega) E_y(\omega), \quad (2.26)$$

$$D_z(\omega) = \varepsilon_z(\omega) E_z(\omega). \quad (2.27)$$

This reduces to an isotropic model when $\varepsilon_x(\omega) = \varepsilon_y(\omega) = \varepsilon_z(\omega) = \varepsilon_r(\omega)$. This leads to identical update equations for all field components. For anisotropic materials with different $\varepsilon_x(\omega)$, $\varepsilon_y(\omega)$, or $\varepsilon_z(\omega)$, different parameters and/or update equations are required to update individual field components.

2.2.6 Validation of Dispersive Materials Models

Gold (Au) and Silver (Ag) films were modeled by fitting an isotropic Debye-Drude model of the forms detailed in eqn. 2.13 and 2.14, using the method described at the beginning of this section. To simulate Au the model was fit to the wavelength dependent dielectric function data as tabulated in the supplemental materials of the paper by Ciesielski *et al.* [74]. The fit to this data can be seen in Fig. 2.2. The model parameters obtained from this fit were $\varepsilon_\infty = 3.231$, $\varepsilon_s = -1.598 \times 10^4$, $\tau_0 = 1.425 \times 10^{-14}$ s, and $\sigma = 1.006 \times 10^6$ S m⁻¹.

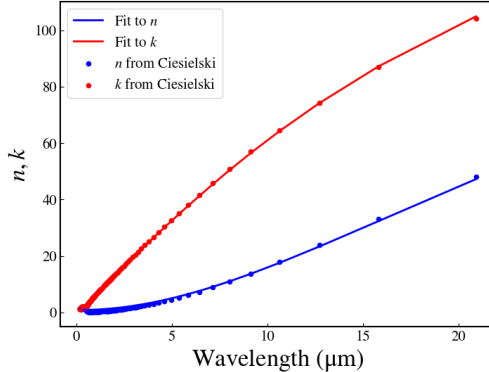


Figure 2.2: Real and imaginary fits of the Debye-Drude model (Eq. 2.13) to the wavelength dependent dielectric function data as tabulated in the supplemental materials of the paper by Ciesielski *et al.* [74]

To simulate hexagonal Boron Nitride (hBN) a tensor Lorentz model was used, *i.e.*,

$$\boldsymbol{\varepsilon}_{\text{hBN}}(\omega) = \begin{pmatrix} \varepsilon_x(\omega) & 0 & 0 \\ 0 & \varepsilon_y(\omega) & 0 \\ 0 & 0 & \varepsilon_z(\omega) \end{pmatrix}, \quad (2.28)$$

where

$$\varepsilon_k(\omega) = \varepsilon_k(\infty) + \frac{S_k \omega_k^2}{\omega_k^2 - i\gamma_k \omega - \omega^2}, \quad (2.29)$$

$\varepsilon_k(\infty)$ is the k^{th} component (where $k = x, y, z$) of the dielectric function at infinity, ω_k is the frequency of a transverse optical phonon propagating in the k^{th} direction, the factor $S_k \omega_k^2$ can be written in the form $\varepsilon_k(\infty)(\omega_{\text{LO}}^2 - \omega_{\text{TO}}^2)$ [25], showing the explicit dependence on the longitudinal optical (LO) and transverse optical (TO) phonon frequencies. In the case of hexagonal Boron Nitride (hBN), the symmetry of the hBN lattice requires that $\varepsilon_x(\omega) = \varepsilon_y(\omega)$. As the polarization of the excitation source used was parallel to the hBN surface, the in-plane parameters used in this research were $\varepsilon_{x,y}(\infty) = 4.87$, $S_{x,y} = 0.61$, $\hbar\omega_{x,y} = 170.1 \text{ meV}$. The out-of-plane parameters were $\varepsilon_z(\infty) = 2.95$, $S_z = 0.61$, $\gamma_z = 0.25 \text{ meV}$, and $\hbar\omega_z = 92.5 \text{ meV}$ from Ref. [75]. The notable exception was the planar damping constant $\gamma_{x,y}$, which has been shown to have a strong thickness dependence by Caldwell *et al* as can be seen in Fig. 2.3.

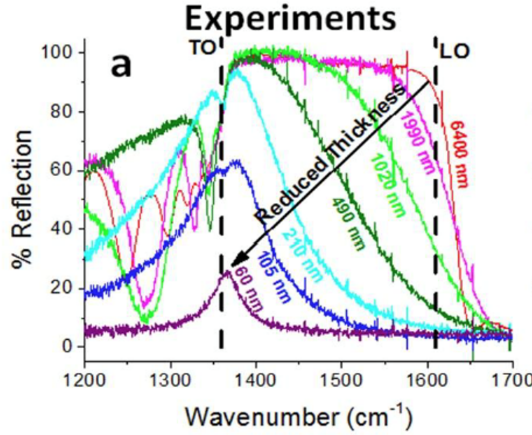


Figure 2.3: Results published by Caldwell *et al.*, [13], showing the reflection spectra for various thicknesses of hBN. As can be seen the Lorentzian lineshape changes dramatically with variance in the thickness of the hBN layer due to a change in $\gamma_{x,y}(d_{\text{hBN}})$,

To calculate $\gamma_{x,y}(d_{\text{hBN}})$ a Lorentzian model was fit to digitized data from Fig. 2.3. From these fits, as shown in Fig. 2.4 (a), the value of $\gamma_{x,y}(d_{\text{hBN}})$ was extracted for each hBN film thickness. These values were fit to a power law relation as shown in Fig. 2.4 (b) in the

form of a log-log plot. From this relation the appropriate value of $\gamma_{x,y}$ for a film thickness of 80 nm was found to be $6.149 \times 10^{12} \text{ rad s}^{-1}$, or 3.97 meV. The value of $\gamma_{x,y}$ obtained was used in a Lorentz model to simulate an infinite sheet of 80 nm thick hBN in a vacuum. The resulting reflection, transmission and absorptance spectra is shown in Fig. 2.4 (c). The dark lines were calculated using the transfer matrix method while the bright lines were calculated using the in-house FDTD code developed for this dissertation. It was determined that the agreement between the two methods was good and this value of $\gamma_{x,y}$ was used for all 80 nm thick hBN layers studied in this dissertation.

2.3 Sources

Two nominal categories of sources are most often applied in the FDTD method, hard sources and soft sources. A source is said to be a hard source when after updating the field across the entire grid, one field component at one point on the grid is overwritten with the source. This approach injects power into the model, but the source point behaves like a perfect electric conductor or perfect magnetic conductor and will scatter waves. Conversely a soft source is when the source value is added to the field component at one point on the grid and is transparent to any scattered waves passing through it. Such a source is implemented by *adding* a source function to the field component(s) at the point(s) where the source is located. Simulations in this work exclusively used soft source formulations.

Simulations in this dissertation used two methods for inputting an electromagnetic source: pointwise sources and Total-Field Scattered-Field sources. For either source a time domain function is used to evolve the field value(s) at a specified location within the simulation space. While a harmonic source could be used this would fail to utilize the broadband frequency functionality of FDTD. For this reason much of the work in this dissertation was done using simulations excited by a Ricker wavelet [76]. For simulations that required either a narrow band or extremely broadband excitation a sinusoidally modulated Gaussian pulse was used.

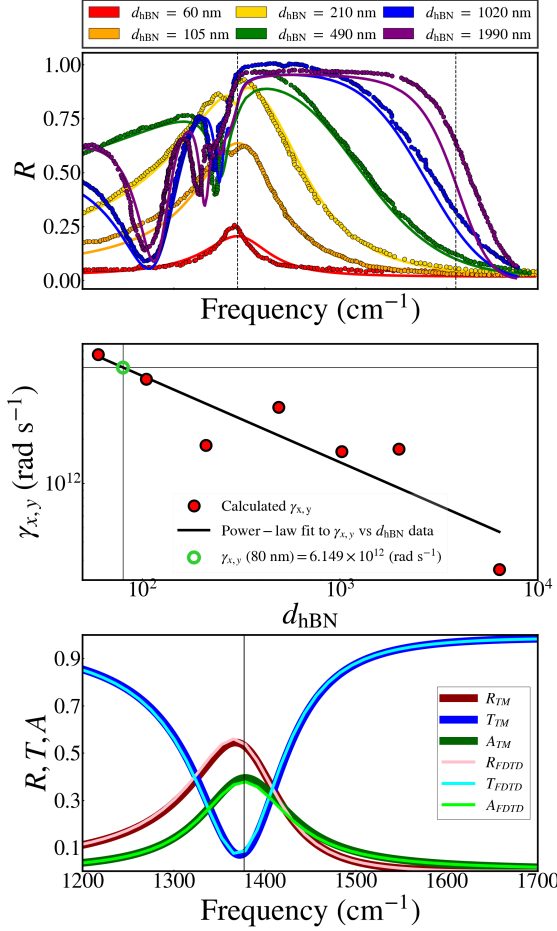


Figure 2.4: (a) Reflectance spectra for various thicknesses of hBN. The dots are digitized data from Caldwell *et al.*, [13], the solid lines are the spectra calculated using the transfer matrix method. (b) A log-log power law fit to the calculated values of $\gamma_{x,y}(d_{\text{hBN}})$, (c) Reflection, transmission and absorptance spectra for an infinite sheet of 80 nm thick hBN in a vacuum. These data were obtained using the Lorentz parameter $\gamma_{x,y}(d_{\text{hBN}})$ calculated in pane (b). The dark lines were calculated using the transfer matrix method while the bright lines were calculated using the in-house FDTD code developed for this dissertation.

2.3.1 Point Sources

A point source in FDTD is simulated by varying a single (or array of single) grid points using a source function. One or more specific grid point(s) are set to update in accordance to a time dependent function, $E_k(t)$ or $H_k(t)$, where k represents x , y or z . These sources are used to simulate dipoles or pseudo point sources, such as an atomic force microscope tip.

2.3.2 Total-Field Scatter-Field Source

A Total-Field Scatter-Field (TFSF) source allows the simulation of unidirectional plane waves. The electric or magnetic fields perpendicular to the direction of propagation are updated along the plane of the “incident” boundary. Polarization of the source is achieved by modifying the update functions *e.g.*, E_y polarization is achieved by setting the source update to zero, $E_x(t) = 0$. To prevent the source propagating backwards the opposite perpendicular field is subtracted from the TFSF boundary when the corresponding field is updated. A major benefit of the TFSF method is it produces two areas of the simulation, the total-field, where the incident source is directed, and the scattered field, where all field strength is due to scattering from objects or devices in the total-field volume. This feature greatly eases the calculation of reflectance spectra, as detailed in section 2.5.2.

2.3.3 Modulated Gaussian Function

As discussed earlier, one of the main benefits of the FDTD method is its ability to study a broadband spectrum. In order to do so it is important to use pulsed source functions for input. This section details the formulation of the two source functions utilized in this dissertation: a modulated Gaussian function and the Ricker wavelet.

When a source required the pulse width and central frequency of the pulse to be specified independently, a sinusoidally modulated Gaussian pulse was used. This can be expressed as

$$f_r(t) = e^{-\left(\frac{t-t_0}{2\sigma}\right)^2} \sin [\omega_0(t - t_0)], \quad (2.30)$$

where t_0 is the temporal delay, σ is a pulse width parameter and ω_0 is the central frequency in rad cm⁻¹.

2.3.4 The Ricker Wavelet

The Ricker wavelet, (2.31), is a pulsed source equivalent to the second derivative of a Gaussian. This source was also used for broad band simulations. Unlike a general modulated Gaussian pulse there is no DC component. The temporal pulse delay was able to be set such that the source “turned” on gradually. This gradual nature combined with a lack of a DC component reduced the occurrence of non-physical numerical artifacts in simulations. The spectral content was centered around a peak frequency in the spectral range of interest for each study. The Ricker wavelet is defined by

$$f_r(t) = \left(1 - 2(\pi\nu_p(t - d_r)^2)\right) e^{-(\pi\nu_p(t - d_r)^2)}, \quad (2.31)$$

where ν_p is related to the pulse width and d_r is the temporal pulse delay.

2.4 Boundary Conditions

In order to simulate various structures different boundary types were incorporated into the code. These boundary types can be categorized into periodic boundaries and absorbing boundaries.

2.4.1 Periodic Boundary Conditions

To efficiently simulate periodic metamaterials, such as a grating, the simulation space consisted of the smallest repeating structure. The simulation would be spatially terminated by periodic boundary conditions in the transverse directions (*i.e.*, the x - and y -direction). This is accomplished by updating the discretized $\nabla \times \mathbf{E}$ and $\nabla \times \mathbf{H}$ equations along the upper and lower boundaries of the simulation explicitly, *i.e.*,

$$(\nabla \times E)_x(x, N_y, z) = \frac{E_z^t(x, N_y, z) - E_z^t(x, 0, z)}{\Delta y} + \frac{E_y^t(x, N_y, z+1) - E_y^t(x, N_y, z)}{\Delta z}, \quad (2.32)$$

where N_y is the size of the simulation space in the y -direction. When the cells at $y = N_y$ are updated the term $E_z^t(x, y+1, z)$ is replaced with $E_z^t(x, 0, z)$. Thus any signal exiting through a cell along the $y = N_y$ boundary reenters the simulation at $y = 0$. To create an infinite two-dimensional simulation space. By repeating this procedure along the x boundary an infinite periodic sheet is simulated. Similarly along the lower boundaries the \mathbf{H} field is updated as:

$$(\nabla \times H)_x(x, 0, z) = \frac{H_z^t(x, 0, z) - H_z^t(x, N_y, z)}{\Delta y} - \frac{H_y^t(x, 0, z) - H_y^t(x, 0, z-1)}{\Delta z}. \quad (2.33)$$

2.4.2 Bloch Periodic Boundary Conditions

In 1928 Felix Bloch proved that in periodic media it is possible for waves to propagate without scattering [77], their behavior governed by a periodic envelope function multiplied by a planewave. While Bloch's research was in the quantum mechanics of electron scattering, the same methods can be utilized in electromagnetism. Bloch's theory can be applied by using the Maxwell curl equations as an eigenproblem analogous to Bloch's treatment of Schrödinger's equation [78]. The Bloch-Floquet theorem for periodic eigenproblems states that solutions to the Maxwell Curl equations can be expressed as a plane wave with an envelope of the form $\mathbf{H}(\mathbf{r}) = e^{i\mathbf{k}\cdot\mathbf{r}} \mathbf{H}_{n,\mathbf{k}}(\mathbf{r})$ with eigenvalues $\omega_n(\mathbf{k})$. Where \mathbf{k} is the reciprocal lattice vector and n is an integer which labels discrete eigenvalues.

The reciprocal lattice vectors, $\mathbf{k} = \frac{2\pi}{a}$ where \mathbf{a} is the lattice vector of the structure, form the reciprocal lattice. The unit cell of this reciprocal lattice is referred to as the Brillouin zone. When all symmetries of the Brillouin zone are considered reference [79] states that only

the smallest region of symmetry need be considered. This region is termed the irreducible Brillouin zone.

To implement a Bloch periodic boundary the periodic boundary condition in the y -direction,

$$E_x^t(x, N_y + 1, z) = E_x^t(x, 0, z), \quad (2.34)$$

is replaced with

$$E_x^t(x, N_y + 1, z) = E_x^t(x, 0, z) e^{ik_y a_y}, \quad (2.35)$$

where a_y is the periodicity in the y -direction. Implementing such a boundary allows for waves of the form $\mathbf{H}(\mathbf{r}) = e^{i\mathbf{k}\cdot\mathbf{r}} \mathbf{H}_{n,\mathbf{k}}(\mathbf{r})$ to propagate without scattering while, over time, other wave forms with destructively interfere until they reach negligible amplitudes. By recording data taken in such a simulation the propagating eigenvalues, $\omega_n(\mathbf{k})$, can be determined. Further discussion on Bloch's theory as applied to electromagnetics can be found in reference [78].

2.4.3 Perfectly Matched Layers

Terminating simulations with an absorbing boundary was required to simulate a lattice extending to infinity. By perfectly matching the impedance of the grid to the impedance at the absorbing boundary the reflections can be reduced. This is improved when several layers of gradually increasing absorbing parameters are used. this is called a perfectly matched layer (PML) method. Though not a boundary condition in the technical sense, PML methods are discussed in this section as they are an important method for terminating an FDTD simulation space.

2.4.4 Uniaxial Perfectly Matched Layer (UPML)

When an object or device in a simulation is hit by a wave it will scatter the applied wave in many potential directions. Waves could propagate at different angles and speeds through the boundary. When loss is introduced at a boundary, reflections will still occur. In order to eliminate reflections to a negligible amplitude for all angles and polarizations an anisotropic material can be used. For the portions of the lattice occupied by the PML an anisotropic dielectric tensor \mathbf{S} is used. For this dissertation only z -direction boundaries needed to be terminated with an absorbing boundary. Thus the tensor was of the form

$$\mathbf{S} = \begin{pmatrix} s_z & 0 & 0 \\ 0 & s_z & 0 \\ 0 & 0 & s_z^{-1} \end{pmatrix}, \quad (2.36)$$

where $s_z = 1 - \frac{\sigma_z}{i\omega\varepsilon_0}$. The update equations for the UPML take the form

$$\nabla \times \mathbf{H}(\omega) = -\frac{i\omega}{c_0} \mathbf{S} \cdot \mathbf{D}(\omega). \quad (2.37)$$

The values for σ are calculated using

$$\sigma_z = \begin{cases} \frac{\varepsilon_0}{2\Delta t} \left(\frac{z}{L_z}\right)^3, & z \leq z_{\min}, z \geq z_{\max} \\ 0, & z_{\min} < z < z_{\max} \end{cases}, \quad (2.38)$$

The final update equations are

$$H_x(x, y, z)^{t+\frac{\Delta t}{2}} = C_1 H_x(x, y, z)^{t+\frac{\Delta t}{2}} + C_2 (\nabla \times \mathbf{E}^t)_x, \quad (2.39)$$

$$H_y(x, y, z)^{t+\frac{\Delta t}{2}} = C_1 H_y(x, y, z)^{t+\frac{\Delta t}{2}} + C_2 (\nabla \times \mathbf{E}^t)_y, \quad (2.40)$$

$$H_z(x, y, z)^{t+\frac{\Delta t}{2}} = H_z(x, y, z)^{t+\frac{\Delta t}{2}} + C_2 (\nabla \times \mathbf{E}^t)_z + C_3 \sum_{T=0}^t (\nabla \times \mathbf{E}^t)_z, \quad (2.41)$$

where C_1, C_2 and C_3 are constants involving σ_z . A similar set of update equations are required for the \mathbf{D} field. More information on the UPML can be found in reference [70].

A UPML offers some benefits to frequency domain models. Models can be formulated and implemented without considering the PML beyond adjusting the permittivity along the edges of the lattice. However, when simulations involving metallic edges are run the UPML is likely to cause the simulation to diverge. For this reason a more robust PML formulation was required.

2.4.5 Convolutional Perfectly Matched Layer (CPML)

The UPML is a widely used implementation of the PML method. However, the use of classically defined tensor coefficients, as defined in Eq. 2.36, can lead to large reflection errors for highly evanescent waves or for late-time, low-frequency interactions [70]. It was found that using a properly scaled complex frequency-shifted tensor these limitations could be overcome. To eliminate the issues caused by metallic edge interactions with the PML a new formulation was incorporated called the convolutional PML [80]. Subsequently a more efficient implementation was published using a recursive-convolution technique. The CPML is the current state-of-the-art method for terminating an FDTD boundary with an absorbing layer [68]. Under this formulation the FDTD approximation of Ampere's Law, within the PML of a simulation with an absorbing boundary in the z -dimension only is:

$$\frac{\partial \mathbf{D}}{\partial t} = \varepsilon_0 \begin{pmatrix} s_k(t) & 0 & 0 \\ 0 & s_k(t) & 0 \\ 0 & 0 & s_k(t)^{-1} \end{pmatrix} \nabla \times \mathbf{H}, \quad (2.42)$$

where k is the dimension terminated by the CPML,

$$s_k(t) = \mathcal{F}^{-1} \left(\frac{1}{\kappa_k + \frac{\sigma_k}{a_k - i\omega\varepsilon_0}} \right), \quad (2.43)$$

where κ is the extinction coefficient, and \mathcal{F}^{-1} is the inverse Fourier transform

$$\kappa_k = \begin{cases} 1 + (\kappa_{x, \max} - 1)(\frac{k}{L_k})^3, & k \leq k_{\min}, k \geq k_{\max} \\ 1, & k_{\min} < k < k_{\max} \end{cases}, \quad (2.44)$$

and a_k is an attenuation constant

$$a_k = \begin{cases} a_{x, \max}(\frac{L_k - k}{L_k})^3, & k \leq k_{\min}, k \geq k_{\max} \\ 0, & k_{\min} < k < k_{\max} \end{cases}. \quad (2.45)$$

Applying Eq. 2.43 to Eq. 2.42 and applying the inverse Fourier transform from Eq. 2.43 results in a convolution. Efficient realization of this operation is done using the reverse-convolution methodology, as detailed in section 7.9.1 of Taflove [70]. Once applied, the CPML update equations, shown here for the D_x field, are of the form:

$$\begin{aligned} D_x^t(x, y, z) &= C_a(x, y, z) D_x^{t-1}(x, y, z) \\ &+ C_b(x, y, z) \left[\frac{H_z^{t-1/2}(x, y, z) - H_z^{t-1/2}(x, y - 1, z)}{\Delta y} \right. \\ &\quad \left. - \frac{H_y^{t-1/2}(x, y, z) - H_y^{t-1/2}(x, y, z - 1)}{\kappa_z(x, y, z) \Delta z} + \Psi_{x,z}^t(x, y, z) \right], \end{aligned} \quad (2.46)$$

where (x, y, z) are the spatial coordinates, the superscript t is the time index, the subscripts x, y, z are the field components,

$$C_a(x, y, z) = \frac{(1 - \frac{\sigma(x, y, z) \Delta t}{2})}{(1 + \frac{\sigma(x, y, z) \Delta t}{2})}, \quad (2.47)$$

$$C_b(x, y, z) = \frac{\Delta t}{(1 + \frac{\sigma(x, y, z) \Delta t}{2})}, \quad (2.48)$$

and

$$\Psi_{x,z}^t(x, y, z) = b_z \Psi_{x,z}^{t-1}(x, y, z) + c_z \frac{\partial}{\partial z} H_y^t(x, y, z). \quad (2.49)$$

The constants b_k and c_k are formulations of the principal CPML constants σ_k , κ_k and a_k . Definitions for b_k and c_k can be found in the appendix of this dissertation. corresponding update equations for the CPML are used for each component of the \mathbf{D} and \mathbf{H} fields. The CPML constants are applied during the \mathbf{D} and \mathbf{H} update equations, while the values for $\Psi_{x,z}$ are calculated with their own update equations and added to the appropriate field components after the grid has been updated.

2.5 Sensors

In order for the in-house FDTD code, written for this dissertation to export data, sensors needed to be placed within the simulation space. Two categories of sensor were implemented to produce two categories of data, namely time and frequency-domain data. Both categories of sensor recorded either electric or magnetic field strength. From these data several analysis tools were implemented.

2.5.1 Time-Domain Sensors

Time domain sensors would record field strength at specified field points. Point sensors would record field strength at the location of interest after the lattice had been updated. These sensors could be set to record every time step or at discrete multiples of time steps. In order to record time evolving fields these sensors could be implemented as two dimensional arrays. These time-domain array sensors would record after the lattice had been updated. Most often recordings would be taken at discrete multiples of time steps to reduce the memory requirement. From this type of sensor a cross section of the time evolving fields could be displayed as an animation.

2.5.2 Frequency-Domain Sensors

Reflectance and transmittance spectra were calculated by means of planar Poynting vector monitors which calculated frequency resolved components of the Poynting vector. The frequency resolved field components were calculated “on the fly” using a discrete Fourier-transform (DFT) in the time domain. The Poynting vector was calculated from the field components using a plane wave expansion as detailed in Ref. [81]. The incident field data required to normalize the results were similarly calculated. The individual components of the spectrally resolved electric field in a given plane (*e.g.*, at the vacuum-hBN interface) could be output for further analysis and visualization. For far field spectra a reflectance sensor was placed above the unidirectional TF/SF source and the transmittance sensor was placed within the substrate opposite the device from the source. For near field data, sensors were placed at the surface of the hBN layer to obtain planar views in the yz -plane to obtain cross-sectional views. During each time step the discrete Fourier transform (DFT) was calculated at every grid point in the sensing plane at each frequency of interest.

$$\mathbf{E}(\omega, x, y) = \Delta t \sum_{m=1}^M e^{-im\omega\Delta t} \mathbf{E}(m\Delta t, x, y, z), \quad (2.50)$$

where M is the total number of time steps and m is the current time step. After the simulation, the power was calculated from the real part of the complex Poynting vector using the plane wave expansion method [81]

$$\wp_{\text{Ref}}(\omega, k_x, k_y) = \frac{1}{2} \text{Re} \left[\eta \frac{k_z}{k} |\mathbf{E}(\omega, k_x, k_y)|^2 \right], \quad (2.51)$$

where \mathbf{k} is the wave vector and η is the admittance of the medium containing the sensor. In $|\mathbf{E}(\omega, k_x, k_y)|^2$, both the Euclidian vector norm and the complex absolute value is taken. The reflectance spectra were obtained by normalizing the reflected power by the uniform incident power, *i.e.*,

$$R(\omega) = \sum_{x,y}^{N_x, N_y} \frac{\wp_{\text{Ref}}(\omega, k_x, k_y)}{\wp_{\text{Inc}}(\omega)}. \quad (2.52)$$

The transmittance spectra are similarly calculated. Absorptance spectra are obtained using $A(\omega) = 1 - [T(\omega) + R(\omega)]$.

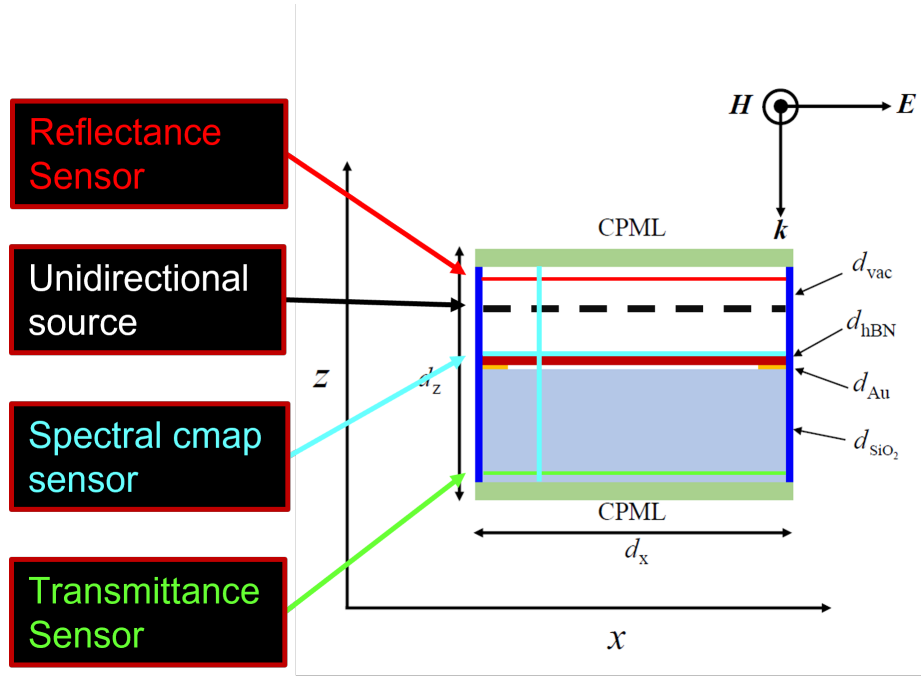


Figure 2.5: Anatomy of a typical simulation used to calculate an absorptance spectrum.

Near field sensors used the same DFT sensor but in post processing the field data for each frequency is plotted as a normalized colormap as shown in Fig. 2.6.

2.6 Parallelization

A historical drawback of the FDTD method is it is computationally time-consuming process using conventional computing methods. A conventional CPU based simulation will step through each cell in the order they are labeled. The processor will only solve one cell component at a time. However, the order the cells are calculated within each time step does not matter. A *parallelized* code will submit a calculation to a processing unit as soon as one

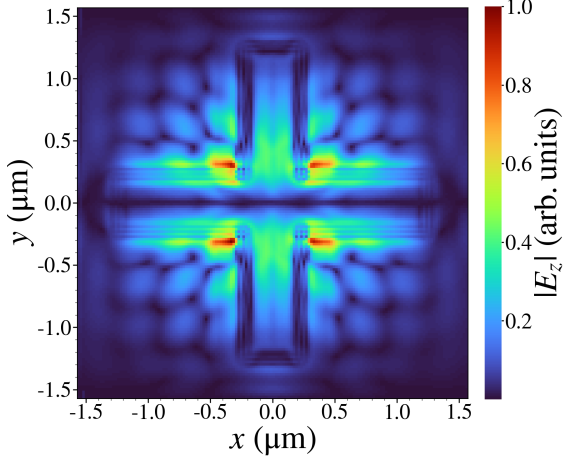


Figure 2.6: Colormap figure produced for near-field analysis.

is available, independent of the state of the other calculations in the loop. These processes are visualized in Fig. 2.7.

In order to decrease run time the decision was made to write an in-house code that parallelized the update equations using graphical processing units (GPUs). While it is possible to use modern CPU technology to provide parallelization, this comes at significant cost. Previous to the development of the in-house code a commercial code was run on a state-of-the-art 48 core Intel Xeon Broadwell processor on the Sapelo high performance computing cluster which required two weeks of wall clock run time. It was decided to write an in-house FDTD code in the C programming language and utilizing the OpenACC GPU framework. Using an Nvidia 3584 core P100 GPU card on the GACRC cluster run speed was significantly increased. The GPU-enabled in-house code ran the same simulation that took two weeks using a commercial code in ~ 12 hours. While other commercial FDTD codes can take advantage of GPUs, they lacked several features needed for this study, such as Lorentzian model materials, CPML boundaries, and DFT sensors.

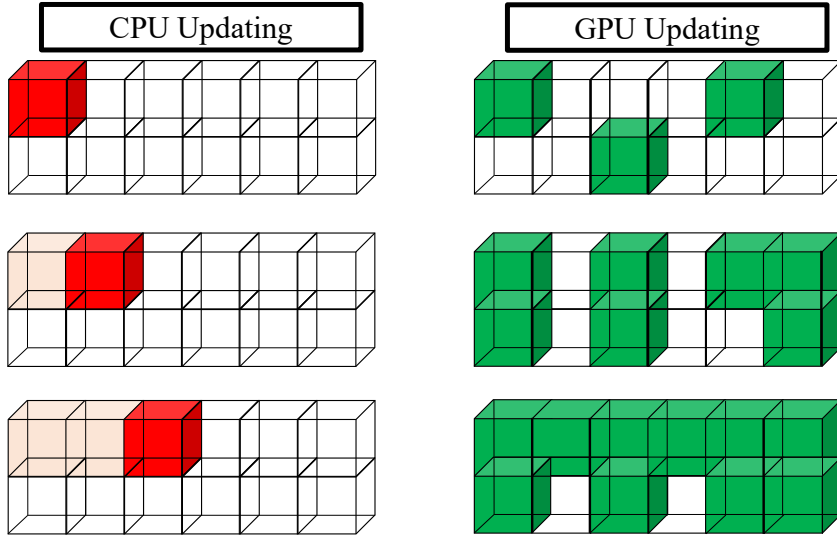


Figure 2.7: Visualization of the CPU and GPU processes for updating the Yee Grid.

2.7 In-House Code Design

In order to update the Yee Grid in an FDTD simulation the processes discussed above needed to be combined. A diagram showing the code flow of the main FDTD loop is shown in Fig. 2.8.

Cardinal parameter values for the simulation would be input into a header file. Using these values the FDTD grid would be initialized. Memory for all of the field arrays would be allocated. Knowing the dielectric values at top and bottom of the z -direction boundary the CPML parameters would be defined. The structure of the device to be simulated would be assigned using manually designed arrays. These arrays would assign the dielectric model associated with grid point. Model parameters would be read from the header file during the

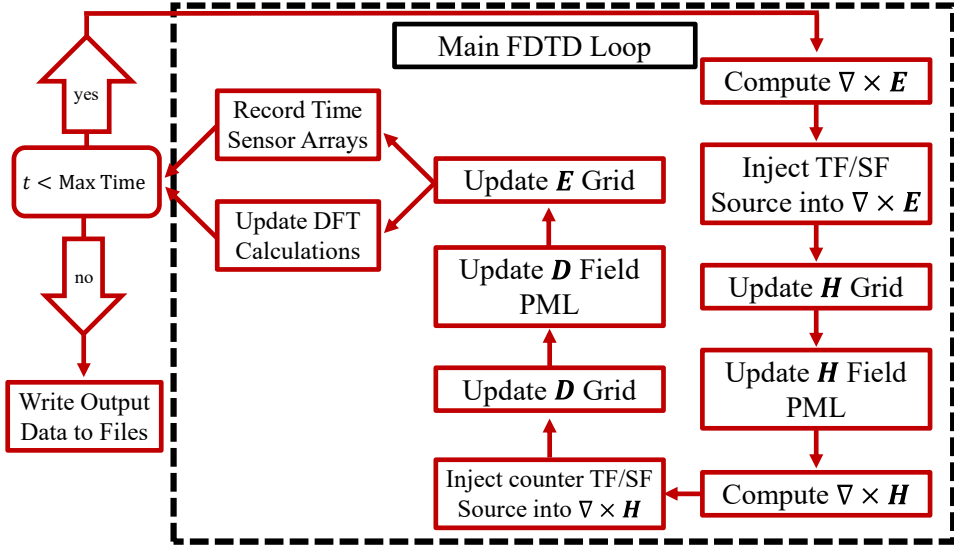


Figure 2.8: A block diagram showing the steps taken during the main FDTD update loop.

update loops. Once the grid was initialized the structure of the grid would be output to a data file that would be used to create cross sectional images of the simulation structure. A diagram showing the initialization of the FDTD grid is shown in Fig. 2.9.

Once the grid was initialized the output files would be initialized in destination directories. Memory for each field array was then allocated on the GPU and the initial field values uploaded to the allocated memory locations. In order to preserve the acceleration facilitated by the GPU, no data arrays would be sent to or from the GPU card during the main FDTD update loop. Once the update loop reached the predetermined maximum time-step the update loop would terminate, and the output data would be withdrawn from the GPU to be written to the output files. A diagram showing the key steps performed by the main program is shown in Fig. 2.10.

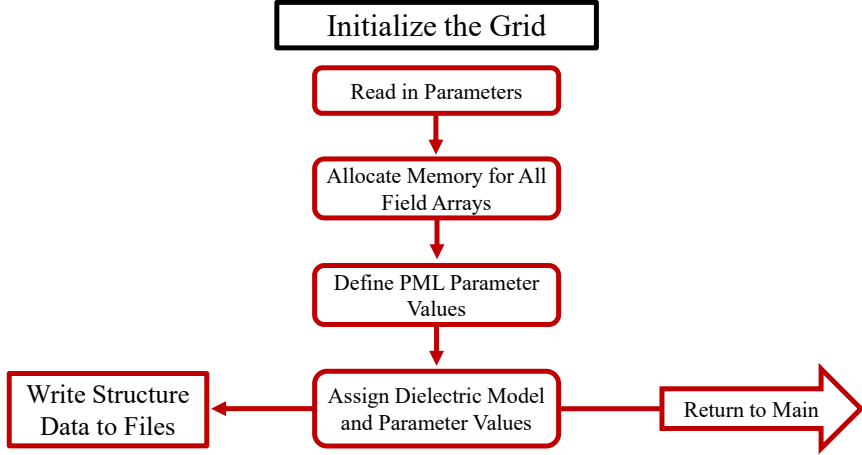


Figure 2.9: Key steps taken to initialize the FDTD grid before the main FDTD update loop.

2.8 Analysis Tools

In addition to the analysis tools detailed above, several additional tools were developed to aid in the analysis of the data produced for this dissertation. Many of the tools were built using Python to analyze data output by either the time-domain or frequency-domain sensors.

2.8.1 Simulation Geometry Imaging

In order to ensure the correct structure was being used in simulations a feature was added to the in-house code which would output the grid structure to a data file at orthogonal cross sections. This file was then used to create a figure using Python. See Fig. 2.11 for an example.

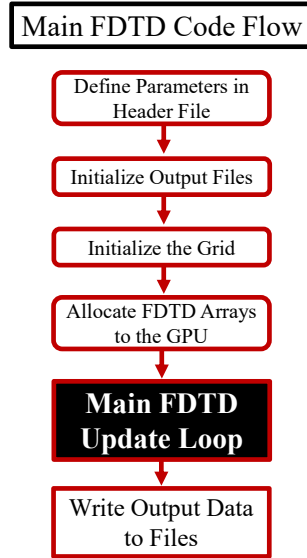


Figure 2.10: Key steps performed by the main in-house code.

2.8.2 Proxy Dispersion Curve Analysis

During this dissertation shifts in the spectra, of the kind detailed in Section 2.5.2, would be observed as device parameters were varied during simulation sweeps. In order to better analyze these spectral peak frequency shifts, the data would be plotted in colormap form as a function of the parameter being varied, as shown in Fig. 3.10. This kind of image was able to act as a limited proxy dispersion curve. To locate peak features indicated by markers in Fig. 3.10 a naive nearest neighbor peak finding algorithm was used as detailed in Section 3.3.

2.8.3 Dispersion Curves

For potential comparison to experiment, it was useful to analyze lineouts from near-field data. A series of lineouts would be taken for each frequency calculated by the DFT sensor

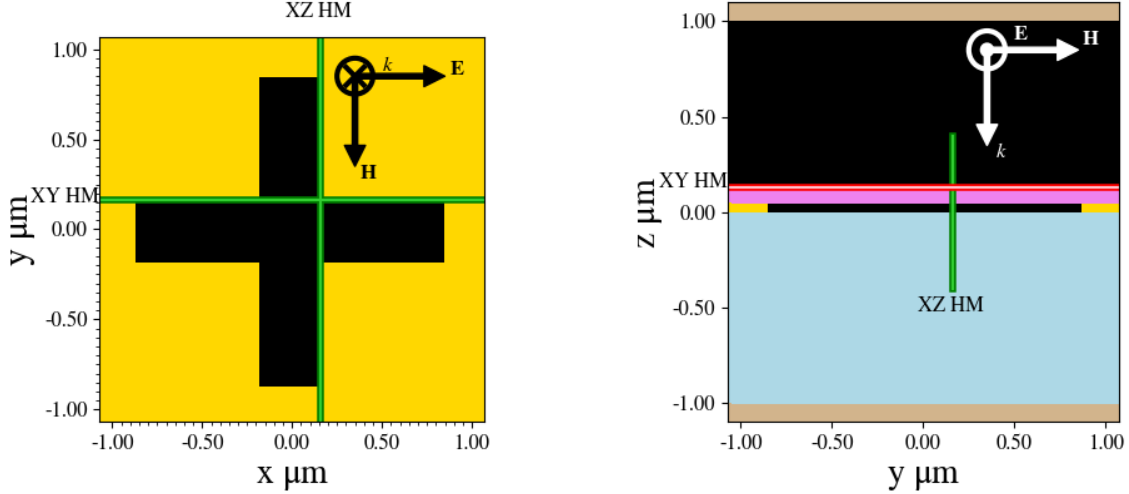


Figure 2.11: (a) Planar view of a Au cross shaped aperture along the xy -plane. Field polarization is indicated by the black arrows. (b) Cross sectional view of the same structure displayed in pane along the yz -plane (a). Field polarization is indicated by the white arrows. Materials are differentiated by color. In this figure the tan represents PML, magenta represents hBN, gold represents Au, light blue represents SiO_2 , and black represents vacuum. Green and red lines indicate the positions of cross sectional and planar frequency domain colormaps respectively, of the kind displayed in Fig. 2.6.

during the main FDTD update loop. An example can be seen in Fig. 2.12. In Fig. 2.12 each row of data corresponds to a separate frequency detection at 1 cm^{-1} resolution. Each column represents a position along the indicated lineout at 2 nm resolution. In Fig. 2.12 (b) the spatial Fourier transform of the data in Fig. 2.12 (a) is shown. This figure enables the visualization of dispersion curves for interesting photonic features.

To demonstrate the analogy to methods used in experimental analysis Fig. 2.13 [82] shows the imaginary component of the AFM measurements of an hBN ribbon over SiO_2 and the spatial Fourier transform of that data. While these figures are from studies of dissimilar devices the similarity in form can be recognized.

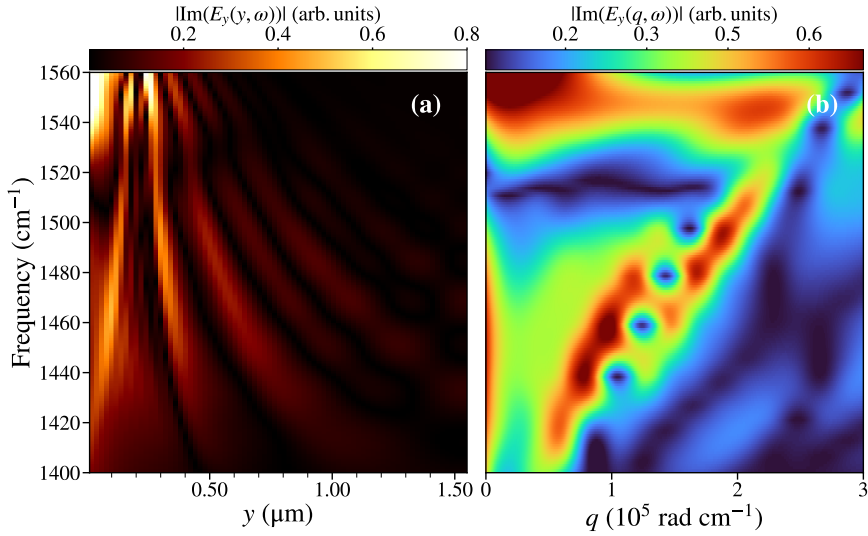


Figure 2.12: (a) Imaginary E_y field lineout data from the device studied in Chapter 3. (b) The spatial Fourier transform of the data from pane (a)

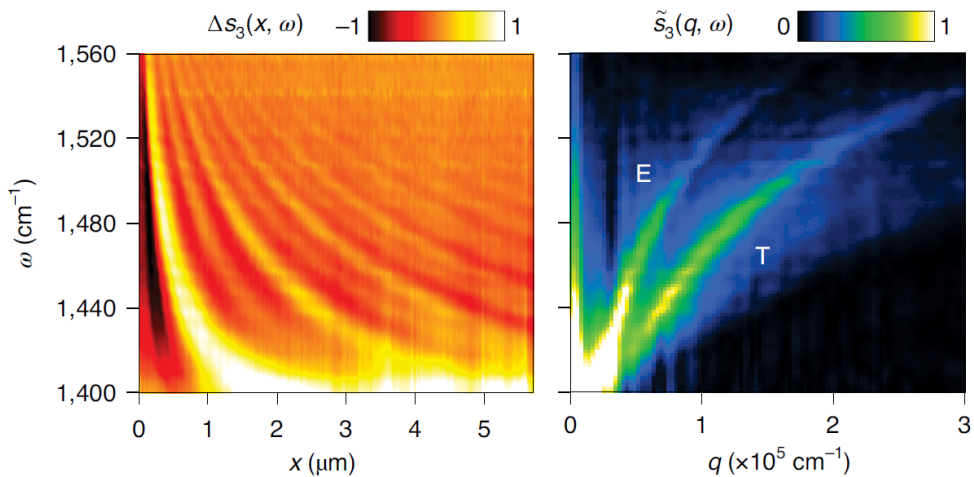


Figure 2.13: Figure from Bylinkin *et.al.*, [82]. The imaginary component of the AFM measurements of an hBN ribbon over SiO_2 and the spatial Fourier transform of that data.

Chapter 3

Coupling of phonon-polaritons with plasmon-polaritons in a layered device comprising hBN on a nanopatterned square array of cross apertures in a Au layer

3.1 Introduction

The device studied in this chapter is an infinite hBN sheet over a square array of cross shaped apertures in Au. The cross shape offers the advantage of four geometric parameters that may be varied to tune the grating's plasmonic resonance to the TO resonance of hBN. These parameters are the Au film thickness, d_{Au} , cross length, l , cross width, w , and periodicity d_{CC} , which must be congruent in the x - and y - directions to maintain a square array structure. Cross-shaped apertures in Au have been shown to exhibit perfect infrared absorption [60] as well as promoting strong plasmon-phonon coupling in an IR resonant material between

the grating and the source [50]. SiO_2 was chosen as a substrate as it can be approximated as optically inert at IR frequencies.

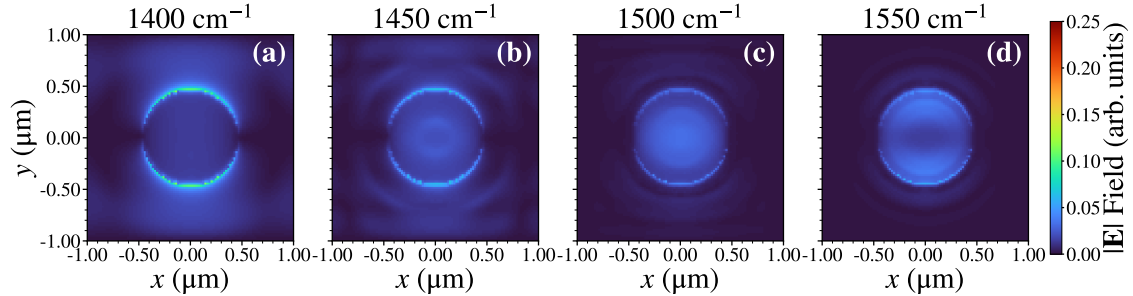


Figure 3.1: Frequency domain color map of hBN film atop of nanopatterned (a square array of holes) etched into a gold (Au) film which was deposited on a fused silica (SiO_2) substrate. The color scale in this figure is normalized to 0.25 the maximum $|\mathbf{E}|$ value obtained from Fig. 3.2 (d), this was done in order to enhance the contrast.

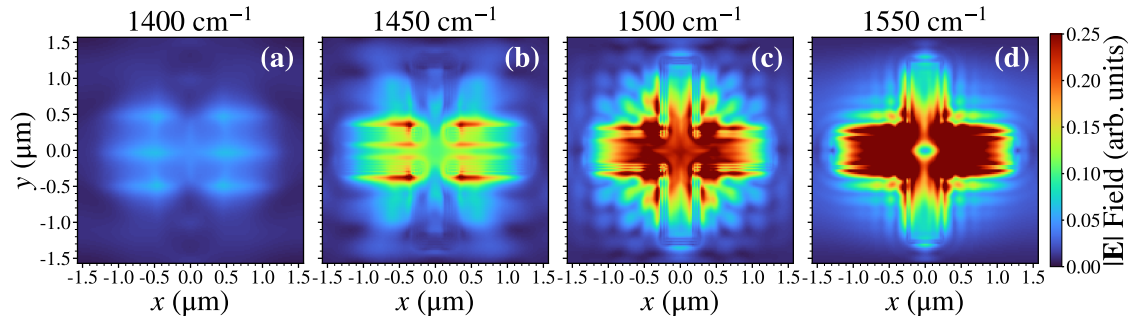


Figure 3.2: Frequency domain color map of hBN film atop of nanopatterned (a square array of crosses) etched into a gold (Au) film which was deposited on a fused silica (SiO_2) substrate. The color scale in this figure is normalized to 0.25 the maximum $|\mathbf{E}|$ value obtained from pane (d), this was done in order to enhance the contrast in Fig 3.2.

As can be seen when comparing Fig. 3.1 with Fig. 3.2 the cross aperture produces significantly more contrast than the circular aperture. Furthermore, for the case of the cross aperture two distinct field patterns can be clearly discerned in the x - and y - directions.

This is likely an indication of coupling between modes with different polarizations and wave vectors and may have implications for device applications.

3.2 Preliminary Measurements

The system modelled in this chapter was an hBN film atop of nanopatterned (a square array of crosses) etched into a gold (Au) film which was deposited on a fused silica (SiO_2) substrate. The combination of the nanopatterned crosses in an Au film was selected as the plasmonic metamaterial layer because the absorption features associated with this device exhibited simpler lineshapes than those calculated for similar devices, *e.g.*, circular holes in either an Ag or Au metal film.

Data in this chapter were produced by computer simulations using the FDTD method as detailed in Chapter 2. Due to the large time constants of the hBN and Au films incorporated in the devices studied in this investigation, $\geq 2 \times 10^6$ time steps were needed for each simulation. This necessitated incorporating GPU acceleration into the in-house code to reduce the runtime required. A combination of OpenACC and CUDA [83] methodologies were used to speed up simulations by a factor of ~ 70 ; this enabled a greater number of higher resolution simulations to be performed in a reasonable time frame.

The details of the principle nanopatterned structure simulated in this chapter are shown in Fig. 3.3. The structure was composed of an 80 nm sheet of hexagonal boron nitride (hBN) deposited on a 50 nm thick film of nanopatterned Au atop of a SiO_2 substrate. The Au film was patterned with cross-shaped apertures. The aperture dimensions were $l = 0.8 d_{\text{CC}}$ and $w = 0.15 d_{\text{CC}}$, where d_{CC} was the model periodicity in the congruent x - and y - dimensions, which was varied during this work.

For the simulations presented in the far-field analysis section of this chapter, a broadband, plane wave source was used. The time profile of the broadband source was a Ricker wavelet [76] centered on $\lambda = 2.4 \mu\text{m}$ (4167 cm^{-1}). For the simulations presented in Figs. 3.13

and 3.14, a very broadband (Gaussian modulated sinusoid) source with a pulse-width (standard deviation), $\tau = 5.0$ fs, and a center wavelength of $\lambda = 7.3 \mu\text{m}$ (1370 cm^{-1}) was used. This source is very flat spectrally and varied in field strength by less than 1.5% across the reststrahlen band. Both sources were laterally uniform in time and injected using the total-field scattered-field (TFSF) interface [84]. Both of these sources were y -polarized and propagated in the negative z -direction. The use of the TFSF method enabled sensors to be placed above the TFSF boundary in order to record only the reflected field values.

To prevent divergence in the simulation caused by edge reflections in the patterned Au layer, a convolutional perfectly matched layer (CPML) [85] boundary was used as the CPML has been shown to be more stable than a uniaxial perfectly matching layer (UPML) [86] absorbing boundary for simulations of this kind. Periodic boundary conditions were used in the transverse directions. In the positive and negative z -directions, the simulation was terminated by 50 perfectly matched layers. Due to the difference between the length scales of features in the transverse and longitudinal directions, the computational grid used cell sizes in the ratio of 10:10:1 in the x -, y - and z -dimensions, respectively. The resonance frequency of the patterned Au layer was found to be only slightly sensitive to the spatial resolution used in the simulation. Convergence testing was performed and a working resolution of $\Delta x = 20 \text{ nm}$, $\Delta y = 20 \text{ nm}$, $\Delta z = 2 \text{ nm}$ was selected to be a good compromise between simulation accuracy and GPU memory limits.

As discussed in detail in Section 2.2 the various components of the device were modelled as follows. The hBN layer was simulated using a tensor Lorentz model. The Au film was simulated using wavelength dependent refractive index data as detailed by Ciesielski *et al.* [74] to fit to a Debye-Drude model. Finally, the SiO_2 substrate was simulated using a simple dielectric with $\epsilon_{\text{SiO}_2} = 2.127$. In order to validate the models of the dispersive materials used in this work, thin films of Au and hBN in vacuo were simulated and the normal incidence absorptance, $A(\omega)$, spectrum for each of the films was calculated using $A(\omega) = 1 - [T(\omega) + R(\omega)]$, where $T(\omega)$ and $R(\omega)$ are the transmittance and reflectance spectra, respectively.

These absorptance spectra were compared with the absorptance spectra calculated for the corresponding film using the transfer matrix (TM) method [61] and excellent agreement between the two methods was observed.

In addition to the structure, denoted the “coupled device” (CD), depicted in Fig. 3.3, several other auxiliary structures were simulated. The “bare device” (BD), this device is identical to the coupled device, but with the hBN layer removed. This device does not support phonon-polaritons. The “uncoupled device I” (UDCI), this device is identical to the coupled device, but with the hBN layer replaced with an equal thickness anisotropic layer that has $\varepsilon_k(\infty)$ equal to the values for hBN, but the resonant behavior removed by setting $S_k = 0$. This device does not support phonon-polaritons. The “uncoupled device II” (UCDII), this device is identical to the coupled device, but with the nanopatterned Au layer replaced with an equal thickness layer of nanopatterned Si modelled by a frequency independent dielectric constant, $\varepsilon_{\text{Si}} = 11.7$; this device does not support plasmons.

The simulational meta-parameters and the materials parameters used to simulate the devices described in this chapter are given in Table 3.1.

In order to investigate the effect of tuning the plasmon resonance through the hBN reststrahlen band, a series of FDTD simulations were performed at a range of distances between the nearest neighbor centers of the crosses, (*i.e.*, d_{CC} in the range 2.34 – 3.94 μm). The resulting $R(\omega)$, $T(\omega)$, and $A(\omega)$ spectra are shown in Fig. 3.4. Two clear features can be observed in each spectra, in Fig. 3.4 (c) these can be described as a smooth peak towards the red and “shark fin” shaped peaks towards the blue end of the spectrum. The smooth peak is the plasmon resonance while the “shark fin” peaks are due to Rayleigh anomalies. A clear red shift in all spectra was observed as the value of d_{CC} was increased. This demonstrated the tunability of the BD plasmon resonance. The shifted resonance of all three spectra appear to be equal in all cases.

A similar series of simulations were performed for the UCDI and are shown in Fig. 3.5. As in the BD a red shift in all spectra was observed as the value of d_{CC} was increased.

Table 3.1: Simulational Parameters

Symbol	Value	Units	Description
Simulational Meta-Parameters			
Δx	20	nm	Spatial step in x -direction
Δy	20	nm	Spatial step in y -direction
Δz	2	nm	Spatial step in z -direction
Δt	5.945×10^{-18}	s	Time step
n_x	$d_{CC}/\Delta x$	N.A.	Number of steps in x -direction
n_y	$d_{CC}/\Delta y$	N.A.	Number of steps in y -direction
n_t	(10^6 , 500×10^3)	N.A.	Number of time steps (near-field, far-field)
n_{PML}	50	N.A.	Number of PML layers in $\pm z$ -direction
Materials Parameters – Au			
ε_∞	3.321	N.A.	High-frequency ε
ε_s	-1.598×10^{-4}	N.A.	Low-frequency ε
τ_0	1.425×10^{-14}	s	Relaxation time
σ	1.006×10^6	Sm^{-1}	Conductivity
Materials Parameters – hBN			
$\varepsilon_{x,y}(\infty)$	4.87	N.A.	High-frequency ε in the x, y -directions
$\varepsilon_z(\infty)$	2.96	N.A.	High-frequency ε in the z -direction
$S_{x,y}$	1.83	N.A.	Dimensionless coupling factor in the x, y -directions
S_z	0.61	N.A.	Dimensionless coupling factor in the z -direction
$\hbar\omega_{x,y}$	170.1	meV	TO phonon frequency in the x, y -directions
$\hbar\omega_z$	92.5	meV	TO phonon frequency in the z -direction
$\gamma_{x,y}$	3.97	meV	Damping constant in the x, y -directions
γ_z	0.25	meV	Damping constant in the z -direction
Materials Parameters – Substrate, Spacer-layers etc.			
$\varepsilon_{\text{SiO}_2}$	2.13	N.A.	Relative permitivity of SiO_2
ε_{Si}	11.73	N.A.	Relative permitivity of Si

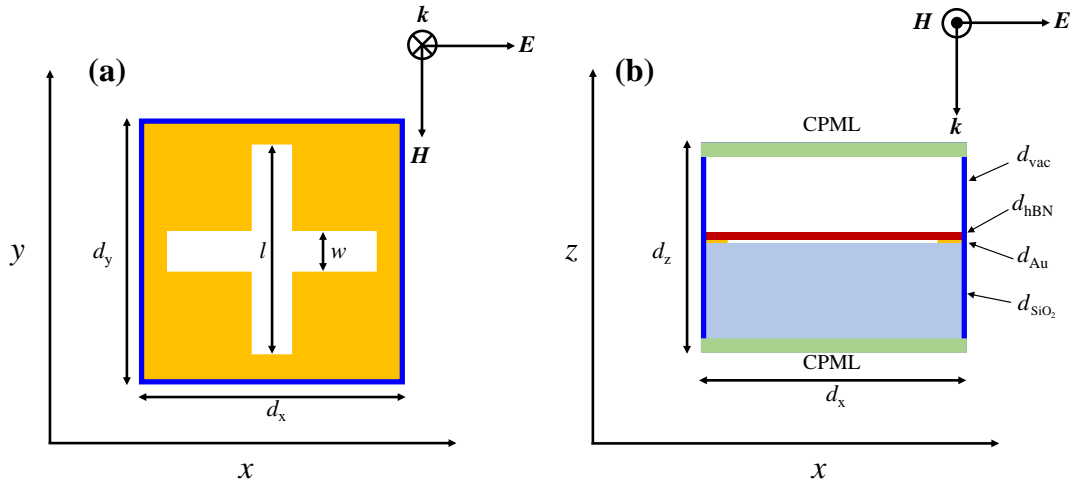


Figure 3.3: Schematic of the hBN/Au structure simulated in this chapter. (a) Planar view at the hBN/Au interface. (b) Cross-sectional view. CPML: Convolutional perfectly matched layer boundary conditions are imposed at the z - direction boundaries. Periodic boundary conditions are imposed at the x and y boundaries. The unit cell lengths in the x - and y -directions are d_x and d_y , respectively. The layer thicknesses are $d_{\text{vac}} = 0.87 \mu\text{m}$, $d_{\text{hBN}} = 80 \text{ nm}$, $d_{\text{SiO}_2} = 1.0 \mu\text{m}$, $d_{\text{Au}} = 50 \text{ nm}$. The length of the long segments of the cross pattern is $l = 0.8 d_x = 0.8 d_y$ while the width of the cross is $w = 0.15 d_x = 0.15 d_y$. The distance between the centers of neighboring crosses is $d_{\text{CC}} = d_x = d_y$. The directions of the \mathbf{E} -field, \mathbf{H} -Field and propagation vector \mathbf{k} are shown in both panes.

As can be seen by comparing the absorptance spectra in Fig. 3.4 (c) and Fig. 3.5 (c) the plasmonic resonance for each UCDI were red shifted when compared to the equivalent d_{CC} BD. However the peak frequencies of the Rayleigh anomalies remained unchanged under the same comparison. The absorptance at the plasmon resonance is increased for the UCDI while the Rayleigh anomaly magnitudes are reduced. The structure with $d_{\text{CC}} = 3.14 \mu\text{m}$ exhibits a plasmon absorptance peak that is most closely resonant with the hBN TO phonon and this device is the one studied most extensively in the near field analysis section of this chapter.

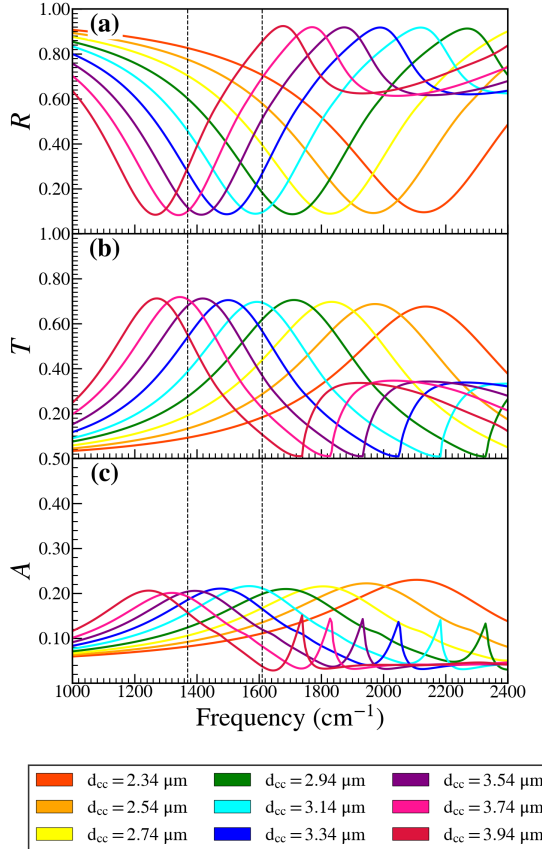


Figure 3.4: The spectra for the BD at a range of d_{CC} values. (a) Reflectance spectra. (b) Transmittance spectra. (c) Absorptance spectra. The vertical black dashed lines in this figure indicate the position of the hBN TO and LO phonon frequencies, at $\omega_{TO} = 1370 \text{ cm}^{-1}$ and $\omega_{LO} = 1610 \text{ cm}^{-1}$, respectively.

The equivalent CD data to those shown above can be seen in Fig. 3.6. The most prominent effect observed in the CD is that the plasmon resonances split into two main peaks to either side of the hBN TO phonon frequency when compared to equivalent d_{CC} UCDI. The peaks for $d_{CC} = 3.14 \mu\text{m}$ device shifted approximately equal amounts above and below the hBN TO phonon frequency. As with the UCDI the resonances of the Rayleigh anomalies remained unchanged.

Another notable feature that is observed in most of the absorptance spectra depicted in Fig. 3.6 (c), is a small peak centered close to the hBN TO phonon frequency, which is also

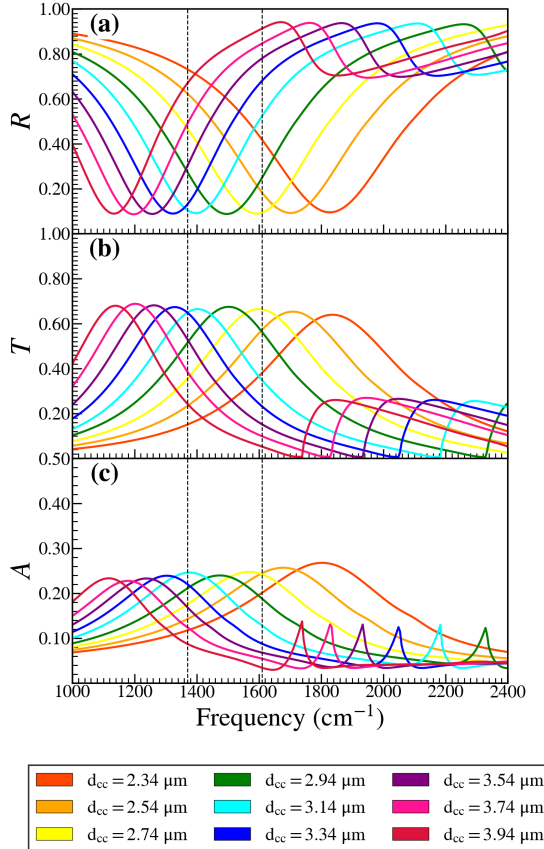


Figure 3.5: The spectra for the UCDI at a range of d_{CC} values. (a) Reflectance spectra. (b) Transmittance spectra. (c) Absorptance spectra. The vertical black dashed lines in this figure indicate the position of the hBN TO and LO phonon frequencies, at $\omega_{TO} = 1370 \text{ cm}^{-1}$ and $\omega_{LO} = 1610 \text{ cm}^{-1}$, respectively.

close to the center of the absorptance peak of the non-plasmonic UCDII. Less obvious in these spectra, but also present are a series of small peaks and shoulders that lie between the hBN TO and LO frequencies, the nature of these latter features will be elucidated below.

3.3 Peak Finding

To determine resonance values for various features it was necessary to perform peak finding. For plasmonic and Rayleigh resonances a naive nearest-neighbor peak finding algorithm was

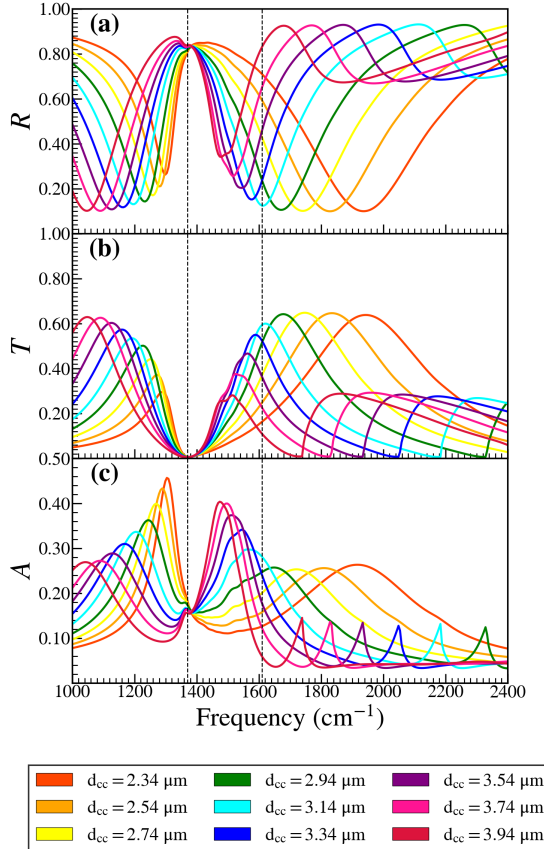


Figure 3.6: The spectra for the CD at a range of d_{CC} values. (a) Reflectance spectra. (b) Transmittance spectra. (c) Absorptance spectra. The vertical black dashed lines in this figure indicate the position of the hBN TO and LO phonon frequencies, at $\omega_{TO} = 1370 \text{ cm}^{-1}$ and $\omega_{LO} = 1610 \text{ cm}^{-1}$, respectively.

used for the resonances displayed in 3.4. To reduce use of computing resources, a power law function was fit to BD plasmonic resonances displayed in 3.4. As can be seen the fit constants for the power law function, ax^b , were calculated to be, 5005.79 and 1.01 for a and b respectively, which closely approximates a linear relationship between the plasmon resonance and $\frac{2\pi}{d_{CC}}$. From this relation the remaining resonances were calculated. The data for this is shown in 3.7.

For the inflection points, seen within the reststrahlen band, the absorptance curve was twice differentiated with respect to frequency. The resulting curve was then multiplied by

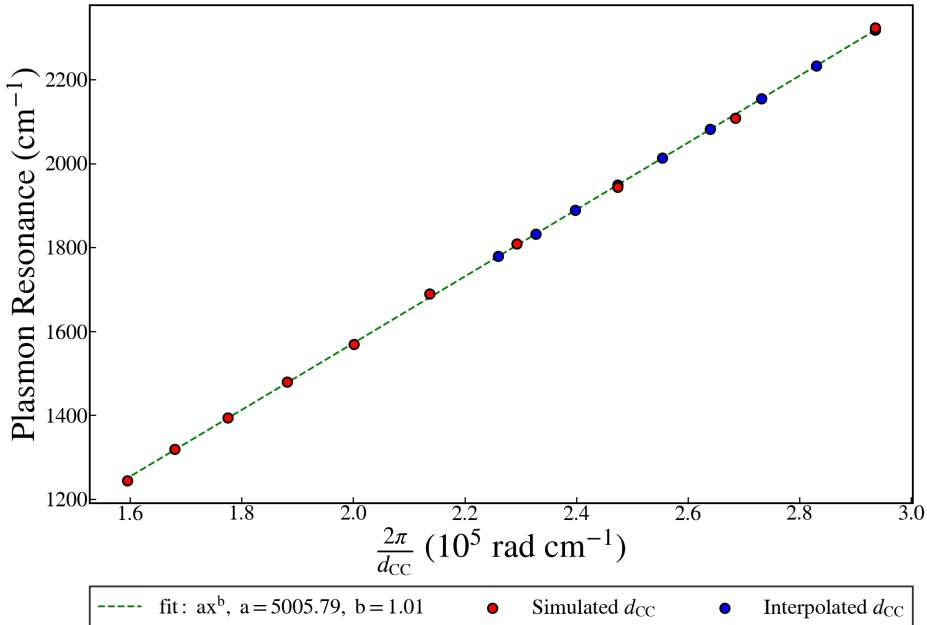


Figure 3.7: The dependence of the plasmon resonance frequency on d_{CC} for the bare device (BD). A power law was fit to the data for the purpose of interpolation. The resulting fit was extremely close to linear.

-1 and the same naive nearest-neighbor peak finding algorithm employed. To eliminate potentially spurious points a minimum $\frac{\partial^2 A(\omega)}{\partial \omega^2}$ value was used. Peaks below this value were discarded. This value was determined for each mode individually. The resulting values can be seen in 3.8 for the $d_{CC} = 3.15 \mu\text{m}$ CD.

3.4 Far-Field Analysis

In order to investigate the effect of tuning the plasmon resonance through the hBN rest-strahlen band, a series of FDTD simulations were performed at a range of distances between the nearest neighbor centers of the crosses, (*i.e.*, d_{CC} in the range $2.34 - 3.94 \mu\text{m}$) and the absorptance spectra for the bare device (BD), the uncoupled device I (UCDI) and the coupled device (CD) structures were calculated from the frequency resolved Poynting vector

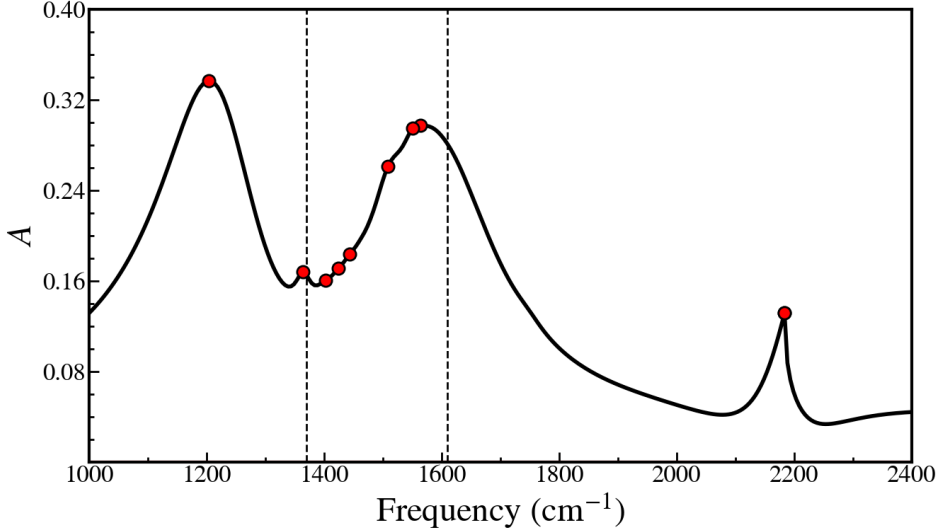


Figure 3.8: Mode locations for the $d_{CC} = 3.15 \mu\text{m}$ CD.

data collected by the planar DFT sensors described in Section 2.5.2. Fig. 3.9 shows the absorption spectra calculated for all three devices. The vertical dashed lines in Fig. 3.9 indicate the positions of the hBN TO and LO phonons at 1370 and 1610 cm^{-1} , respectively. The absorption spectrum of an 80 nm thick free-standing hBN film, as seen in Fig. 2.4 (c), is resonant with the TO phonon frequency. As can be seen from Fig. 3.9 (b), the UCDI structure with $d_{CC} = 3.14 \mu\text{m}$ exhibits a plasmon absorptance peak that is most closely resonant with the hBN TO phonon and this device is the one studied most extensively in this chapter.

Fig. 3.9 (c) shows the absorption spectra for a series of CDs for a range of d_{CC} . Also shown in Fig. 3.9 (c) is the absorptance spectrum of the UCDII with $d_{CC} = 3.14 \mu\text{m}$ (gray dotted line), which exhibits a single peak centered close to the hBN TO frequency. The most prominent effect observed in the CD is that the plasmon absorption spectra in UCDI split into two main peaks either side of the hBN TO phonon frequency, with the peaks for $d_{CC} = 3.14 \mu\text{m}$ device being shifted approximately equal amounts above and below the hBN TO phonon frequency.

Another notable feature that is observed in most of the absorptance spectra depicted in Fig. 3.9 (c), is a small peak centered close to the hBN TO phonon frequency, which is also close to the center of the absorptance peak of the non-plasmonic UCDII. Less obvious in these spectra, but also present are a series of small peaks and shoulders that lie between the hBN TO and LO frequencies, the nature of these latter features will be elucidated below.

Finally, there are a series of cusps that occur in the spectra of all three devices, only one of which is shown in Fig. 3.9. This feature occurs at a frequency of $\sim 1750 \text{ cm}^{-1}$ for all three $d_{\text{CC}} = 3.94 \mu\text{m}$ devices. The assignment of these latter features will be deferred until later in this chapter.

In order to better analyze the absorptance peak frequency shifts observed in Fig. 3.9, the data in Fig. 3.9 (b) and (c) were plotted in colormap form as a function of $\frac{2\pi}{d_{\text{CC}}}$ as prescribed in Wan *et al.* [50] in Fig. 3.10 (a) and 3.10 (b) respectively. These plots can act as a proxy for the dispersion curves, although with some limitations. In both Fig. 3.10 (a) and (b), the peaks in the spectra indicated by the orange, green and blue triangles are due to Rayleigh anomalies [87–89] with indices (0,1), (1,1), (0,2), and their symmetric counterparts, respectively. The red squares in Fig. 3.10 (a) indicate the main absorptance peak due to the plasmon-polariton in the UCDI. These peaks track linearly with $\frac{2\pi}{d_{\text{CC}}}$, the peak of the absorptance of corresponding BD and is analogous to the reflection data presented by Wan *et al.* [50] in their Fig. 3(a). The red squares in Fig. 3.10 (b) show how the absorptance peak due to the plasmon-polariton in UCDI splits due to the interaction the bulk phonon-polariton in the hBN. The circles in Fig. 3.10 (b) are interpreted as indicating slab phonon-polariton modes in the hBN layer; this interpretation will be further supported by the near-field data below.

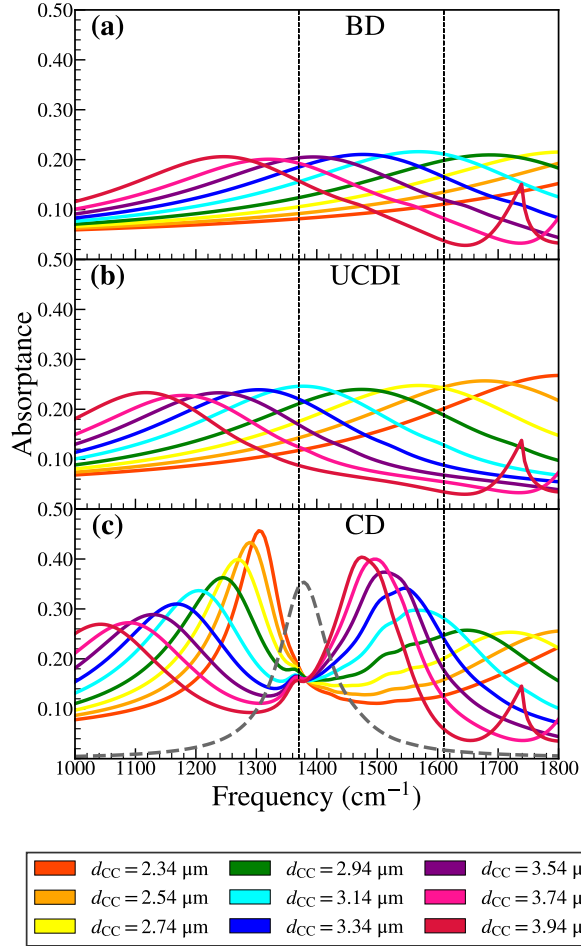


Figure 3.9: (a) The absorptance spectrum of the BD for a range of d_{CC} values. (b) The absorptance spectra of the UCDI. (c) The absorptance spectra of the CD. The gray dotted curve in pane (c) depicts the absorption spectra for the UCDII with $d_{\text{CC}} = 3.14 \mu\text{m}$. The vertical black dashed lines in this figure indicate the position of the hBN TO and LO phonon frequencies as described in the main text.

3.5 Near-Field Analysis

In order to gain insight into the coupling between the plasmon-polaritons in the nanopatterned Au and the phonon-polaritons in hBN film, the electric field distributions, $|\mathbf{E}|$, at the position of the vacuum-hBN interface were investigated for all four devices, *i.e.*, BD, UCDI, UCDII, and CD, as shown in Fig. 3.11. This position was selected as these field

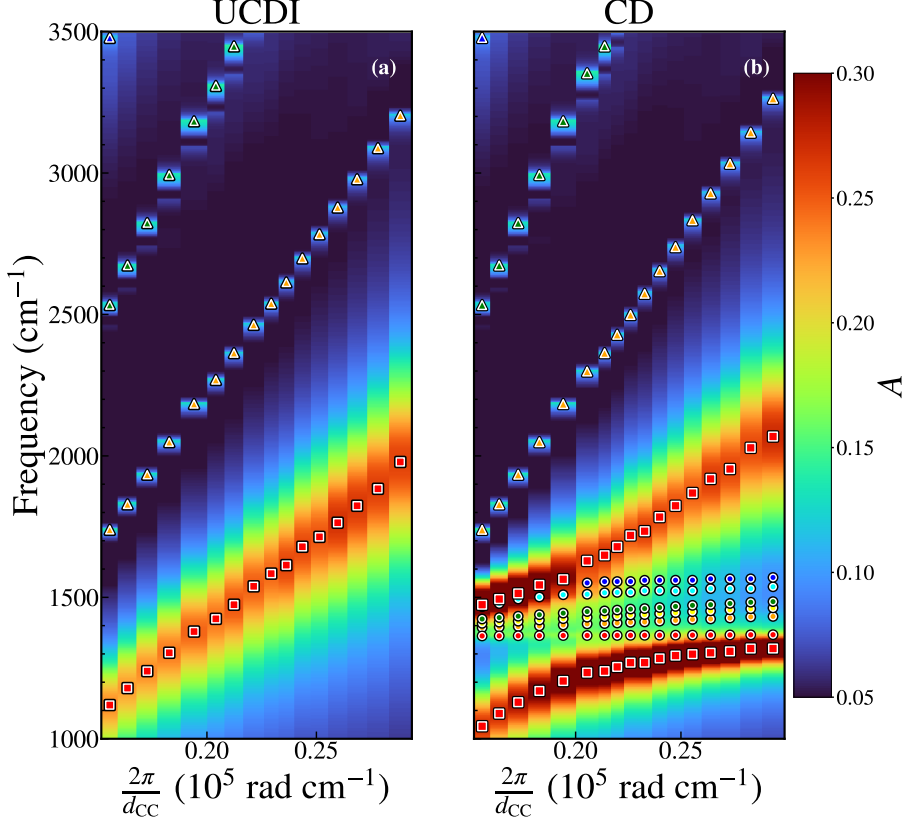


Figure 3.10: (a) Absorptance spectra for the UCDI vs $\frac{2\pi}{d_{CC}}$ plotted as a color map. The symbols indicate the peaks in the absorptance spectra. The triangular symbols are due to Rayleigh anomalies, while the square symbols indicate the plasmon-polariton, which shifts linearly with $\frac{2\pi}{d_{CC}}$. (b) Absorptance spectra for the CD vs $\frac{2\pi}{d_{CC}}$ plotted as a color map. The symbols indicate the peaks/shoulders in the absorptance spectra. The triangular symbols are due to Rayleigh anomalies, while the square symbols show the interaction between plasmon-polariton in the nanopatterned Au film and the bulk phonon-polariton in the hBN. The interpretation of the features labeled by the circular symbols are given in the main text.

distributions are accessible to experimental techniques. In order to gain additional insight, the cross-sectional field maps (which are not accessible experimentally) are also shown in Fig. 3.11 directly below the corresponding planar data. Fig. 3.11 presents data after y -polarized excitation at three different frequencies, *i.e.*, below the hBN reststrahlen band at $\nu = 1200 \text{ cm}^{-1}$, within the hBN reststrahlen band at $\nu = 1500 \text{ cm}^{-1}$ and above the reststrahlen band at $\nu = 1700 \text{ cm}^{-1}$. The data excited at frequencies above and below the reststrahlen band is expected to be predominantly plasmonic in nature for BD, UCDI and

CD; this is borne out by the data in Fig. 3.11 (a)–(h) and (q) – (x), respectively. In particular, in the case of the BD, there are field hot-spots at the inner corners of the cross pattern. In both the UCDI and CD, these hot spots are reproduced and smeared out; in the case of the CD this is due the presence of the hBN capping layer. The UCDII exhibits no evidence of field hot-spot behavior as expected for a structure without a nanostructured metallic layer. It is noticeable that in all the above cases the only rapid variations in the field take place right at the boundary between the metal/dielectric cross and the enclosed vacuum. Based upon the above discussion, the field maps shown in panes (b) and (r) of Fig. 3.11 are taken to be a prototypical signature of plasmonic behavior in the capped devices considered in this chapter. In the case of the CD, see Fig. 3.11 (d) and (t), the field maps are very similar to those depicted in Fig. 3.11 (b) and (r), indicating that the behavior observed is predominately plasmonic when this device is excited either above or below the hBN reststrahlen band.

Excitation of the above devices within the hBN reststrahlen band at $\nu = 1500 \text{ cm}^{-1}$ reveals significantly different behavior. In the case of the BD and UCDI, the planar, Fig. 3.11 (i) and (j), and cross-sectional field maps, Fig. 3.11 (m) and (n), strongly resemble the plasmonic field maps excited outside the reststrahlen band, in particular those excited at $\nu = 1700 \text{ cm}^{-1}$. The UCDII planar field map, Fig. 3.11 (k), exhibited high spatial frequency variations in the y -direction in the region within the cross, although there is comparatively little high spatial frequency variation in the x -direction. This behavior is reproduced outside the cross, but at a noticeably different spatial frequency. An examination of the cross-sectional field map, Fig. 3.11 (o), reveals that there is a guided slab mode within the hBN layer of this device. The CD planar field map, Fig. 3.11 (l), exhibited high spatial frequency variations in both the x - and y -directions in the regions within and outside the cross. The contrast of these spatial variations is somewhat greater than that observed in Fig. 3.11 (k). An examination of the cross-sectional field map, Fig. 3.11 (p), also shows strong evidence of a guided mode within the hBN layer of this device. The high spatial frequency variation

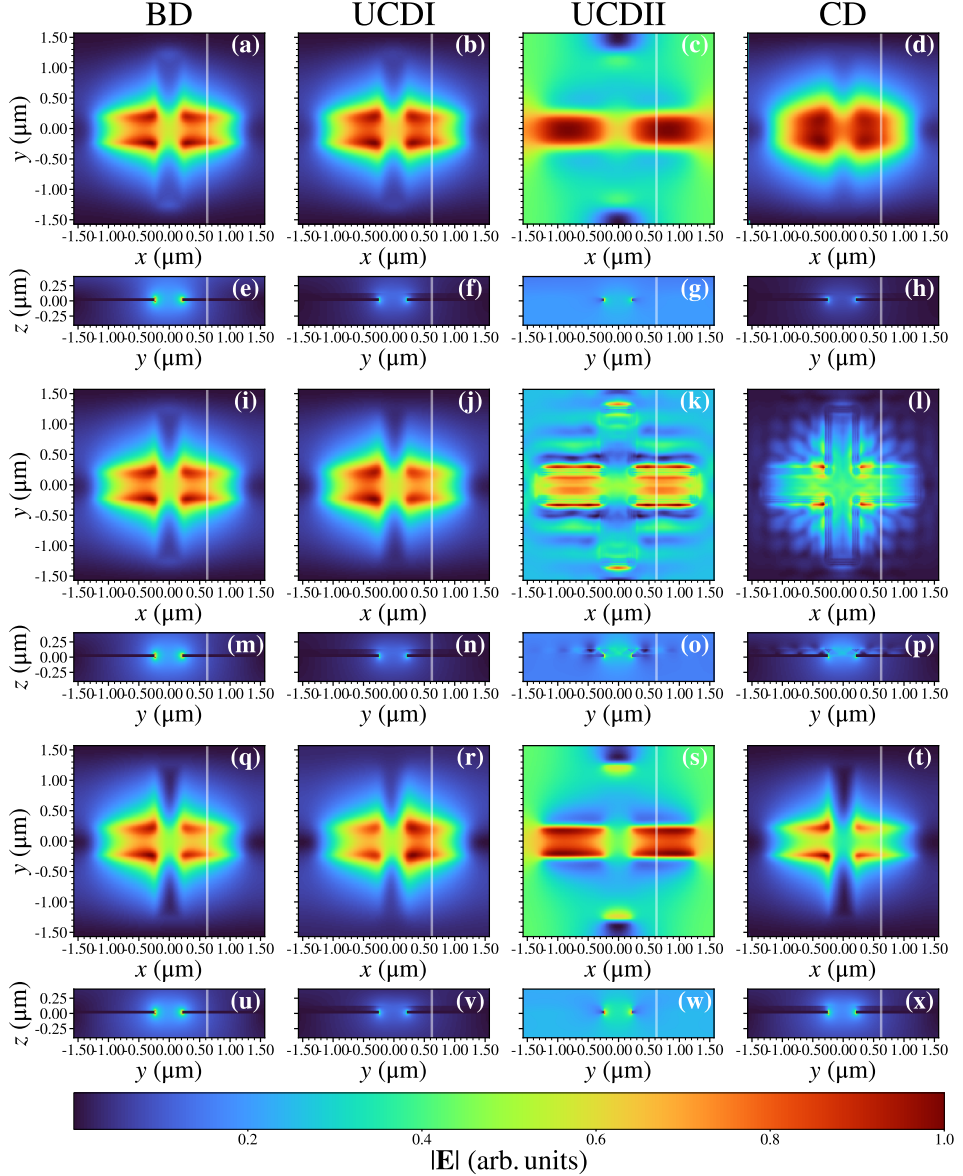


Figure 3.11: Background subtracted and normalized planar and cross-sectional colormaps of the field magnitude for the BD, UCDI, UCDII, and CD with $d_{CC} = 3.14 \mu\text{m}$. Panes (a) – (h) were excited below the reststrahlen band at $\nu = 1200 \text{ cm}^{-1}$. The white lines in the planar colormaps panes (a) – (d) indicate the location of the cross-sectional colormaps in (e) – (h). Panes (i) – (p) were excited in the reststrahlen band at $\nu = 1500 \text{ cm}^{-1}$. The white lines in the planar colormaps panes (i) – (l) indicate the location of the cross-sectional colormaps in (m) – (p). Panes (q) – (x) were excited above the reststrahlen band at $\nu = 1700 \text{ cm}^{-1}$. The white lines in the planar colormaps panes (q) – (t) indicate the location of the cross-sectional colormaps in (u) – (x).

observed in the planar field maps and the guided mode behavior observed in the cross-

sectional field maps is taken to be a prototypical signature of polaritonic behavior in the devices considered in this paper.

Two notable differences between the behavior of UCDII and the CD are as follows: (i) the contrast in the spatial field variation is a factor of $\sim 2 - 3$ times higher in the CD than the UCDII suggesting that the plasmon plays a role in coupling energy into the hBN phonon-polaritons. (ii) the spatial variation of the field in the x -direction in the CD, which is not present in the UCDII device, indicate that the plasmon also plays a key role in launching phonon-polaritons into different directions within the hBN layer.

For potential comparison to experiment, it is useful to analyze lineouts from field data of the type presented in Fig. 3.11. A series of lineouts for a CD with $d_{CC} = 3.14 \mu\text{m}$ is shown in Fig. 3.12 (a). The electric fields were frequency resolved in the range $\nu = 1490 - 1570 \text{ cm}^{-1}$. The position of the lineout is indicated by the white line in the insert of Fig. 3.12 (b). Lineout data was only extracted outside of the cross region, *i.e.*, where the hBN was supported by an Au layer. The peaks in $|\mathbf{E}|$ were determined using the peak fitting algorithm described above. A phonon-polariton wavelength was assigned by calculating the averages of the differences between successive peaks. These wavelengths were found to lie in the range 140 – 330 nm. These data were used to construct a dispersion curve as shown in Fig. 3.12 (b). Additional insight can be obtained by examining the individual field components [90], thus a similar process was applied to the E_y lineout data as shown in Fig. 3.12 (c) and (d). As can be seen by comparing the plots in Fig. 3.12 (b) and (d), the computed dispersion curves are similar although not identical, particularly at low values of q .

Fig. 3.13 (a) reproduces the far-field absorption spectrum from Fig. 3.9 (c) for convenient comparison with the near field data. Fig. 3.13 (b) shows E_y lineouts in the y -direction for frequencies in the range $\nu = 1000 - 1800 \text{ cm}^{-1}$ at intervals of 1 cm^{-1} . As can be seen from this figure, the region of highest field strength is in the vicinity of the inner Au-vacuum boundary within the cross (vacuum below the hBN layer), however features can be clearly resolved outside the cross (gold below the hBN layer). Broad features attributed to plasmons

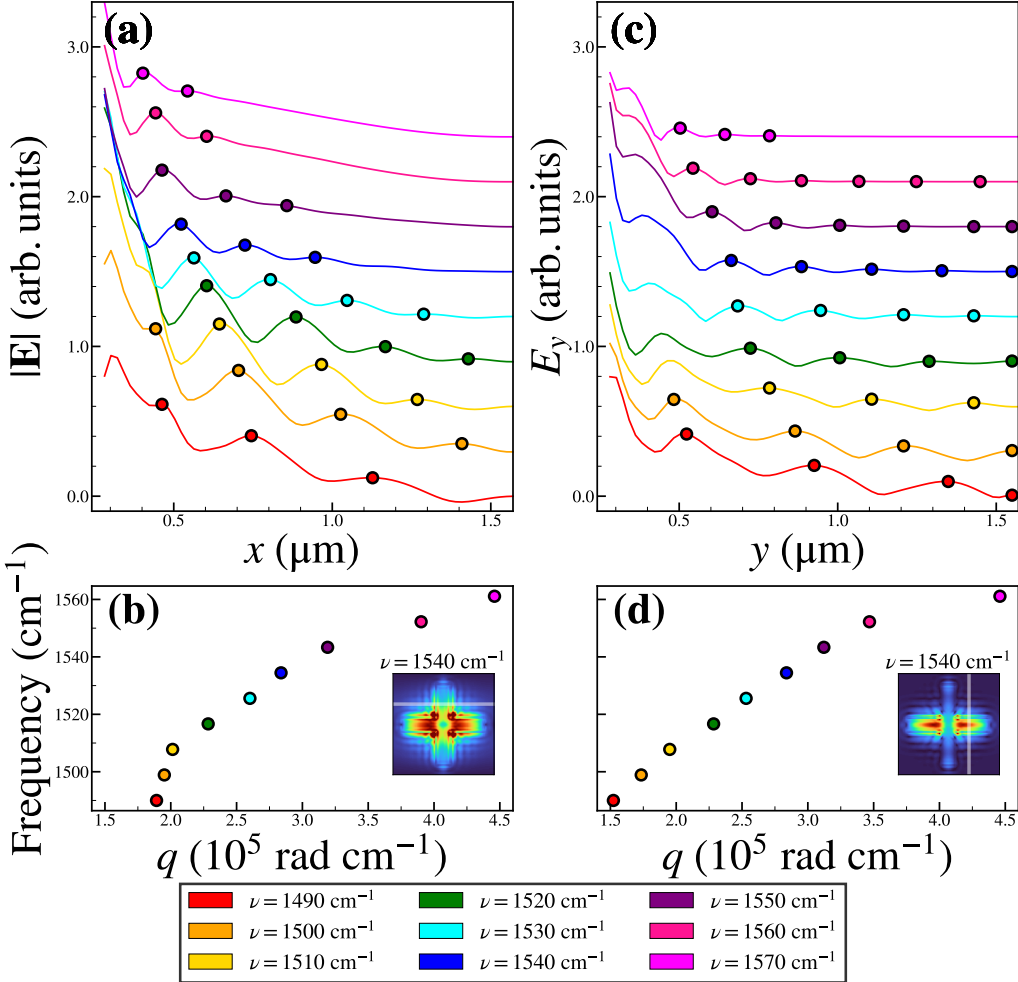


Figure 3.12: (a) Lineouts of the magnitude of the electric field for a range of excitation frequencies in the reststrahlen band $\nu = 1490 - 1570 \text{ cm}^{-1}$. The circular dots indicate peaks in the lineout. (b) Dispersion curve constructed from the peak data in pane (a). (c) Lineouts of the y -component of the electric field for a range of excitation frequencies in the reststrahlen band $\nu = 1490 - 1570 \text{ cm}^{-1}$. The circular dots indicate peaks in the lineout. (d) Dispersion curve constructed from the peak data in pane (c). The inserts in panes (b) and (d) show the position of the lineouts in panes (a) and (c).

can be observed both below and above the reststrahlen band; these features extend from inside the vacuum region into the gold region. Within the frequency range spanned by the reststrahlen band, multiple branches can be observed in both the vacuum and Au regions.

Particularly notable at high frequencies (*i.e.*, in the range $\nu = 1550 - 1800 \text{ cm}^{-1}$), the signal is much stronger in the region inside the cross structure than the region outside. This

effectively applies a square windowing function to the signal which modulates the Fourier transformed data in Fig. 3.13 (c), introducing minima at values of $q = 2n\pi/w$, *i.e.*, the zeros of $\text{sinc}(kw/2)$, where w is the width of the cross as defined in Fig. 3.3 and n is a non-zero integer. Fig. 3.13 (c) shows the spatial Fourier transform of the (full spatial lineout) data described above. The resulting plot of $|E_y(q, \omega)|$ enables the phonon-polariton dispersion curves to be visualized. In order to aid the interpretation of the data in Fig. 3.13 (c), theoretical phonon-polariton dispersion curves were calculated for a pair of three-layer thin-film structures: (i) Vacuum/hBN/Vacuum, and (ii) Vacuum/hBN/Au.

It should be noted that the q -resolution of the data in Fig. 3.13 (c) is limited to $\Delta q = 2\pi/d_y$ as described in Press *et al.* [91] and is an intrinsic property of the discrete Fourier transform of a periodic function. In order to make this image easier to interpret, this data has been interpolated using a cubic spline interpolation algorithm.

Fig. 3.13 (c) shows the spatial Fourier transform of the (full spatial lineout) data described above. The resulting plot of $|E_y(q, \omega)|$ enables the phonon-polariton dispersion curves to be visualized. In order to aid the interpretation of the data in Fig. 3.13 (c), hBN phonon-polariton dispersion curves are calculated by extending the method described in the supplemental materials of the 2014 paper by Dai *et al.* [24] to four-layer systems. In particular, the Fresnel reflection coefficients were calculated using the transfer matrix method as detailed in Chapter 8 of Orfanidis [92]. The hBN phonon-polariton dispersion curves were then calculated by finding the maxima of the imaginary part of the complex Fresnel reflection coefficient at real momenta. The curves in green are for the Vacuum/hBN/Vacuum/SiO₂ structure, while the curves in red are for the Vacuum/hBN/Au/SiO₂ structure. Both transverse magnetic (TM) and transverse electric (TE) modes can be calculated using this method. The TM dispersion curves calculated in this manner were in good agreement (in their region of overlapping validity, *i.e.*, at high wavevector) with the dispersion curves calculated using the quasistatic approximation [24, 25] for the three-layer (no substrate) systems, Vac-

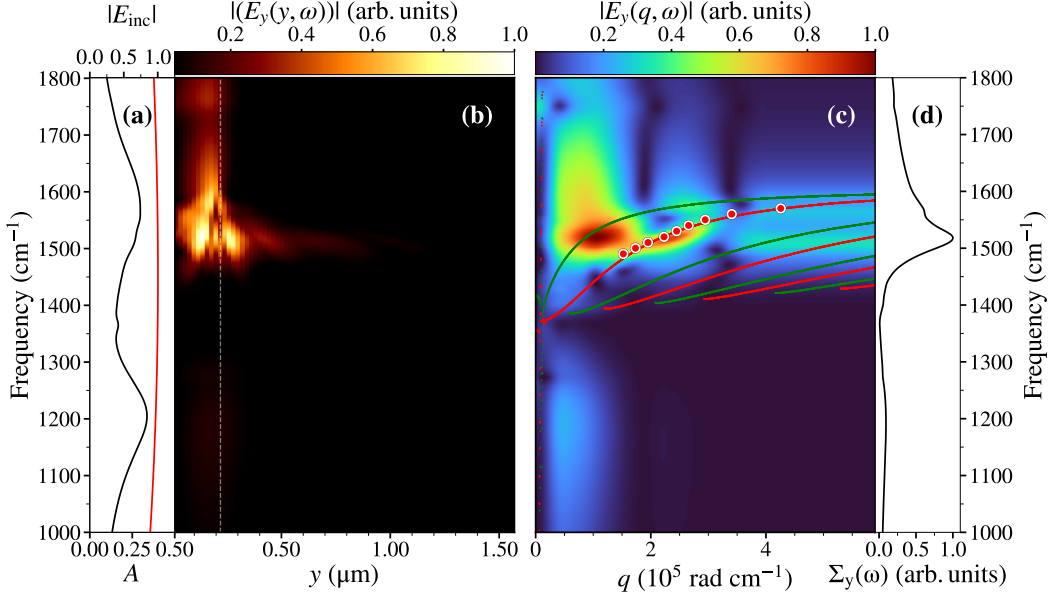


Figure 3.13: Phonon-polariton dispersion curves in the CD. (a) Black curve – lower scale: The far-field absorptance spectrum. Red curve – upper scale: The magnitude of the excitation field used to generate the data in the following panes. (b) E_y lineouts (at the position of the white lines in Fig. 3.11) for frequencies in the range $\nu = 1000 - 1800 \text{ cm}^{-1}$ with a spectral resolution of 1 cm^{-1} . The spatial extent of the data displayed in this pane is from the center to the edge of the unit cell to avoid duplication. The white dotted line in this pane indicates the boundary between vacuum and Au. (c) The spatial Fourier transform of the (full spatial lineout) data presented in pane (b). This data has been interpolated using a cubic spline algorithm. The resulting plot of $|E_y(q, \omega)|$ enables the phonon-polariton dispersion curves to be visualized. The red and green theoretical dispersion curves are calculated as described in the text. The red dots are the dispersion curve data from Fig. 3.12 (b). (d) The spectral content of the data in pane (c) obtained by integrating over q .

uum/hBN/Vacuum, and Vacuum/hBN/Au, respectively.

$$q(\omega) = -\frac{\Psi}{d_{\text{hBN}}} \left[\tan^{-1} \left\{ \frac{\varepsilon_0}{\varepsilon_{x,y}(\omega)\Psi} \right\} + \tan^{-1} \left\{ \frac{\varepsilon_s}{\varepsilon_{x,y}(\omega)\Psi} \right\} + n\pi \right], \quad (3.1)$$

where $\Psi = -i\sqrt{\varepsilon_z(\omega)/\varepsilon_{x,y}(\omega)}$ and $\varepsilon_{x,y,z}(\omega)$ are the components of the hBN dielectric tensor, $\varepsilon_{\text{hBN}}(\omega)$. $\varepsilon_s = \varepsilon_0$, the permittivity of free space for the Vacuum/hBN/Vacuum structure and

$\varepsilon_s = \varepsilon_{\text{Au}}(\omega)$ for the Vacuum/hBN/Au structure; n is an integer and all other quantities are defined above. The advantage of Eq. 3.1 is that it explicitly highlights that the phonon-polariton dispersion clearly has multiple branches, and that those branches are labelled by n . The major difference between the four-layer and three-layer TM dispersion curves is that the $n = 0$ mode for the Vacuum/hBN/Vacuum/SiO₂ four-layer structure is asymptotic to a slightly lower frequency than the same mode in the corresponding three-layer structure, all other TM modes are very similar.

As can be seen in Fig. 3.13 (c), the upper green curve (dispersion curve for the Vacuum/hBN/Vacuum/SiO₂ structure with $n = 0$) and the upper red curve (dispersion curve for the Vacuum/hBN/Au/SiO₂ structure with $n = 1$) overlap regions with large values of $|E_y(q, \omega)|$. The dispersion curve data shown in Fig. 3.12 (d) is plotted on top of the data shown in Fig. 3.13 (c) and good agreement is observed between these data (plotted as red circles) and the red $n = 1$ dispersion curve for the Vacuum/hBN/Au/SiO₂ structure. It is notable that the value of $|E_y(q, \omega)|$ decreases strongly with increasing values of n .

The spectral content of the data in Fig. 3.13 (c) is obtained by integrating over q to yield the quantity denoted $\Sigma_y(\omega)$, which is plotted in Fig. 3.13 (d). The resulting spectrum, while exhibiting the general features of the far-field spectrum, shows three notable differences. Firstly, this spectrum suppresses both the residual peak at the hBN TO optical phonon frequency and the low frequency plasmon band centered at $\sim 1200 \text{ cm}^{-1}$ relative to the phonon-polariton signal. Secondly, the fine structure within the hBN reststrahlen band is emphasized, and finally there is a very small additional peak centered at $\sim 1750 \text{ cm}^{-1}$, the origin of which is not understood at this time. The near-field spectrum, $\Sigma_y(\omega)$, therefore emphasizes the slab phonon-polaritons over the bulk phonon-polaritons when compared to the far-field spectrum thus highlighting the importance of using near-field experimental techniques to investigate systems of this kind.

To further investigate the coupling to the hBN phonon-polaritons, the phonon-polariton signal strength in the coupled device was investigated as a function of d_{CC} . In order

to better separate the signal originating from the Vacuum/hBN/Vacuum/SiO₂ and the Vacuum/hBN/Au/SiO₂ regions of the device, a Tukey [93] windowing function was used to mask regions of the real space data in Fig. 3.13 (b) before Fourier transforming that data. The Fourier transformed data that derives from only the Vacuum/hBN/Vacuum/SiO₂ region of the $d_{CC} = 3.14 \mu\text{m}$ device is shown Fig. 3.14 (a). The theoretical dispersion curves for the Vacuum/hBN/Vacuum/SiO₂ structure are overlaid in green. The upper green curve is denoted $\omega_{V,0}(q)$. Similarly, the Fourier transformed data that derives from only the Vacuum/hBN/Au/SiO₂ region of the same device is shown Fig. 3.14 (b) and the theoretical dispersion curves for the Vacuum/hBN/Au/SiO₂ structure are overlaid in red. The upper red curve is denoted $\omega_{Au,1}(q)$. Figs. 3.14 (c) and (d) are the same as Figs. 3.14 (a) and (b), respectively, but for the $d_{CC} = 3.94 \mu\text{m}$ device.

A region of Fig. 3.14 (a) was defined by q in the range $0.15 \times 10^5 - 4.15 \times 10^5 \text{ rad cm}^{-1}$ and ω in the range $\omega_{V,0}(q) \pm 88 \text{ cm}^{-1}$. $|E_y(q, \omega)|$ was integrated over this region to yield the quantity Σ_V . Similarly, a region of Fig. 3.14 (b) was defined by q in the range $0.8 \times 10^5 - 4.8 \times 10^5 \text{ rad cm}^{-1}$ and ω in the range $\omega_{Au,1}(q) \pm 88 \text{ cm}^{-1}$. $|E_y(q, \omega)|$ was integrated over this region to yield the quantity Σ_{Au} . This process was repeated for devices with values of d_{CC} in the range $2.5 - 4.5 \mu\text{m}$, the latter being the largest structure that could be simulated using available computational resources. $\Sigma_V(d_{CC})$ was normalized to its maximum value which occurred at $d_{CC} = 3.74 \mu\text{m}$ and is plotted in green in Fig. 3.14 (e). $\Sigma_{Au}(d_{CC})$, which is plotted in red in Fig. 3.14 (e), was also normalized to the maximum value of $\Sigma_V(d_{CC})$, so that the relative strengths of these two quantities could be directly compared. $\Sigma_{Au}(d_{CC})$ is approximately half the strength of $\Sigma_V(d_{CC})$, but exhibits a similar dependence on d_{CC} , with the exception that its maximum value occurs at $d_{CC} = 3.94 \mu\text{m}$. Given the level of numerical noise in the Fig. 3.14 (e) data, this apparent shift in the maximum value may not be physically significant.

In order to gain insight into the behavior of both $\Sigma_V(d_{CC})$ and $\Sigma_{Au}(d_{CC})$, the far-field coupled device (CD) absorptance spectra of Fig. 3.9 (c) were integrated over the reststrahlen

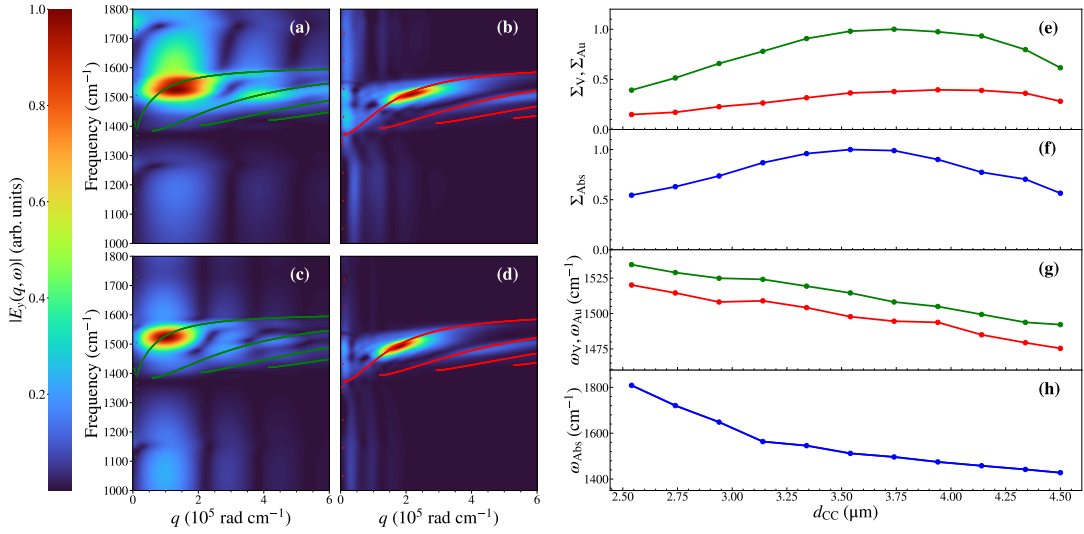


Figure 3.14: Vacuum/hBN/Vacuum/SiO₂ and Vacuum/hBN/Au/SiO₂ phonon-polariton signal strength and frequency dependence in the CDs as a function of d_{CC} . (a) The spatial Fourier transform of the Vacuum/hBN/Vacuum/SiO₂ masked data from pane Fig. 3.13 (b). The green theoretical dispersion curves are for the Vacuum/hBN/Vacuum/SiO₂ system. (c) The spatial Fourier transform of the Vacuum/hBN/Au/SiO₂ masked data from pane Fig. 3.13 (b). The red theoretical dispersion curves are for the Vacuum/hBN/Au/SiO₂ system. Pane (c) is the same as pane (a), but for the $d_{CC} = 3.94 \mu\text{m}$ device. Pane (d) is the same as pane (b), but for the $d_{CC} = 3.94 \mu\text{m}$ device. (e) Green: The integrated Vacuum/hBN/Vacuum/SiO₂ phonon-polariton signal strength plotted as a function of d_{CC} . Red: The integrated Vacuum/hBN/Au/SiO₂ phonon-polariton signal strength plotted as a function of d_{CC} . (f) Blue: The far-field absorptance spectra from Fig. 3.9 integrated over the spectral region of the reststrahlen band plotted as a function of d_{CC} . (g) Green: The frequency at which the peak of the Vacuum/hBN/Vacuum/SiO₂ phonon-polariton signal strength occurs plotted as a function of d_{CC} . Red: The frequency at which the peak of the Vacuum/hBN/Au/SiO₂ phonon-polariton signal strength occurs plotted as a function of d_{CC} . (h) Blue: The peak of the high frequency far-field absorptance band from Fig. 3.9. The lines in panes (e), (f), (g) and (h) are guides to the eye.

band to yield the quantity Σ_{Abs} , which was normalized to its maximum value, which occurred at $d_{CC} = 3.54 \mu\text{m}$. $\Sigma_{Abs}(d_{CC})$ is plotted in blue in Fig. 3.14 (f). A comparison of Fig. 3.14 (e) and (f) suggests that the variation of $\Sigma_V(d_{CC})$ and $\Sigma_{Au}(d_{CC})$ with d_{CC} is dominated by the overlap of the respective absorptance spectrum with the reststrahlen band. That the peaks

of $\Sigma_V(d_{CC})$ and $\Sigma_{Au}(d_{CC})$ do not occur exactly at the peak of $\Sigma_{Abs}(d_{CC})$ could possibly be due to (i) long wavelength (small q) phonon-polaritons becoming quenched in the smaller (d_{CC}) structures or (ii) the presence of a Rayleigh anomaly, which shifts into the reststrahlen band for devices with $d_{CC} > 3.94 \mu\text{m}$.

A careful examination of Fig. 3.14 (a), (b), (c) and (d) reveals that the phonon-polaritons excited in the $d_{CC} = 3.94 \mu\text{m}$ are downshifted in both frequency and wave-vector compared to the corresponding phonon-polariton in the $d_{CC} = 3.14 \mu\text{m}$ device. This behavior is systematic as is demonstrated by the data in Fig. 3.14 (g), which shows both a plot of the frequency at which the maximum Vacuum/hBN/Vacuum/SiO₂ phonon-polariton signal occurs (plotted in green) and a plot of the frequency at which the maximum Vacuum/hBN/Au/SiO₂ phonon-polariton signal occurs (plotted in red) as a function of d_{CC} . The dependence of the value of q at which the maximum phonon-polariton signals occur as function of d_{CC} (not shown) follow a similar trend to the frequency data. The data (plotted in blue) in Fig. 3.14 (h) shows the peak of the high frequency far-field absorptance band from Fig. 3.9. The above data and associated discussion indicates that the frequency/wavevector of the phonon-polariton can be tuned over a limited spectral region by varying d_{CC} . This tunability may be of import for potential applications of these devices.

3.6 Conclusions

The excitations that occur in a hBN/nanopatterned Au device have been investigated using the Finite-Difference Time-Doman (FDTD) method. In order to gain a more detailed understanding of the coupling between the phonon-polaritons in the hBN layer and the plasmon-polaritons in the nanopatterned Au layer, the far- and near-field properties of this coupled device (CD) were compared with the properties of three other uncoupled devices denoted BD (supports plasmon-polaritons only), UCDI (supports plasmon-polaritons only) and UCDII (supports phonon-polaritons only). An examination of the far-field absorptance

spectra of the above devices show that in the coupled device the absorptance peak, associated with the plasmon-polariton in UCDI, splits due to the interaction with the bulk phonon-polariton in hBN, while an examination of the absorptance fine-structure provides evidence of slab phonon-polaritons in hBN.

An investigation of the near-field electric field distributions enables the slab phonon-polaritons to be identified and categorized according to mode number per Eq. 3.1 and supporting layer, *i.e.*, vacuum or Au. A comparison of the field maps for the CD and UCDII show that the presence of the plasmon-polaritons in the CD increases the contrast in the spatial electric field variation indicating that the plasmon plays a key role in both coupling energy into the hBN phonon-polaritons and in launching phonon-polaritons into different directions within the hBN layer.

By examining the dependence of the phonon-polariton excitation on the device periodicity, d_{CC} , it was observed that the frequency/wavevector of the phonon-polariton can be tuned by varying d_{CC} . Furthermore the strength of the phonon-polariton signal varies with d_{CC} and that variation is dominated by the spectral overlap of the far-field absorptance spectrum with the reststrahlen band.

Chapter 4

Coupling of phonon-polaritons with
plasmon-polaritons in a layered device
comprising hBN on a nanopatterned
hexagonal array of circular apertures in
a Ag layer

4.1 Introduction

The device studied in this chapter is an infinite hBN sheet over an hexagonal array of circular apertures in Ag. This structure was selected because it emphasizes how changes in symmetry, metallic layer and substrate can impact the device performance. The circular aperture / hexagonal lattice symmetry acts as a prototype structure for a suite of nanostructures that can be realized experimentally using shadow-sphere lithography [58]. The hexagonal geometry is also of interest because it may form the basis of structures that support topologically protected unidirectional chiral edge modes [37, 38]. Si was selected as a substrate

because (i) it is a ubiquitous substrate for experimental device development, (ii) it can be approximated as optically inert at IR frequencies, and (iii) its high refractive index shifts the Rayleigh anomalies into the spectral region of interest allowing the effect of resonant Rayleigh anomalies on the device performance to be evaluated.

Specific details on how these devices were modelled within FDTD simulations is given in the following section.

4.2 Preliminary Measurements

The details of the nanopatterned structure simulated in this chapter are shown in Fig. 4.1. The structure comprised of an 80 nm sheet of hexagonal boron nitride (hBN) deposited on a 50 nm thick film of nanopatterned Ag atop of a Si substrate. The Ag film was patterned with circular holes of radius 0.68 μm arranged in a hexagonal lattice with a distance between the centers of d_{CC} , which was varied during this work. The pattern chosen offers the advantage of three parameters that may be varied to tune the the grating's plasmonic resonance to the TO resonance of hBN. These parameters are the Ag film thickness, d_{Ag} , the hole radius, r_c , and the periodicity d_{CC} , which must have the ratios $d_{\text{CC}} = d_x = \frac{d_y}{\sqrt{3}}$ in the x - and y -directions to maintain a hexagonal array structure. Hexagonal arrays of circular appertures in Au have been shown to exhibit sharper plasmon resonances and greater sensitivity when compared to a similar square array [94].

As described in Chapter 3, broadband, plane wave sources were used to excite structures investigated in this chapter. The sources were x -polarized and propagated in the negative z -direction. Reflection and transmission spectra were calculated using DFT sensors as described in Section 2.5.2. The reflection and transmission sensors were placed at $z = 0.01 \mu\text{m}$ and $z = 1.98 \mu\text{m}$ respectively. To prevent divergence in the simulation caused by edge reflections in the patterned metallic layer, a 50 layer convolutional perfectly matched layer

(CPML) boundary was used in the z -dimension. Periodic boundaries were used in the x - and y - dimensions.

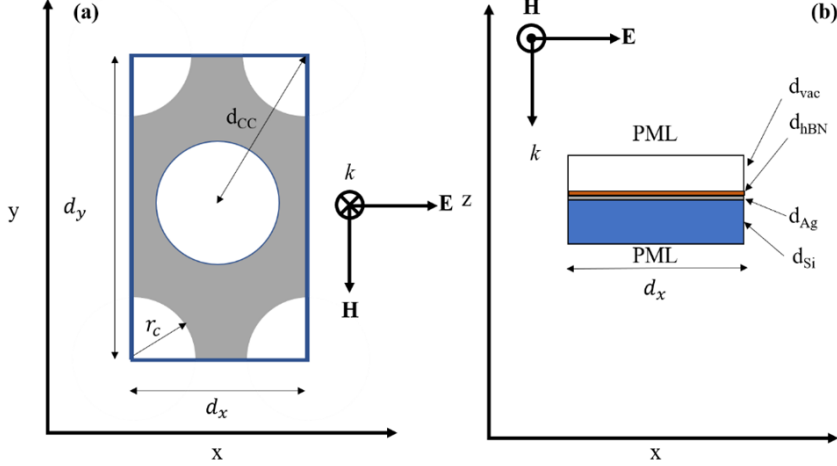


Figure 4.1: Schematic of the hBN/Ag structure simulated on this work. (a) Plane view at the hBN/Ag interface. The symmetry reduced unit cell is outlined in red. (b) Cross-sectional view. CPML: Convolutional perfectly matched layer boundary conditions terminated the z -direction boundaries. Periodic boundary conditions terminated the x and y boundaries. The unit cell lengths in the x - and y -directions are d_x and d_y , respectively. The layer thicknesses beyond the CPMLs were $d_{\text{vac}} = 0.87 \mu\text{m}$, $d_{\text{hBN}} = 80 \text{ nm}$, $d_{\text{Si}} = 1.0 \mu\text{m}$, $d_{\text{Ag}} = 50 \text{ nm}$. The radius of the holes is $r_C = 0.68 \mu\text{m}$. The distance between the centers of the cylindrical holes is $d_{\text{CC}} = d_x$, $d_y = \sqrt{3}d_{\text{CC}}$. The directions of the \mathbf{E} -field, \mathbf{H} -Field and propagation vector \mathbf{k} is shown in both panes.

As discussed in detail in Section 2.2 the various components of the device were modelled as follows. The hBN layer was simulated using a tensor Lorentz model, as described in Chapter 2. The Ag film was simulated using the Debye-Drude model that was also detailed in Chapter 2. This model was fit to the wavelength dependent complex epsilon data from in the Handbook of Optical Constants of Solids I-III [95] and the following parameters were extracted: $\varepsilon_\infty = 1.0$, $\varepsilon_s = 343.8$, $\tau_0 = 7.90 \times 10^{-15} \text{ s}$, and $\sigma = 3.32 \times 10^6 \text{ Sm}^{-1}$. The Si substrate was simulated using a simple dielectric with relative permittivity $\varepsilon_{\text{Si}} = 11.7$. In order to validate the models of the dispersive materials used in this work, thin films of Ag and hBN in vacuo were simulated and the normal incidence absorptance, $A(\omega)$, spectrum

Table 4.1: Simulational Parameters

Symbol	Value	Units	Description
Simulational Meta-Parameters			
Δx	20	nm	Spatial step in x -direction
Δy	20	nm	Spatial step in y -direction
Δz	2	nm	Spatial step in z -direction
Δt	5.945×10^{-18}	s	Time step
n_x	$d_{\text{CC}}/\Delta x$	N.A.	Number of steps in x -direction
n_y	$d_{\text{CC}}/\Delta y$	N.A.	Number of steps in y -direction
n_t	$(10^6, 500 \times 10^3)$	N.A.	Number of time steps (near-field, far-field)
n_{PML}	50	N.A.	Number of PML layers in $\pm z$ -direction
Materials Parameters – Ag			
ε_∞	1.0	N.A.	High-frequency ε
ε_s	343.74	N.A.	Low-frequency ε
τ_0	7.90×10^{-15}	s	Relaxation time
σ	3.32×10^6	Sm^{-1}	Conductivity
Materials Parameters – hBN			
$\varepsilon_{x,y}(\infty)$	4.87	N.A.	High-frequency ε in the x, y -directions
$\varepsilon_z(\infty)$	2.96	N.A.	High-frequency ε in the z -direction
$S_{x,y}$	1.83	N.A.	Dimensionless coupling factor in the x, y -directions
S_z	0.61	N.A.	Dimensionless coupling factor in the z -direction
$\hbar\omega_{x,y}$	170.1	meV	TO phonon frequency in the x, y -directions
$\hbar\omega_z$	92.5	meV	TO phonon frequency in the z -direction
$\gamma_{x,y}$	3.97	meV	Damping constant in the x, y -directions
γ_z	0.25	meV	Damping constant in the z -direction
Materials Parameters – Substrate, Spacer-layers etc.			
ε_{Si}	11.73	N.A.	Relative permitivity of Si

for each of the films was calculated using $A(\omega) = 1 - [T(\omega) + R(\omega)]$, where $T(\omega)$ and $R(\omega)$ are the transmittance and reflectance spectra, respectively. These absorptance spectra were compared with the absorptance spectra calculated for the corresponding film using the transfer matrix (TM) method [61] and excellent agreement between the two methods was observed. Further discussion of the material model validation can be found in Section 2.2.6.

The simulational meta-parameters and the materials parameters used to simulate the devices described in this chapter are given in table 4.1.

As in Chapter 3, in addition to the structure, denoted the “coupled device” (CD), depicted in Fig. 4.1, several other auxiliary structures were simulated. The “bare device” (BD), this device is identical to the coupled device, but with the hBN layer removed. This device does not support phonon-polaritons. The “uncoupled device I” (UDCI), this device is identical to the coupled device, but with the hBN layer replaced with an equal thickness anisotropic layer that has $\varepsilon_k(\infty)$ equal to the values for hBN, but the resonant behavior removed by setting $S_k = 0$. This device does not support phonon-polaritons.

In order to investigate the effect of tuning the plasmon resonance through the hBN reststrahlen band, a series of FDTD simulations were performed at a range of distances between the nearest neighbor centers of the circles, (*i.e.*, d_{CC} in the range $2.14 - 2.78 \mu\text{m}$). The resulting $R(\omega)$, $T(\omega)$, and $A(\omega)$ spectra are shown in Fig. 4.2. Similarly to the spectra in Fig. 3.4 a clear red shift of the main spectral features is observed as d_{CC} was increased. In contrast to Fig. 3.4 the shape of the reflectance and transmittance spectral resonances vary with respect to changes in d_{CC} . In Fig. 4.2 (a) the reflectance resonance troughs decreased as d_{CC} increased while the transmittance resonance peaks increased as d_{CC} increased. However, similarly to the absorptance spectra shown in Fig. 3.4 (c) the plasmon resonance in Fig. 4.2 (c) varied by less than $\pm 10\%$ of the total peak height.

The most striking effect in Fig. 4.2 are the cusps (troughs) that occur in the spectral region $1200 - 1600 \text{ cm}^{-1}$ of the transmittance spectra in Fig. 4.2 (b). These cusps are due to Rayleigh anomalies [87–89]. For normal incidence, the frequencies at which the Rayleigh anomalies occur is given by [89]

$$\frac{\omega}{c} = \frac{1}{n_{\text{sub}}} |r\mathbf{g}_1 + s\mathbf{g}_2|, \quad (4.1)$$

where n_{sub} is the refractive index of the substrate, \mathbf{g}_1 and \mathbf{g}_2 are the grating wavevectors, and r and s are integers. For an hexagonal lattice as is studied in this chapter, $\mathbf{g}_1 = \frac{2\pi}{d_{CC}} \left(1, \frac{-1}{\sqrt{3}}\right)$ and $\mathbf{g}_2 = \frac{2\pi}{d_{CC}} \left(0, \frac{2}{\sqrt{3}}\right)$. These are the reciprocal lattice vectors of the hexagonal basis vectors,

$\mathbf{a}_1 = (d_{CC}, 0)$ and $\mathbf{a}_2 = \left(\frac{d_{CC}}{2}, \frac{\sqrt{3}d_{CC}}{2}\right)$, respectively. For $(r, s) = (1, 0), (0, 1)$, etc., the frequencies predicted by Eq. 4.1 are in excellent agreement with the minima of the cusps in Fig. 4.2 (b). The small cusps that occur in the spectral region $> 2000\text{ cm}^{-1}$ of the transmittance spectrum in Fig. 4.2 (b) and are more clearly seen as small “shark fin” peaks in the absorptance spectra in Fig. 4.2 (c), are in good agreement with the frequencies predicted by Eq. 4.1 with $(r, s) = (1, -1), (-1, 1)$, etc.

The overlap of the $(r, s) = (1, 0), (0, 1)$, etc., Rayleigh anomalies with the spectral region surrounding and including the reststrahlen band is a direct consequence of the Si substrate with $n = 3.42$ ($\epsilon_{Si} = 11.7$), used in this device. It is notable that the Rayleigh anomalies modify the absorption spectra. This can be understood as a channeling of energy into a diffracted wave that propagates tangentially to the surface of the grating at the Ag-Si interface. This diffracted wave causes a dip in the transmittance spectrum (peak in the absorptance spectrum) that can overlap the plasmon resonance and thereby modify the plasmon absorption peak. That the Rayleigh anomalies significantly modify the absorption spectra in this manner, means that the far-field properties are not as useful a tool for gaining insight into the plasmon-polariton / phonon-polariton coupling in the devices discussed in this chapter when compared to the devices described in Chapter 3. Additional examples of this absorption modification and its implications will be described in the following sections.

As with the uncoupled device studied in Chapter 3 the addition of a “dielectric” hBN layer resulted in a red shift of certain features. However if the largest absorptance peaks of the $d_{CC} = 2.14\text{ }\mu\text{m}$ devices Fig. 4.2 and Fig. 4.3 in are examined, the frequency at which this peak occurs remains at 1575.8 cm^{-1} . This feature, of unchanging peak position between the BD and the UCDI with the same d_{CC} , appears for all values of $d_{CC} \leq 2.18\text{ }\mu\text{m}$ observed in this study and is a direct consequence of the Rayleigh anomalies modifying the absorptance spectrum as described in the previous section. The structure with $d_{CC} = 2.38\text{ }\mu\text{m}$ was observed to be resonant with the hBN TO phonon frequency.

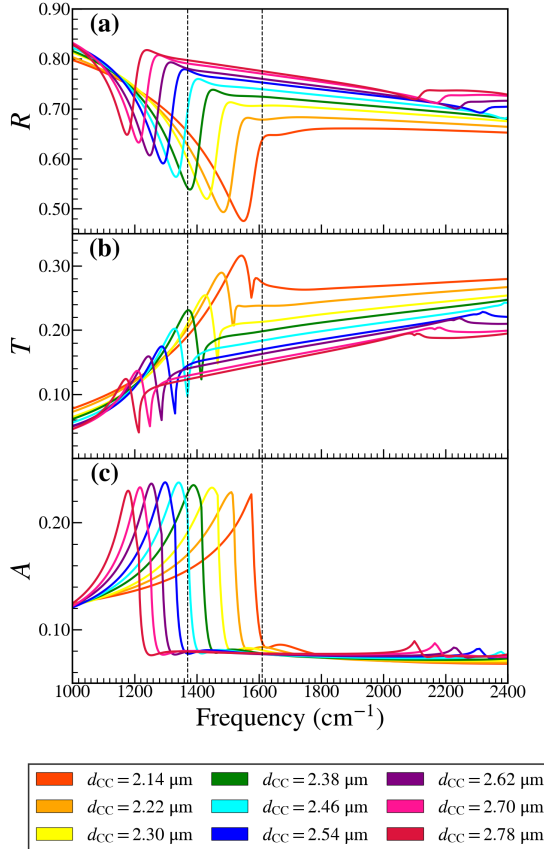


Figure 4.2: The spectra for the BD at a range of d_{CC} values. (a) Reflectance spectra. (b) Transmittance spectra. (c) Absorptance spectra. The vertical black dashed lines in this figure indicate the position of the hBN TO and LO phonon frequencies.

The $R(\omega)$, $T(\omega)$, and $A(\omega)$ spectra for the CD are shown in Fig. 4.4. As with the UCDI and BD the reflectance troughs and transmittance peaks decrease in magnitude as d_{CC} increases. However for the transmittance spectra three separate trough features appear with similar magnitudes. To either side of the TO resonance sharp troughs corresponding to the Rayleigh anomaly-like features appear with similar magnitudes. A larger set of troughs appear along the TO resonance with nearly identical magnitudes. Several interesting features can be discerned. As with the UCD the peak absorptance resonance for devices with $d_{CC} \leq 2.18 \mu\text{m}$ remained unchanged in location. As observed in Chapter 3 the most prominent effect observed in the CD is that the plasmon resonances split into two main peaks. However unlike

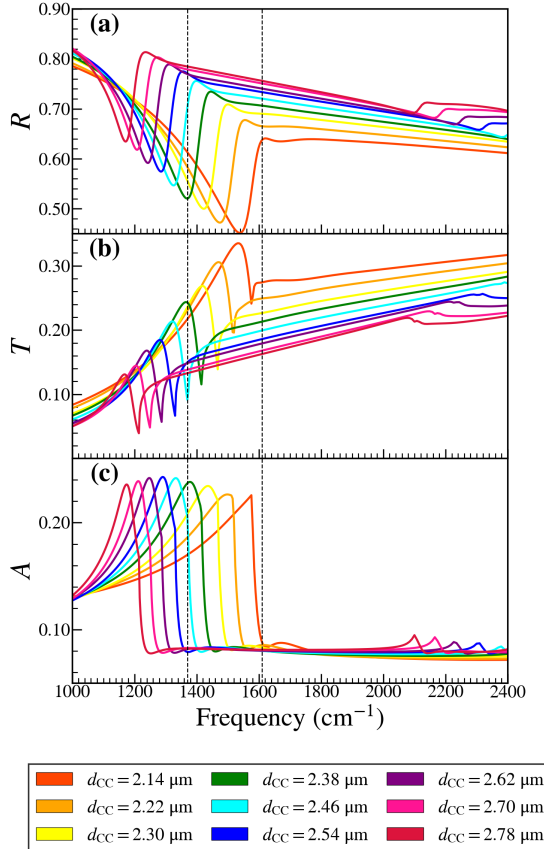


Figure 4.3: The spectra for the UCDI at a range of d_{CC} values. (a) Reflectance spectra. (b) Transmittance spectra. (c) Absorptance spectra. The vertical black dashed lines in this figure indicate the position of the hBN TO and LO phonon.

the Au-cross device, the peaks for $d_{CC} \geq 2.54 \mu\text{m}$ split into a series of peaks asymptoting towards the TO resonance from above and another larger peak below the reststrahlen band. For CDs with $d_{CC} \leq 2.54 \mu\text{m}$ the peaks split to either side of the TO resonance. In addition, there is a smaller peak at 1468 cm^{-1} the position of which is independent of d_{CC} . This peak is close to, but slightly down shifted from the hBN TO phonon frequency.

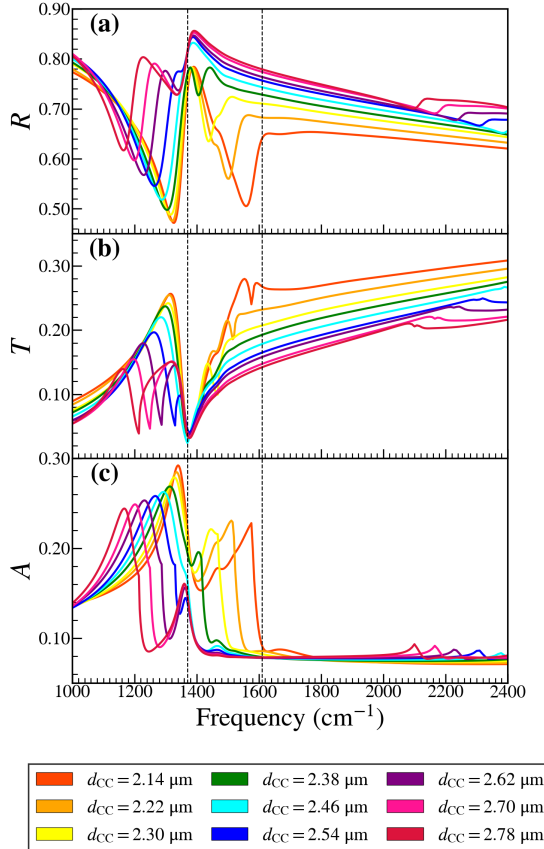


Figure 4.4: The spectra for the CD at a range of d_{CC} values. (a) Reflectance spectra. (b) Transmittance spectra. (c) Absorptance spectra. The vertical black dashed lines in this figure indicate the position of the hBN TO and LO phonon frequencies.

4.3 Far-Field Analysis

In order to investigate the effect of tuning the plasmon resonance through the hBN reststrahlen band, a series of FDTD simulations were performed at a range of distances between the nearest neighbor centers of the circles, (*i.e.*, d_{CC} in the range $2.14 - 2.78 \mu\text{m}$) and the absorptance spectra for the bare device (BD), the uncoupled device I (UCDI) and the coupled device (CD) structures were calculated from the frequency resolved Poynting vector data collected by the planar DFT sensors described in section 2.5.2. Fig. 4.5 shows the absorption spectra calculated for all three devices. The vertical dashed lines in Fig. 4.5 indicate

the positions of the hBN TO and LO phonons at 1360 and 1614 cm⁻¹, respectively. As can be seen from Fig. 4.5 (b), the UCDI structure with $d_{CC} = 2.38 \mu\text{m}$ exhibits a plasmon absorptance peak that is most closely resonant with the hBN TO phonon and this device is the one studied most extensively in this chapter.

Fig. 4.5 (c) shows the absorption spectra for a series of CDs for a range of d_{CC} . The most prominent effect observed in the CD is that the plasmon absorption spectra in the UCDI split into two main peaks in the vicinity of the hBN TO phonon frequency as described in Section 3.2.

Another notable feature that is observed in most of the absorptance spectra depicted in Fig. 4.5 (c) are a series of shoulders that lie between the hBN TO and LO phonon frequencies for devices with $d_{CC} > 2.38 \mu\text{m}$. The position of these shoulders appear to be independent of the splitting of the nearby plasmon resonance.

In order to better analyze the absorptance peak frequency shifts observed in Fig. 4.5, the data in Fig. 4.5(b) and (c) were plotted in colormap form as a function of $\frac{2\pi}{d_{CC}}$. As described in Chapter 3, these plots can act as a proxy for the dispersion curves, although with some limitations. The peak positions in the absorptance spectra were determined using the peak fitting algorithm described in Chapter 3 and plotted on top of the colormaps. In both Fig. 4.6 (a) and (b), the peaks in the spectra indicated by the yellow triangles are due to Rayleigh anomalies [87–89] with indices (0, 1), and (1, -1), calculated using Eq. 4.1. The proximity of the (0, 1) Rayleigh anomalies to the plasmon resonance compromises the utility of Fig. 4.6. Where in Fig. 3.10 the red boxes clearly indicated the location of the plasmon-polariton, in Fig. 4.6 the peak finding algorithm was ambiguous as to whether the resonances were due to the plasmon-polaritons or the RAs, for peaks greater than the hBN TO resonance. However the algorithm was able to identify the lower branch of the split plasmon-polaritons resonances in the CD. When compared to the resonances observed in the UCDI, the plasmon-polariton in UCD splits due to the interaction the bulk phonon-polariton in the hBN. This was further supported by the similar splitting in the plasmon-polariton

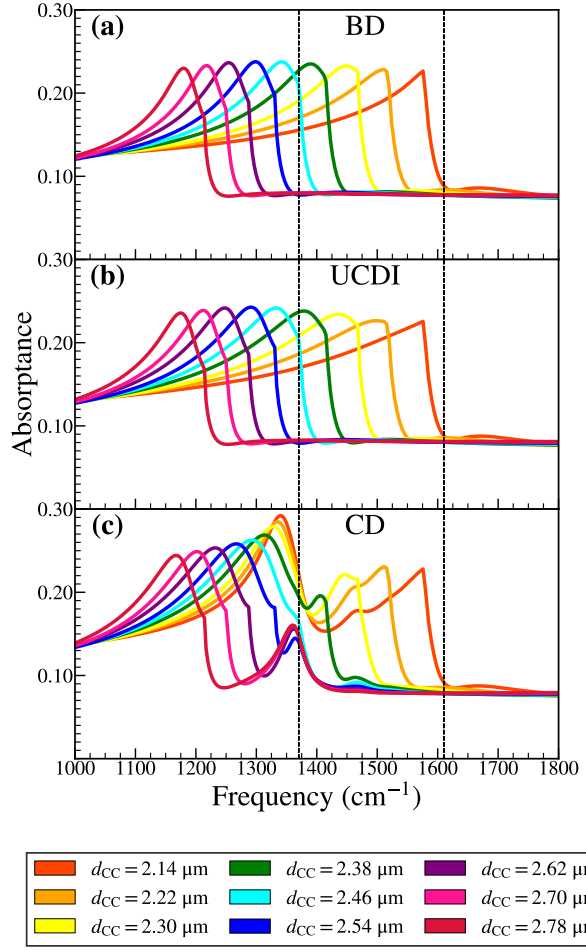


Figure 4.5: (a) The absorptance spectrum of the BD for a range of d_{CC} values. (b) The absorptance spectra of the UCDI. (c) The absorptance spectra of the CD. The vertical black dashed lines in this figure indicate the position of the hBN TO and LO phonon frequencies as described in the main text.

peak that was observed in Chapter 3, and in the reflection data presented by Wan *et al.* [50] in their Fig. 3(a).

4.4 Near-Field Analysis

In order to gain additional insight into the coupling between the plasmon-polaritons in the nanopatterned Au and the phonon-polaritons in hBN film, the electric field distributions,

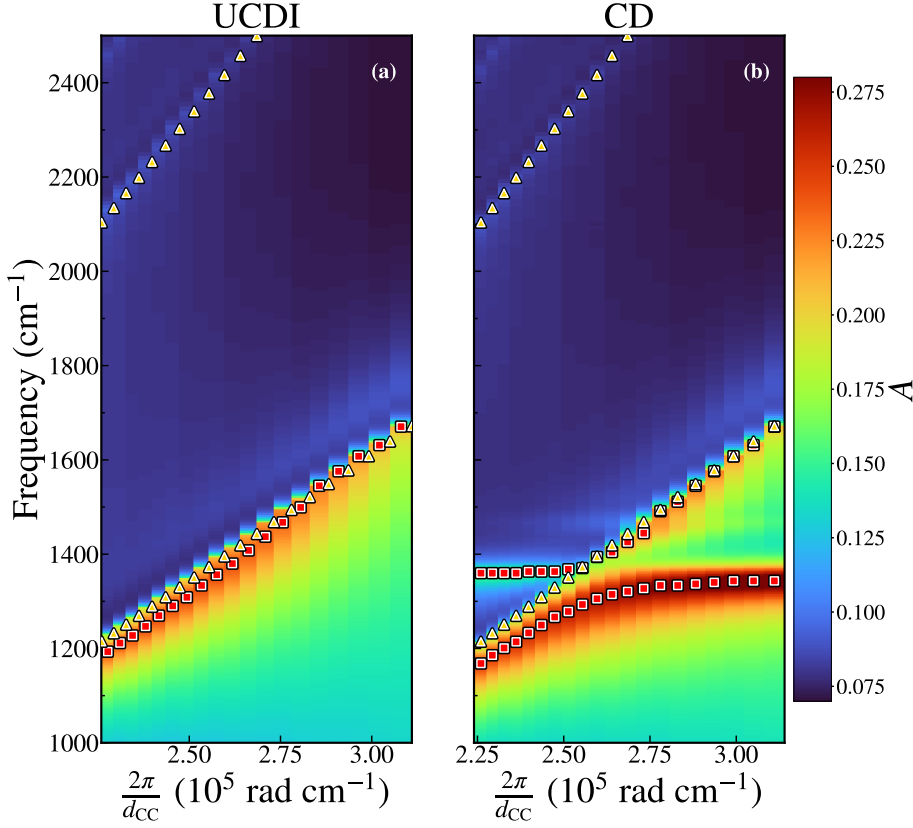


Figure 4.6: (a) Absorptance spectra for the UCDI as a function of $\frac{2\pi}{d_{CC}}$ plotted as a color map. The symbols indicate the peaks in the absorptance spectra. The triangular symbols are due to Rayleigh anomalies, while the square symbols indicate the plasmon-polariton, which shifts inversely to increases in d_{CC} . (b) Absorptance spectra for the CD as a function of $\frac{2\pi}{d_{CC}}$ plotted as a color map. The symbols indicate the peaks/shoulders in the absorptance spectra. The triangular symbols are due to Rayleigh anomalies, while the square symbols show the interaction between plasmon-polariton in the nanopatterned Au film and the bulk phonon-polariton in the hBN.

$|\mathbf{E}|$, at the position of the vacuum/hBN interface were investigated for all four devices, *i.e.*, BD, UCDI, UCDII, and CD, as shown in Figs. 4.7 and 4.8. This position was selected as these field distributions are accessible to experimental techniques. In order to gain additional insight, the cross-sectional field maps (which are not accessible experimentally) in the xz -and yz -plane are also shown in Figs. 4.7 and 4.8 respectively, directly below the corresponding planar data. Fig. 4.7 presents data after x -polarized excitation at three different frequencies, *i.e.*, below the hBN reststrahlen band at $\nu = 1200 \text{ cm}^{-1}$, within the hBN reststrahlen band

at $\nu = 1500 \text{ cm}^{-1}$ and above the reststrahlen band at $\nu = 1700 \text{ cm}^{-1}$. Fig. 4.8 presents data after y -polarized excitation at matching frequencies.

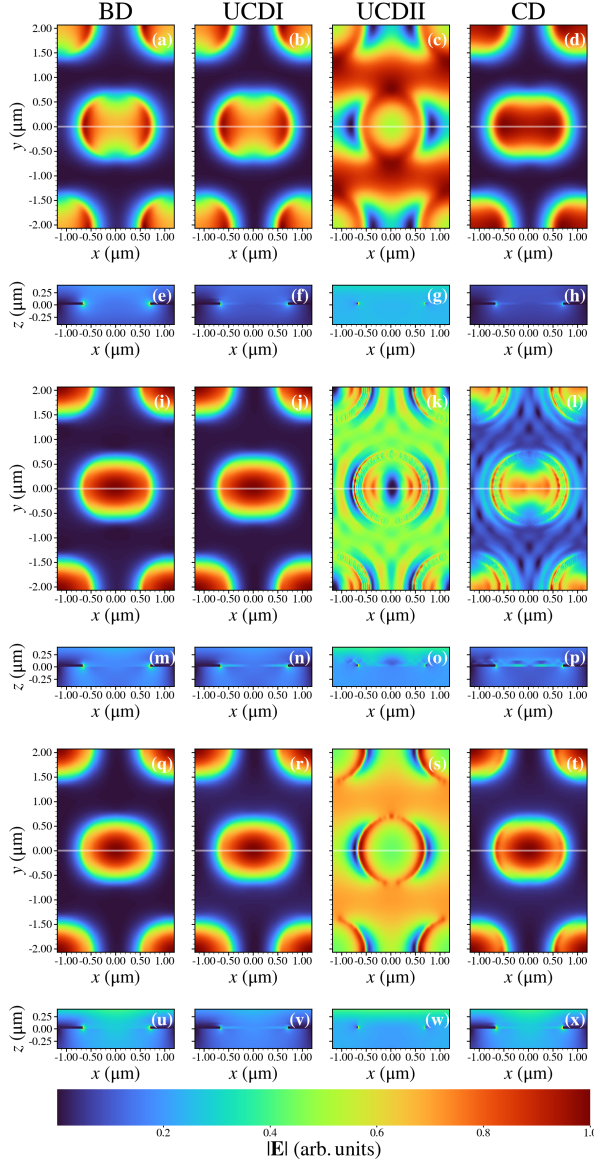


Figure 4.7: Background subtracted and normalized planar and cross-sectional colormaps of the $|E|$ field with for the BD, UCDI, UCDII, and CD with $d_{\text{CC}} = 2.38 \mu\text{m}$. Simulations in this figure used an x -polarized source. Panes (a) – (h) were excited below the reststrahlen band at $\nu = 1200 \text{ cm}^{-1}$. The white lines in the planar colormaps panes (a) – (d) indicate the location of the cross-sectional colormaps in (e) – (h). Panes (i) – (p) were excited in the reststrahlen band at $\nu = 1500 \text{ cm}^{-1}$. The white lines in the planar colormaps panes (i) – (l) indicate the location of the cross-sectional colormaps in (m) – (p). Panes (q) – (x) were excited above the reststrahlen band at $\nu = 1700 \text{ cm}^{-1}$. The white lines in the planar colormaps panes (q) – (t) indicate the location of the cross-sectional colormaps in (u) – (x).

The data excited at frequencies above and below the reststrahlen band is expected to be predominantly plasmonic in nature for BD, UCDI, UCDII, and CD; this is borne out by the data in Figs. 4.7 and 4.8 (a)–(h) and (q) – (x), respectively. In all cases the field concentration inside the circle is greater inside the circle than outside. For the UCDII the difference in contrast is lower than for the silver devices. Looking at the xz -plane data it was noticed that the field is at its highest magnitude along the vacuum boundary of the circles. The UCDII was again noted to have reduced contrast when compared to the metal devices. This indicated that both Ag and Si based devices will display phonon-polariton activity, but with greater absorptance in the Ag. Panes (k) and (l) display surface-phonon-polariton behaviour similar to that observed in Fig. 3.11. However, less contrast is observed in the cross sectional pane when compared to panes (o) and (p) in Fig. 3.11.

Observing Fig. 4.8 there is a noticeable reduction in contrast when compared to Fig. 4.7, indicating a polarization dependence of the absorptance features.

For potential comparison to experiment, it is useful to analyze lineouts from field data of the type presented in Fig. 4.7. A series of lineouts for a CD with $d_{CC} = 2.38 \mu\text{m}$ is shown in Fig. 4.9 (a). The electric fields were frequency resolved in the range $\nu = 1490 - 1570 \text{ cm}^{-1}$. The white line in Fig. 4.7 (a) indicates the point above the hBN-vacuum-Ag interface where the lineouts are taken. The lineout data in Fig. 4.9 is more complicated than that found in Fig. 3.12, and thus unsuitable for analysis by the naive peak finding algorithm used to extract the polariton wavelength from the data in Fig. 3.12.

The phonon-polariton dispersion is explored in Fig. 4.10. Fig. 4.10 (a) reproduces the far-field absorption spectrum from Fig. 4.5 (c) for convenient comparison with the near field data. Fig. 4.10 (b) shows E_z lineouts in the y -direction for frequencies in the range $\nu = 1000 - 1800 \text{ cm}^{-1}$ at intervals of 1 cm^{-1} . As can be seen from this figure, the region of highest field strength is in the vicinity of the inner Ag-vacuum boundary within the circular aperture (vacuum below the hBN layer), however features can be clearly resolved outside the circle (silver below the hBN layer). Broad features attributed to plasmons can be observed

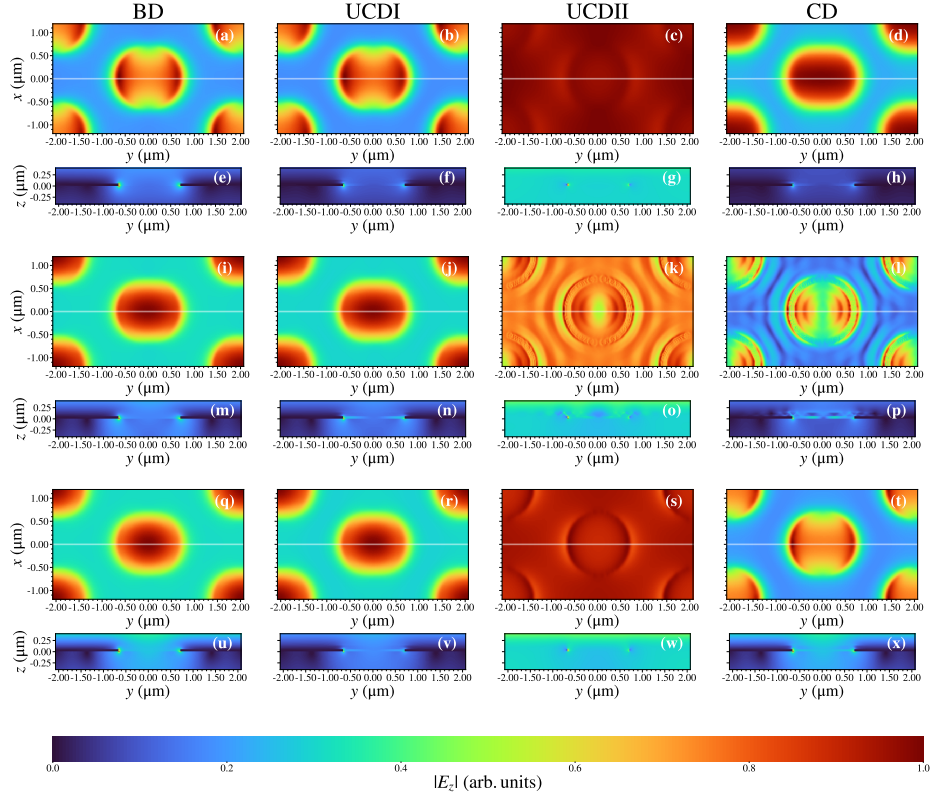


Figure 4.8: Background subtracted and normalized planar and cross-sectional colormaps of the $|E|$ field with for the BD, UCDI, UCDII, and CD with $d_{CC} = 2.38 \mu\text{m}$. Simulations in this figure used an x -polarized source. Panes (a) – (h) were excited below the reststrahlen band at $\nu = 1200 \text{ cm}^{-1}$. The white lines in the planar colormaps panes (a) – (d) indicate the location of the cross-sectional colormaps in (e) – (h). Panes (i) – (p) were excited in the reststrahlen band at $\nu = 1500 \text{ cm}^{-1}$. The white lines in the planar colormaps panes (i) – (l) indicate the location of the cross-sectional colormaps in (m) – (p). Panes (q) – (x) were excited above the reststrahlen band at $\nu = 1700 \text{ cm}^{-1}$. The white lines in the planar colormaps panes (q) – (t) indicate the location of the cross-sectional colormaps in (u) – (x).

both below and above the reststrahlen band; these features extend from inside the vacuum region into the silver region. Within the frequency range spanned by the reststrahlen band, multiple branches can be observed in both the vacuum and Ag regions.

Fig. 4.10 (c) shows the spatial Fourier transform of the (full spatial lineout) data described above. The resulting plot of $|E_z(q, \omega)|$ enables the phonon-polariton dispersion curves to be visualized. In order to aid the interpretation of the data in Fig. 4.10 (c), hBN phonon-

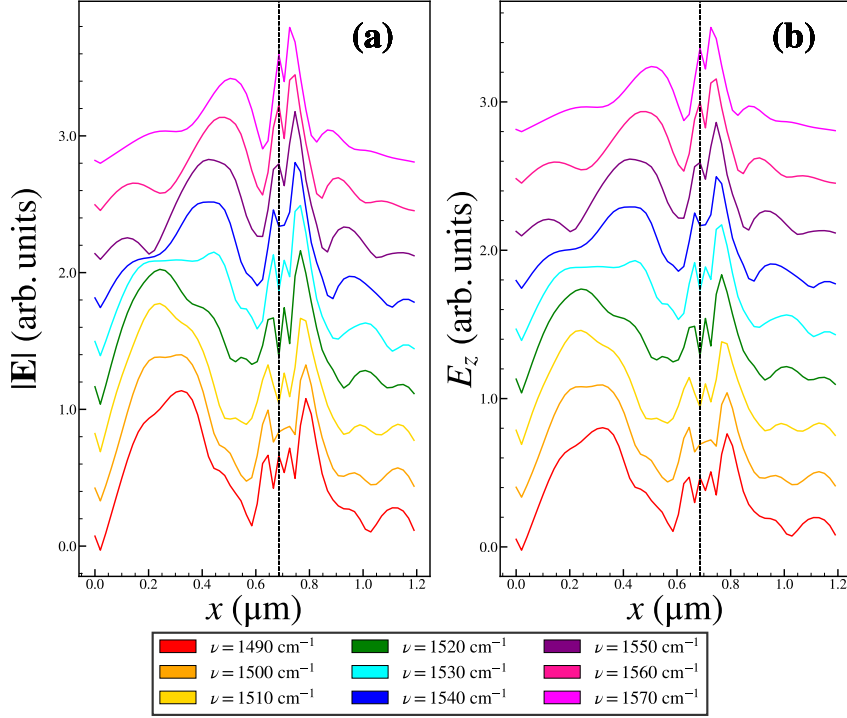


Figure 4.9: (a) CD with $d_{\text{CC}} = 2.38 \mu\text{m}$ lineouts of the magnitude of the electric field for a range of excitation frequencies in the reststrahlen band $\nu = 1490 - 1570 \text{ cm}^{-1}$. (c) CD with $d_{\text{CC}} = 2.38 \mu\text{m}$ lineouts of the z -component of the electric field for a range of excitation frequencies in the reststrahlen band $\nu = 1490 - 1570 \text{ cm}^{-1}$.

polariton dispersion curves are calculated as described in Chapter 3. The curves in green are for the Vacuum/hBN/Vacuum/Si structure, while the curves in red are for the Vacuum/hBN/Ag/Si structure.

As can be seen in Fig. 4.10 (c), the upper green curve (dispersion curve for the Vacuum/hBN/Vacuum/Si structure with $n = 0$) and the upper red curve (dispersion curve for the Vacuum/hBN/Ag/Si structure with $n = 1$) overlap regions with large values of $|E_z(q, \omega)|$. As in Chapter 3, the value of $|E_z(q, \omega)|$ decreases strongly with increasing values of n .

The spectral content of the data in Fig. 4.10 (c) is obtained by integrating over q to yield the quantity denoted $\Sigma_z(\omega)$, which is plotted in Fig. 4.10 (d). The resulting spectrum, while exhibiting the general features of the far-field spectrum, shows two notable differences.

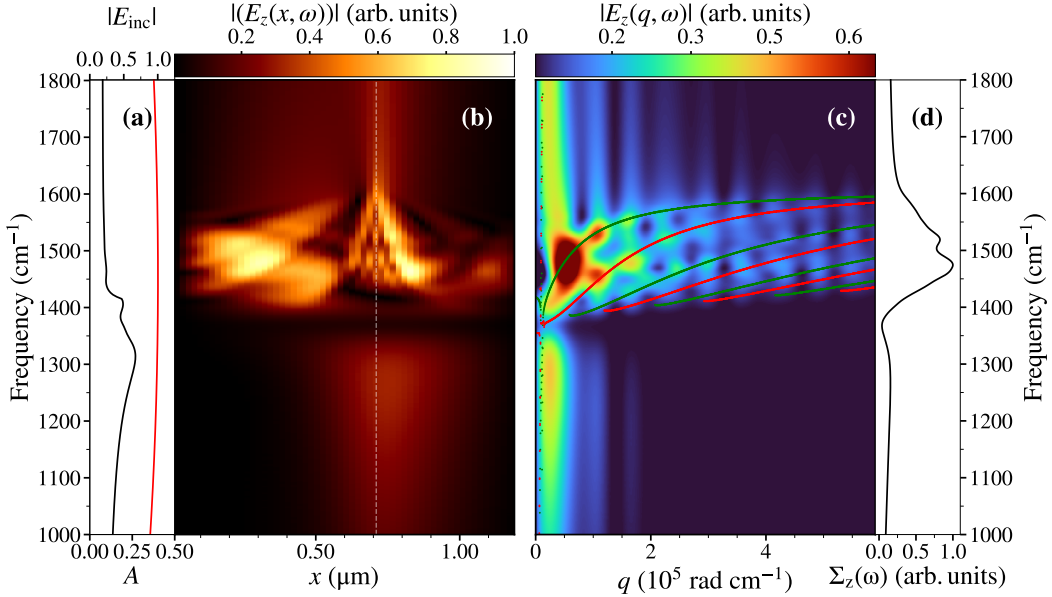


Figure 4.10: Phonon-polariton dispersion curves in the CD with $d_{CC} = 2.38 \mu\text{m}$. (a) The far-field absorption spectrum. (b) E_z lineouts along the $y = 0 \mu\text{m}$ line for frequencies in the range $\nu = 1000 - 1800 \text{ cm}^{-1}$ with a spectral resolution of 1 cm^{-1} . The spatial extent of the data displayed in this pane is from the center to the edge of the unit cell to avoid duplication. The white dotted line in this pane indicates the boundary between vacuum and Ag. (c) The spatial Fourier transform of the (full spatial lineout) data presented in pane (b). This data has been interpolated using a cubic spline algorithm. The resulting plot of $|E_z(q, \omega)|$ enables the phonon-polariton dispersion curves to be visualized. The red and green theoretical dispersion curves are calculated as described in the text. (d) The spectral content of the data in pane (c) obtained by integrating over q .

Firstly, this spectrum suppresses both the residual peak at the hBN TO optical phonon frequency and the low frequency plasmon band centered at $\sim 1300 \text{ cm}^{-1}$ relative to the phonon-polariton signal. Secondly, the fine structure within the hBN reststrahlen band is emphasized. As in Chapter 3, the near-field spectrum, $\Sigma_z(\omega)$, emphasizes the slab phonon-polaritons over the bulk phonon-polaritons when compared to the far-field spectrum thus highlighting the importance of using near-field experimental techniques to investigate systems of this kind.

To further investigate the coupling to the hBN phonon-polaritons, the phonon-polariton signal strength in the coupled device was investigated as a function of d_{CC} . In order to

better separate the signal originating from the Vacuum/hBN/Vacuum/Si and the Vacuum/hBN/Ag/Si regions of the device, a Tukey [93] windowing function was used to mask regions of the real space data in Fig. 4.10 (b) before Fourier transforming that data. The Fourier transformed data that derives from only the Vacuum/hBN/Vacuum/Si region of the $d_{CC} = 2.38 \mu\text{m}$ device is shown Fig. 4.11 (a). The theoretical dispersion curves for the Vacuum/hBN/Vacuum/Si structure are overlaid in green. The upper green curve is denoted $\omega_{V,0}(q)$. Similarly, the Fourier transformed data that derives from only the Vacuum/hBN/Ag/Si region of the same device is shown Fig. 4.11 (b) and the theoretical dispersion curves for the Vacuum/hBN/Ag/Si structure are overlaid in red. The upper red curve is denoted $\omega_{Ag,1}(q)$. Figs. 4.11 (c) and (d) are the same as Figs. 4.11 (a) and (b), respectively, but for the $d_{CC} = 2.74 \mu\text{m}$ device.

A region of Fig. 4.11 (a) was defined by q in the range $0.15 \times 10^5 - 4.15 \times 10^5 \text{ rad cm}^{-1}$ and ω in the range $\omega_{V,0}(q) \pm 88 \text{ cm}^{-1}$. $|E_z(q, \omega)|$ was integrated over this region to yield the quantity Σ_V . Similarly, a region of Fig. 4.11 (b) was defined by q in the range $0.8 \times 10^5 - 4.8 \times 10^5 \text{ rad cm}^{-1}$ and ω in the range $\omega_{Ag,1}(q) \pm 88 \text{ cm}^{-1}$. $|E_z(q, \omega)|$ was integrated over this region to yield the quantity Σ_{Ag} . This process was repeated for devices with values of d_{CC} in the range $2.14 - 2.78 \mu\text{m}$. $\Sigma_V(d_{CC})$ was normalized to its maximum value which occurred at $d_{CC} = 2.22 \mu\text{m}$ and is plotted in green in Fig. 4.11 (e). $\Sigma_{Ag}(d_{CC})$, which is plotted in red in Fig. 4.11 (e), was also normalized to the maximum value of $\Sigma_V(d_{CC})$, so that the relative strengths of these two quantities could be directly compared. $\Sigma_{Ag}(d_{CC})$ is approximately half the strength of $\Sigma_V(d_{CC})$, but exhibits a similar dependence on d_{CC} .

For comparison, the far-field coupled device (CD) absorptance spectra of Fig. 4.5 (c) were integrated over the reststrahlen band to yield the quantity Σ_{Abs} , which was normalized to its maximum value, which occurred at $d_{CC} = 2.14 \text{ nm}$. Σ_{Abs} is plotted in blue in Fig. 4.11 (f). A comparison of Fig. 4.11 (e) and (f) suggests that the variation of $\Sigma_V(d_{CC})$ and $\Sigma_{Ag}(d_{CC})$ with d_{CC} is (as was observed in Chapter 3) dominated by the overlap of the respective absorptance spectrum with the reststrahlen band.

A careful examination of Fig. 4.11 (a), (b), (c) and (d) reveals that, unlike the devices in Chapter 3, the phonon-polaritons excited in devices with different values of d_{CC} , *i.e.*, $d_{CC} = 2.38\text{ nm}$ and $d_{CC} = 2.74\text{ nm}$ occur at approximately the same frequencies. This behavior is consistent with the data in Fig. 4.11 (g), which shows both a plot of the frequency at which the maximum Vacuum/hBN/Vacuum/Si phonon-polariton signal occurs (plotted in green) and a plot of the frequency at which the maximum Vacuum/hBN/Ag/Si phonon-polariton signal occurs (plotted in red) as a function of d_{CC} . An examination of this plot shows that the frequency at which the Vacuum/hBN/Ag/Si phonon-polariton maximum occurs is essentially independent of d_{CC} , while the frequency at which the Vacuum/hBN/Vacuum/Si phonon-polariton maximum occurs (with the exception of the $d_{CC} = 2.74\text{ nm}$ device) decreases monotonically with d_{CC} . For comparison, the data (plotted in blue) in Fig. 4.11 (h) shows the peak of the high frequency far-field absorptance band from Fig. 4.5. The variation of ω_{Abs} with d_{CC} is less pronounced than that observed in Chapter 3 and furthermore becomes essentially independent of d_{CC} for devices with $d_{CC} > 2.46\text{ nm}$.

The difference in behavior between the devices in this chapter and those in Chapter 3 is assumed to be due to the Rayleigh anomalies modifying the spectral properties. The above data and associated discussion indicates that the tunability of the frequency/wavevector of the phonon-polariton has been compromised by the Rayleigh anomalies in these devices.

4.5 Conclusions

The excitations that occur in a hBN/ hexagonally nanopatterned Ag device on an Si substrate have been investigated using the Finite-Difference Time-Doman (FDTD) method. Similar to the devices investigated in Chapter 3, both the far- and near-field properties of these devices were studied. Because of the high refractive index of the Si substrate, this device exhibited Rayleigh anomalies that were close to, and in some cases, in resonance with the plasmon-polariton absorption peaks and thus dramatically modified the shape of those peaks. As a

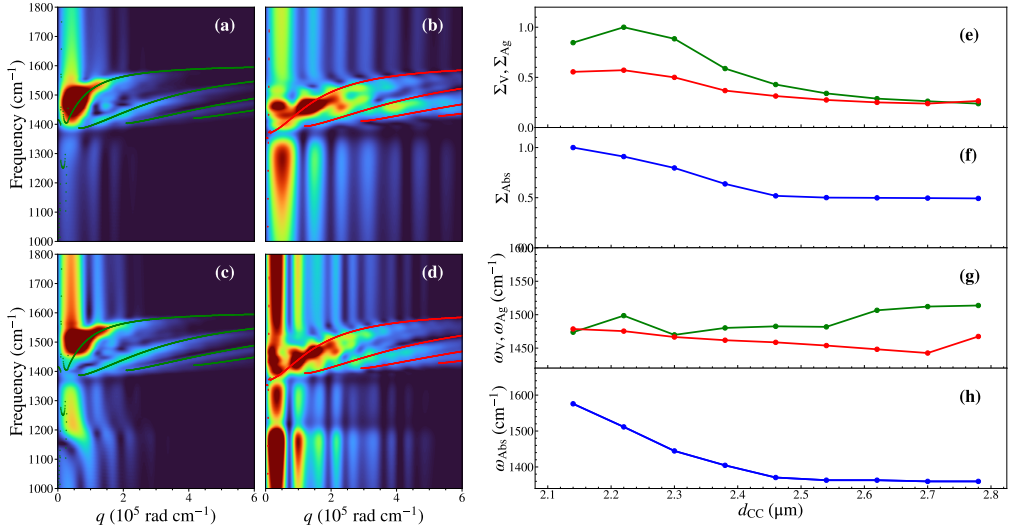


Figure 4.11: Vacuum/hBN/Vacuum/Si and Vacuum/hBN/Ag/Si phonon-polariton signal strength and frequency dependence in the CDs as a function of d_{CC} . (a) The spatial Fourier transform of the Vacuum/hBN/Vacuum/Si masked data from pane Fig. 4.10 (b). The green theoretical dispersion curves are for the Vacuum/hBN/Vacuum/Si system. (c) The spatial Fourier transform of the Vacuum/hBN/Ag/Si masked data from pane Fig. 4.10 (b). The red theoretical dispersion curves are for the Vacuum/hBN/Ag/Si system. Pane (c) and (d) are the same as pane (a) and (b), but for the $d_{CC} = 2.74 \mu\text{m}$ device. (e) Green: The integrated Vacuum/hBN/Vacuum/Si phonon-polariton signal strength plotted as a function of d_{CC} . Red: The integrated Vacuum/hBN/Ag/Si phonon-polariton signal strength plotted as a function of d_{CC} . (f) Blue: The far-field absorptance spectra from Fig. 4.5 integrated over the spectral region of the reststrahlen band plotted as a function of d_{CC} . (g) Green: The frequency at which the peak of the Vacuum/hBN/Vacuum/Si phonon-polariton signal strength occurs plotted as a function of d_{CC} . Red: The frequency at which the peak of the Vacuum/hBN/Ag/Si phonon-polariton signal strength occurs plotted as a function of d_{CC} . (h) Blue: The peak of the high frequency far-field absorptance band from Fig. 4.5. The lines in panes (e), (f), (g) and (h) are guides to the eye.

consequence, the far-field properties were rendered less useful for this class of devices, than for the devices described in Chapter 3.

Nevertheless, an investigation of the near-field electric field distributions enables the slab phonon-polaritons to be identified and categorized according to mode number per Eq. 3.1 and supporting layer, *i.e.*, vacuum or Ag. As in Chapter 3, a comparison of the field maps

for the CD and UCDII show that the presence of the plasmon-polaritons in the CD increases the contrast in the spatial electric field variation indicating that the plasmon plays a key role in both coupling energy into the hBN phonon-polaritons. By examining the dependence of the phonon-polariton excitation on the device periodicity, d_{CC} , it was observed that the frequency/wavevector of the phonon-polariton could not be very effectively tuned by varying d_{CC} . However, the strength of the phonon-polariton signal does vary with d_{CC} and that variation is dominated by the spectral overlap of the far-field absorptance spectrum with the reststrahlen band. The reduction in signal strength in the region of the reststrahlen band caused by the Rayleigh anomalies may be responsible for both the lower contrast observed in this class of devices and the reduced tunability of the phonon-polariton excitation.

Chapter 5

Coupling of phonon-polaritons with plasmon-polaritons in a layered device comprising hBN on a nanopatterned square array of Au crosses suspended over a ground plane

5.1 Introduction

The device studied in this chapter is an infinite hBN sheet over a square array of cross shaped Au structures. The crosses were supported by an infinite sheet of dielectric material, which in turn was supported by an infinite grounding sheet of Au. The cross shape offers similar benefits to those described in Chapter 3. The presence of a grounding plane separated by a dielectric has been shown to exhibit perfect infrared absorption [59, 60] as well as promoting strong plasmon-phonon coupling in an IR resonant material between the grating and the source [50]. Using the tuning method studied in Chapter 3, the period, d_{CC} was varied to

tune the “perfect” absorptance peak to the TO resonance of hBN. The resulting interaction between plasmon-polaritons and phonon-polaritons was studied and is detailed below.

Specific details on how these devices were modelled within FDTD simulations is given in the following section.

5.2 Preliminary Measurements

The details of the nanopatterned structure simulated in this chapter are shown in Fig. 5.1. The structure comprised of an 80 nm sheet of hexagonal boron nitride (hBN) deposited on an array of 0.1 μm thick cross shaped Au nanostructures atop of a 0.196 μm dielectric layer with $\varepsilon_{\text{SiO}_2} = 2.28$. The relative permittivity, $\varepsilon_{\text{SiO}_2} = 2.28$, is taken from the study published by Liu *et.al.*, [59] who’s research into “perfect” plasmonic absorbers provided much of the initial insight that went into this chapter. The SiO_2 sheet was atop an infinite sheet of a 0.1 μm thick Au film atop a Si substrate. The Au nanostructures were arranged in a square lattice with a distance between the centers of d_{CC} , which was varied during this work. The nanostructure dimensions were $l = 0.8 d_{\text{CC}}$ and $w = 0.16 d_{\text{CC}}$, where d_{CC} was the model periodicity in the congruent x - and y - dimensions, which was varied during this work.

As described in Chapter 3, broadband, plane wave sources were used to excite structures investigated in this chapter. The sources were x -polarized and propagated in the negative z -direction. Reflection and transmission spectra were calculated using DFT sensors as described in Section 2.5.2. The reflection and transmission sensors were placed at $z = 0.01 \mu\text{m}$ and $z = 1.78 \mu\text{m}$ respectively. To prevent divergence in the simulation caused by edge reflections in the patterned metallic layer, a 50 layer convolutional perfectly matched layer (CPML) boundary was used in the z -dimension. Periodic boundaries were used in the x - and y - dimensions.

As discussed in detail in Section 2.2 and Section 4.2 the various components of the device were modelled as follows. The hBN layer was simulated using a tensor Lorentz model, the Au

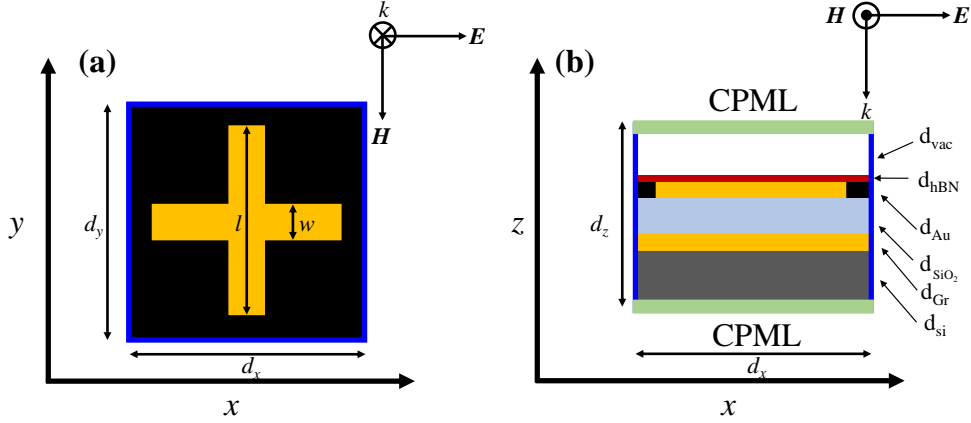


Figure 5.1: Schematic of the hBN/Au structure simulated in this chapter. (a) Planar view at the hBN/Au interface. (b) Cross-sectional view. CPML: Convolutional perfectly matched layer boundary conditions are imposed at the z - direction boundaries. Periodic boundary conditions are imposed at the x and y boundaries. The unit cell lengths in the x - and y -directions are d_x and d_y , respectively. The layer thicknesses are $d_{\text{vac}} = 0.62 \mu\text{m}$, $d_{\text{hBN}} = 80 \text{ nm}$, $d_{\text{Au}} = 0.1 \mu\text{m}$, $d_{\text{SiO}_2} = 0.196 \mu\text{m}$, $d_{\text{Gr}} = 0.1 \mu\text{m}$, $d_{\text{si}} = 0.604 \mu\text{m}$. The length of the long segments of the cross pattern is $l = 0.8 d_x = 0.8 d_y$ while the width of the cross is $w = 0.16 d_x = 0.16 d_y$. The distance between the centers of neighboring crosses is $d_{\text{CC}} = d_x = d_y$. The directions of the \mathbf{E} -field, \mathbf{H} -Field and propagation vector \mathbf{k} are shown in both panes.

film was simulated using a Debye-Drude model to fit to the wavelength dependent refractive index data as detailed by Ciesielski *et al.* [74]. Finally, the dielectric and Si substrate were both simulated using a simple dielectric with $\epsilon_{\text{SiO}_2} = 2.28$ and $\epsilon_{\text{Si}} = 11.7$, respectively.

The simulational meta-parameters and the materials parameters used to simulate the devices described in this chapter are given in table 5.1.

As in Chapter 3 and 4, in addition to the structure, denoted the “coupled device” (CD), depicted in Fig. 5.1, several other auxiliary structures were simulated. The “bare device” (BD), this device is identical to the coupled device, but with the hBN layer removed. This device does not support phonon-polaritons. The “uncoupled device I” (UDCI), this device

Table 5.1: Simulational Parameters

Symbol	Value	Units	Description
Simulational Meta-Parameters			
Δx	20	nm	Spatial step in x -direction
Δy	20	nm	Spatial step in y -direction
Δz	2	nm	Spatial step in z -direction
Δt	5.945×10^{-18}	s	Time step
n_x	$d_{CC}/\Delta x$	N.A.	Number of steps in x -direction
n_y	$d_{CC}/\Delta y$	N.A.	Number of steps in y -direction
n_t	(10^6 , 500×10^3)	N.A.	Number of time steps (near-field, far-field)
n_{PML}	50	N.A.	Number of PML layers in $\pm z$ -direction
Materials Parameters – Au			
ε_∞	3.321	N.A.	High-frequency ε
ε_s	-1.598×10^{-4}	N.A.	Low-frequency ε
τ_0	1.425×10^{-14}	s	Relaxation time
σ	1.006×10^6	Sm^{-1}	Conductivity
Materials Parameters – hBN			
$\varepsilon_{x,y}(\infty)$	4.87	N.A.	High-frequency ε in the x, y -directions
$\varepsilon_z(\infty)$	2.96	N.A.	High-frequency ε in the z -direction
$S_{x,y}$	1.83	N.A.	Dimensionless coupling factor in the x, y -directions
S_z	0.61	N.A.	Dimensionless coupling factor in the z -direction
$\hbar\omega_{x,y}$	170.1	meV	TO phonon frequency in the x, y -directions
$\hbar\omega_z$	92.5	meV	TO phonon frequency in the z -direction
$\gamma_{x,y}$	3.97	meV	Damping constant in the x, y -directions
γ_z	0.25	meV	Damping constant in the z -direction
Materials Parameters – Substrate, Spacer-layers etc.			
$\varepsilon_{\text{SiO}_2}$	2.28	N.A.	Relative permitivity of SiO_2
ε_{Si}	11.73	N.A.	Relative permitivity of Si

is identical to the coupled device, but with the hBN layer replaced with an equal thickness anisotropic layer that has $\varepsilon_k(\infty)$ equal to the values for hBN, but the resonant behavior removed by setting $S_k = 0$. This device does not support phonon-polaritons.

In order to investigate the effect of tuning the plasmon resonance through the hBN reststrahlen band, a series of FDTD simulations were performed at a range of distances between the nearest neighbor centers of the crosses, (*i.e.*, d_{CC} in the range $1.82 - 3.10 \mu\text{m}$). The resulting $R(\omega)$, $T(\omega)$, and $A(\omega)$ spectra are shown in Fig. 5.2. Similarly to the spectra in Fig. 3.4 a clear red shift of the main spectral features is observed as d_{CC} was increased. In contrast to Fig. 3.4 the observed transmittance was zero for all values of d_{CC} . Furthermore for devices with d_{CC} in the range $2.46 - 2.94$ unity absorptance is observed, with the frequency of the unity absorption red shifting as d_{CC} was increased. Unlike in Figs. 3.4 and 4.2, no Rayleigh anomalies were observed, even though, according to Eq. 4.1, they are expected for the devices with $d_{CC} \geq 2.94 \mu\text{m}$

The spectra for the UCDI are shown in Fig. 5.3. As with the uncoupled device studied in Fig. 3.5 and Fig. 4.3 of Chapter 3 and 4 the addition of a “dielectric” hBN layer resulted in a red shift of features. Unlike Figs. 3.5 and 4.3 all of the features shift. This gives evidence that all of the features observed in Figs. 5.2 and 5.3 are plasmonic in nature. The structure with $d_{CC} = 2.70 \mu\text{m}$ was observed to be resonant with the hBN TO phonon frequency.

The equivalent CD data to those shown above can be seen in Fig. 5.4. As was seen in the two previous chapters, the most prominent effect observed in the CD is that the plasmon resonances split into two main peaks to either side of the hBN TO phonon frequency when compared to equivalent d_{CC} UCDI. The peaks for $d_{CC} = 2.70 \mu\text{m}$ device shifted approximately equal amounts above and below the hBN TO phonon frequency. Another notable feature is the sharp absorptance peak just below the TO phonon frequency at $\nu = 1350 \text{ cm}^{-1}$. Similar to Fig. 3.6 (c) are a series of small peaks that lie between the hBN TO and LO frequencies. However, these features are much more pronounced in Fig. 5.4, than in Figs. 3.5 and 4.3.

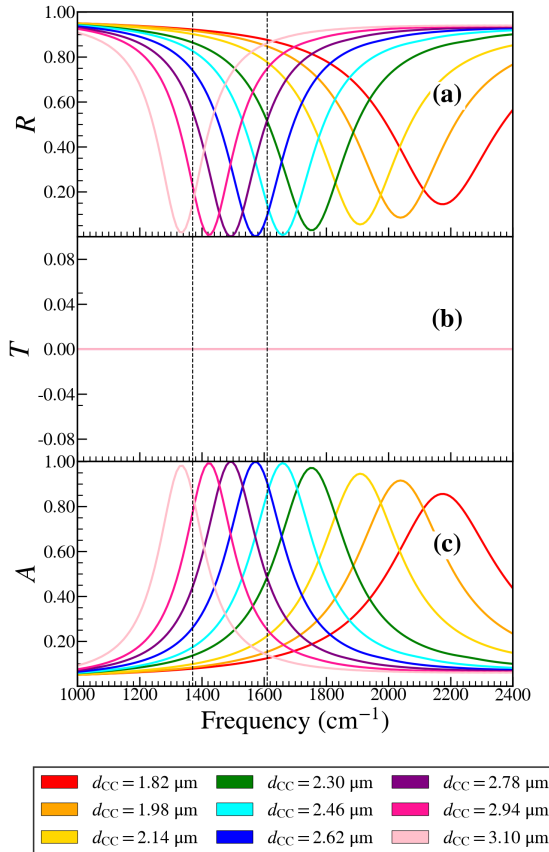


Figure 5.2: The spectra for the BD at a range of d_{CC} values. (a) Reflectance spectra. (b) Transmittance spectra. (c) Absorptance spectra. The vertical black dashed lines in this figure indicate the position of the hBN TO and LO phonon frequencies.

5.3 Far-Field Analysis

In order to investigate the effect of tuning the plasmon resonance through the hBN reststrahlen band, a series of FDTD simulations were performed at a range of distances between the nearest neighbor centers of the crosses, (*i.e.*, d_{CC} in the range 1.82 – 3.10 μm) and the absorptance spectra for the bare device (BD), the uncoupled device I (UCDI) and the coupled device (CD) structures were calculated from the frequency resolved Poynting vector data collected by the planar DFT sensors described in section 2.5.2. Fig. 5.5 shows the absorption spectra calculated for all three devices. The vertical dashed lines in Fig. 5.5 indi-

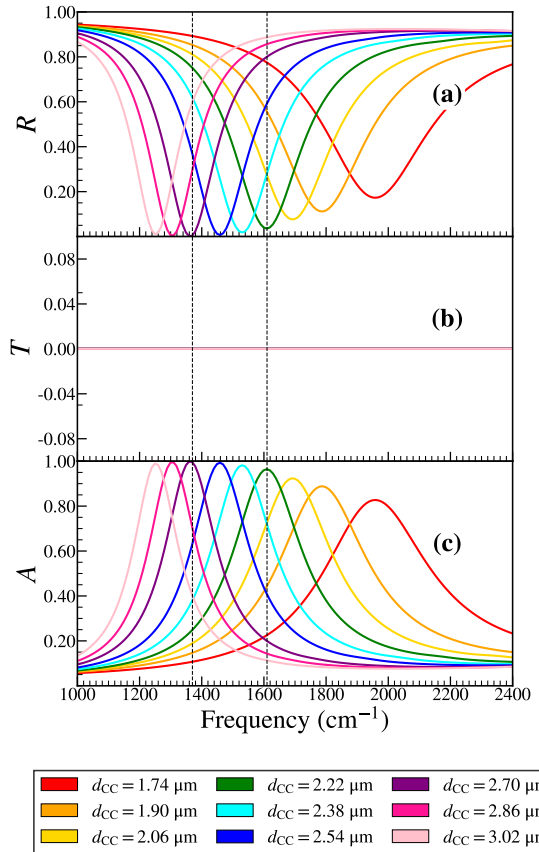


Figure 5.3: The spectra for the UCDI at a range of d_{CC} values. (a) Reflectance spectra. (b) Transmittance spectra. (c) Absorptance spectra. The vertical black dashed lines in this figure indicate the position of the hBN TO and LO phonon.

cate the positions of the hBN TO and LO phonons at 1360 and 1614 cm^{-1} , respectively. As can be seen from Fig. 5.5 (b), the UCDI structure with $d_{CC} = 2.70\text{ }\mu\text{m}$ exhibits a plasmon absorptance peak that is most closely resonant with the hBN TO phonon and this device is the one studied most extensively in this chapter.

Fig. 5.5 (c) shows the absorption spectra for a series of CDs for a range of d_{CC} . The most prominent effect observed in the CD is that the plasmon resonances split into two main peaks to either side of the hBN TO phonon frequency as described in Section 3.2.

In order to better analyze the absorptance peak frequency shifts observed in Fig. 5.5, the data in Fig. 5.5 (b) and (c) were plotted in colormap form as a function of $\frac{2\pi}{d_{CC}}$. As

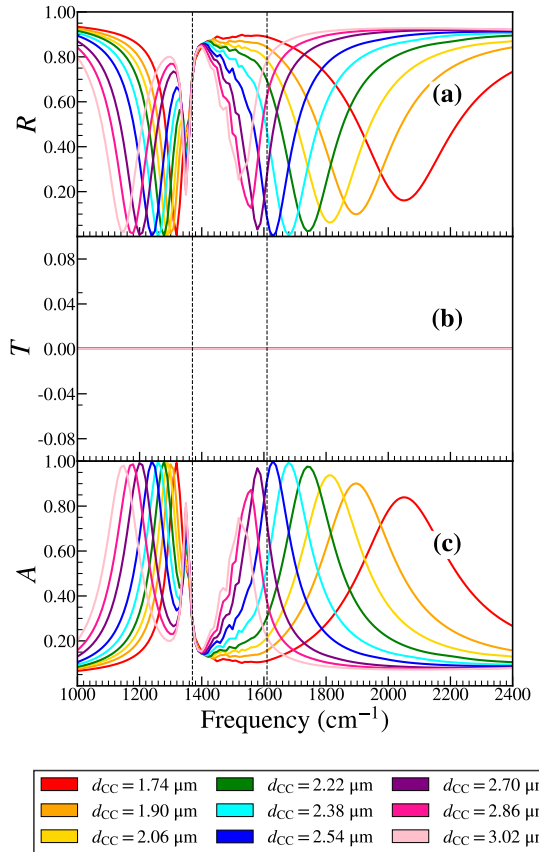


Figure 5.4: The spectra for the CD at a range of d_{CC} values. (a) Reflectance spectra. (b) Transmittance spectra. (c) Absorptance spectra. The vertical black dashed lines in this figure indicate the position of the hBN TO and LO phonon frequencies.

described in Chapter 3 and 4, these plots can act as a proxy for the dispersion curves, although with some limitations. When compared to the resonances observed in the UCDI, the plasmon-polariton in UCD splits due to the interaction of the bulk phonon-polariton in the hBN. This was further supported by the similar splitting in the plasmon-polariton peak that was observed in Chapters 3 and 4, and in the reflection data presented by Wan *et al.* [50] in their Fig. 3 (a). What is clearly apparent is a strong absorptance feature at $\nu = 1350 \text{ cm}^{-1}$. This is likely due to an hBN bulk phonon TO mode as noted in Chapter 3. The fine structure between the hBN TO phonon and LO phonon frequencies is likely due to

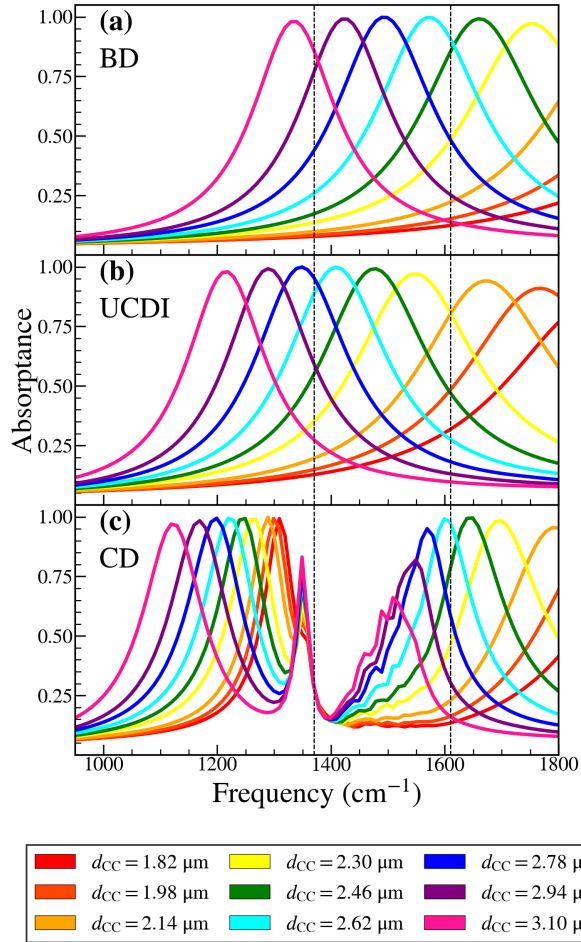


Figure 5.5: (a) The absorptance spectrum of the BD for a range of d_{CC} values. (b) The absorptance spectra of the UCDI. (c) The absorptance spectra of the CD. The vertical black dashed lines in this figure indicate the position of the hBN TO and LO phonon frequencies as described in the main text.

slab phonon-polariton modes in the hBN layer; this interpretation will be further supported by the near field data below.

5.4 Near-Field Analysis

In order to gain additional insight into the coupling between the plasmon-polaritons in the nanopatterned Au and the phonon-polaritons in the hBN film, the electric field distributions,

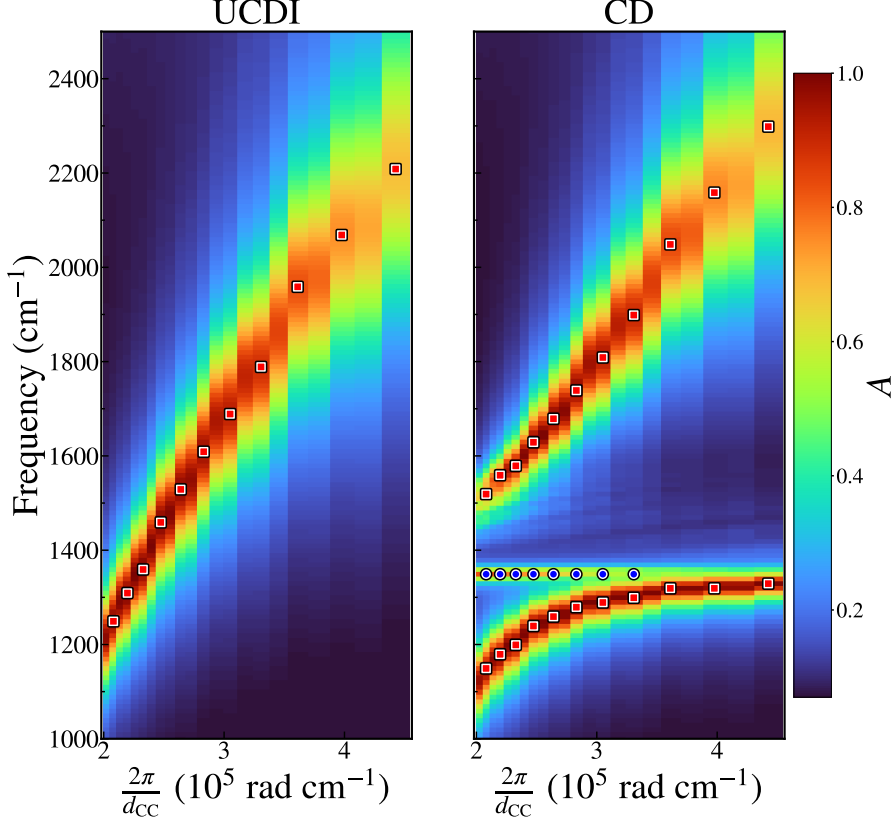


Figure 5.6: (a) Absorptance spectra for the UCDI as a function of $\frac{2\pi}{d_{CC}}$ plotted as a color map. The symbols indicate the peaks in the absorptance spectra. The square symbols indicate the plasmon-polariton, which shifts inversely to increases in d_{CC} . (b) Absorptance spectra for the CD as a function of $\frac{2\pi}{d_{CC}}$ plotted as a color map. The symbols indicate the peaks/shoulders in the absorptance spectra. The square symbols highlight the interaction between plasmon-polariton in the nanopatterned Au film and the bulk phonon-polariton in the hBN.

$|\mathbf{E}|$, at the position of the vacuum/hBN interface were investigated for all four devices, *i.e.*, BD, UCDI, UCDII, and CD, as shown in Fig. 5.7. This position was selected as these field distributions are accessible to experimental techniques. In order to gain additional insight, the cross-sectional field maps (which are not accessible experimentally) in the yz -plane are also shown in Fig. 5.7 directly below the corresponding planar data. Fig. 5.7 presents data after x -polarized excitation at three different frequencies, *i.e.*, below the hBN reststrahlen

band at $\nu = 1200 \text{ cm}^{-1}$, within the hBN reststrahlen band at $\nu = 1500 \text{ cm}^{-1}$ and above the reststrahlen band at $\nu = 1700 \text{ cm}^{-1}$.

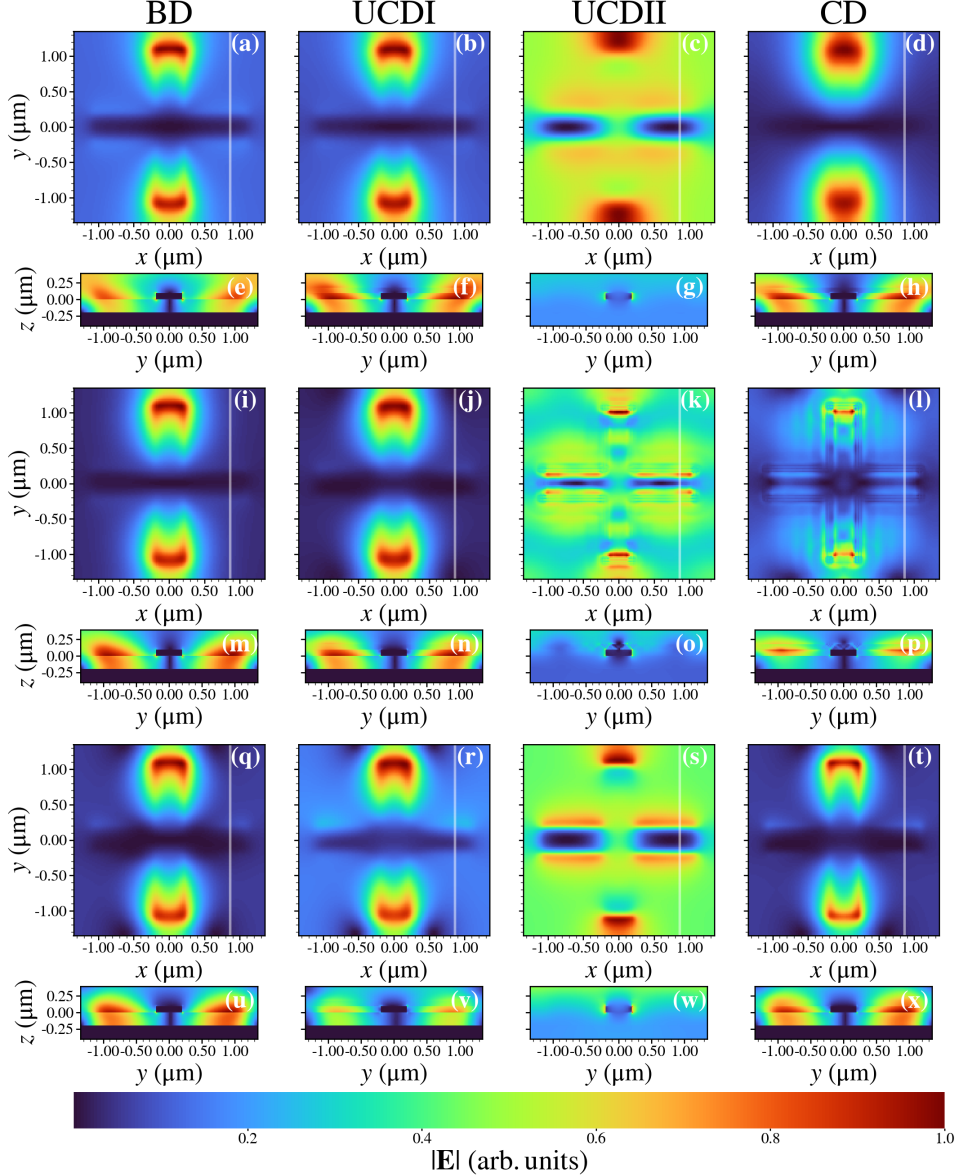


Figure 5.7: Background subtracted and normalized planar and cross-sectional colormaps of the field magnitude for the BD, UCDI, UCDII, and CD with $d_{\text{CC}} = 2.70 \mu\text{m}$. Panes (a) – (h) were excited below the reststrahlen band at $\nu = 1200 \text{ cm}^{-1}$. The white lines in the planar colormaps panes (a) – (d) indicate the location of the cross-sectional colormaps in (e) – (h). Panes (i) – (p) were excited in the reststrahlen band at $\nu = 1500 \text{ cm}^{-1}$. The white lines in the planar colormaps panes (i) – (l) indicate the location of the cross-sectional colormaps in (m) – (p). Panes (q) – (x) were excited above the reststrahlen band at $\nu = 1700 \text{ cm}^{-1}$. The white lines in the planar colormaps panes (q) – (t) indicate the location of the cross-sectional colormaps in (u) – (x).

As in Chapters 3 and 4, the data excited at frequencies above and below the reststrahlen band is expected to be predominantly plasmonic in nature for BD, UCDI and CD; this is borne out by the data in Fig. 5.7 (a)–(h) and (q) – (x), respectively. In particular, in the case of the BD, there are field hot-spots at the outer corners of the cross pattern. In both the UCDI and CD, these hot spots are reproduced and smeared out; in the case of the CD this is due the presence of the hBN capping layer. The UCDII exhibits substantially different evidence of field hot-spot behavior as expected for a structure without a nanostructured metallic layer. In the UCDII the hot spots are along the edges of the Si cross which are perpendicular to the source and at much less contrast than the metallic structures. As in Chapters 3 and 4, the only rapid variations in the field take place right at the boundary between the metal/dielectric cross and the enclosed vacuum. Based upon the above discussion, the field maps shown in panes (b) and (r) of Fig. 5.7 are taken to be a prototypical signature of plasmonic behavior in the capped devices considered in this dissertation. In the case of the CD, see Fig. 5.7 (d) and (t), the field maps are very similar to those depicted in Fig. 5.7 (b) and (r), indicating that the behavior observed is predominately plasmonic when this device is excited either above or below the hBN reststrahlen band.

For potential comparison to experiment, it is useful to analyze lineouts from field data of the type presented in Fig. 5.7. A series of lineouts for a CD with $d_{CC} = 2.70 \mu\text{m}$ is shown in Fig. 5.8 (a). The electric fields were frequency resolved in the range $\nu = 1440 - 1510 \text{ cm}^{-1}$. The position of the lineout is indicated by the white line in the insert of Fig. 5.8 (b). Lineout data was only extracted outside of the cross region, *i.e.*, where the hBN was supported by a vacuum layer. The peaks in $|\mathbf{E}|$ were determined using the peak fitting algorithm described above. A phonon-polariton wavelength was assigned by calculating the averages of the differences between successive peaks. These wavelengths were found to lie in the range 160 – 300 nm. These data were used to construct a dispersion curve as shown in Fig. 5.8 (b).

Further insight can be obtained by examining the individual field components [90], thus a similar process was applied to the E_z lineout data as shown in Fig. 5.8 (c) and (d). As can

be seen by comparing the plots in Fig. 5.8 (b) and (d), the computed dispersion curves are similar although not identical, particularly at low values of q .

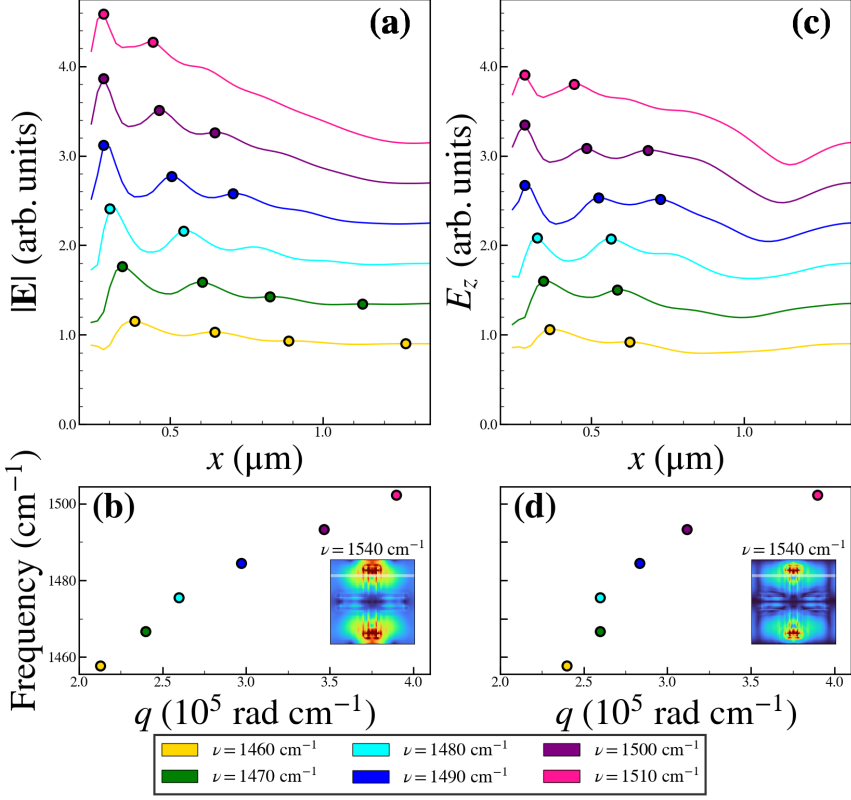


Figure 5.8: (a) CD with $d_{\text{CC}} = 2.70 \mu\text{m}$ lineouts of the magnitude of the electric field for a range of excitation frequencies in the reststrahlen band $\nu = 1440 - 1510 \text{ cm}^{-1}$. (b) CD with $d_{\text{CC}} = 2.70 \mu\text{m}$ lineouts of the z -component of the electric field for a range of excitation frequencies in the reststrahlen band $\nu = 1440 - 1510 \text{ cm}^{-1}$. The circular dots indicate peaks in the lineout. (d) Dispersion curve constructed from the peak data in pane (c). The inserts in panes (b) and (d) show the position of the lineouts in panes (a) and (c).

The phonon-polariton dispersion is explored further in Fig. 5.9. Fig. 5.9 (a) reproduces the far-field absorption spectrum from Fig. 5.5 (c) for convenient comparison with the near field data. Fig. 5.9 (b) shows E_z lineouts in the x -direction for frequencies in the range $\nu = 1000 - 1800 \text{ cm}^{-1}$ at intervals of 1 cm^{-1} . As can be seen from this figure, the region of highest field strength is in the vicinity of the outer corners of the Au-vacuum boundary for the cross-shaped nanostructure (vacuum below the hBN layer), however features can be clearly resolved inside the cross (gold below the hBN layer). Broad features attributed to

plasmons can be observed both below and above the reststrahlen band; these features extend from above the gold region into the vacuum region. Within the frequency range spanned by the reststrahlen band, multiple branches can be observed in both the vacuum and Au regions.

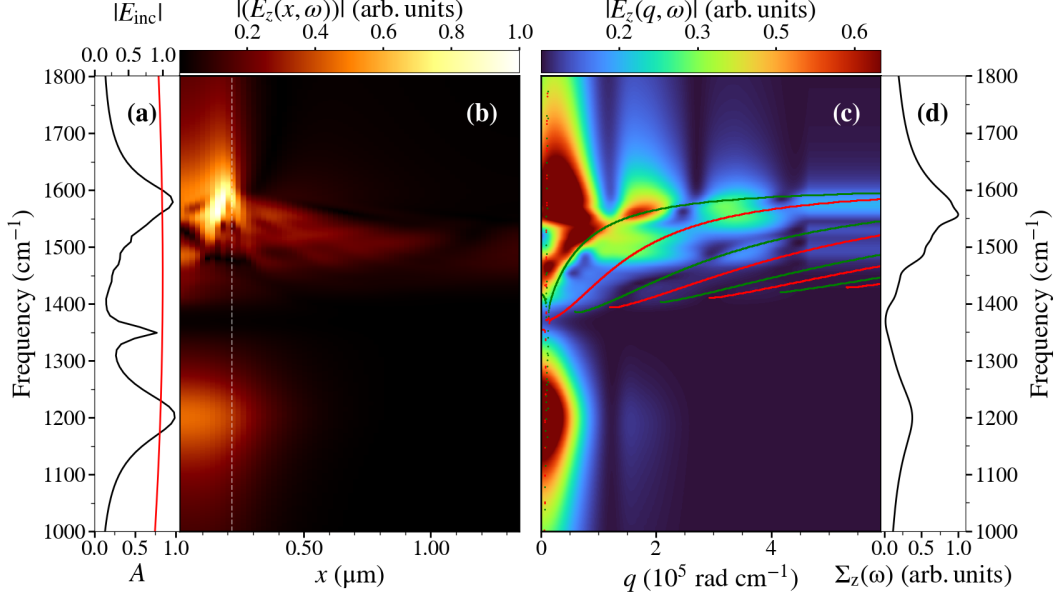


Figure 5.9: Phonon-polariton dispersion curves in the CD with $d_{\text{CC}} = 2.70 \mu\text{m}$. (a) The far-field absorption spectrum. (b) E_z lineouts along the $x = 0 \mu\text{m}$ line for frequencies in the range $\nu = 1000 - 1800 \text{ cm}^{-1}$ with a spectral resolution of 1 cm^{-1} . The spatial extent of the data displayed in this pane is from the center to the edge of the unit cell to avoid duplication. The white dotted line in this pane indicates the boundary between vacuum and Au. (c) The spatial Fourier transform of the (full spatial lineout) data presented in pane (b). This data has been interpolated using a cubic spline algorithm. The resulting plot of $|E_z(q, \omega)|$ enables the phonon-polariton dispersion curves to be visualized. The red and green theoretical dispersion curves are calculated as described in the text. (d) The spectral content of the data in pane (c) obtained by integrating over q .

The phonon-polariton dispersion is explained further in Fig. 5.9. Fig. 5.9 (c) shows the spatial Fourier transform of the (full spatial lineout) data described above. The resulting plot of $|E_z(q, \omega)|$ enables the phonon-polariton dispersion curves to be visualized. In order to aid the interpretation of the data in Fig. 5.9 (c), hBN phonon-polariton dispersion curves are calculated as described in Chapter 3, but for the full six-layer (including substrate) device the

curves in green are for the Vacuum/hBN/Vacuum/SiO₂/Au/Si structure, while the curves in red are for the Vacuum/hBN/Au/SiO₂/Au/Si structure.

As can be seen in Fig. 5.9 (c), the upper green curve (dispersion curve for the Vacuum/hBN/Vacuum/SiO₂/Au/Si structure with $n = 0$) and the upper red curve (dispersion curve for the Vacuum/hBN/Au/SiO₂/Au/Si structure with $n = 1$) overlap regions with large values of $|E_z(q, \omega)|$. As in Chapter 3, the value of $|E_z(q, \omega)|$ decreases strongly with increasing values of n .

The spectral content of the data in Fig. 5.9 (c) is obtained by integrating over q to yield the quantity denoted $\Sigma_z(\omega)$, which is plotted in Fig. 5.9 (d). The resulting spectrum, while exhibiting the general features of the far-field spectrum, shows two notable differences. Firstly, this spectrum suppresses both the residual peak at the hBN TO optical phonon frequency and the low frequency plasmon band centered at $\sim 1200\text{ cm}^{-1}$ relative to the phonon-polariton signal. Secondly, the fine structure within the hBN reststrahlen band is emphasized. As in Chapter 3, the near-field spectrum, $\Sigma_z(\omega)$, emphasizes the slab phonon-polaritons over the bulk phonon-polaritons when compared to the far-field spectrum thus highlighting the importance of using near-field experimental techniques to investigate systems of this kind.

To further investigate the coupling to the hBN phonon-polaritons, the phonon-polariton signal strength in the coupled device was investigated as a function of d_{CC} . In order to better separate the signal originating from the Vacuum/hBN/Vacuum/SiO₂/Au/Si and the Vacuum/hBN/Au/SiO₂/Au/Si regions of the device, a Tukey [93] windowing function was used to mask regions of the real space data in Fig. 5.9 (b) before Fourier transforming that data. The Fourier transformed data that derives from only the Vacuum/hBN/Vacuum/SiO₂/Au/Si region of the $d_{\text{CC}} = 2.70\text{ }\mu\text{m}$ device is shown Fig. 5.10 (a). The theoretical dispersion curves for the Vacuum/hBN/Vacuum/SiO₂/Au/Si structure are overlaid in green. The upper green curve is denoted $\omega_{V,0}(q)$. Similarly, the Fourier transformed data that derives from only the Vacuum/hBN/Au/SiO₂/Au/Si region

of the same device is shown Fig. 5.10 (b) and the theoretical dispersion curves for the Vacuum/hBN/Au/SiO₂/Au/Si structure are overlaid in red. The upper red curve is denoted $\omega_{\text{Au},1}(q)$. Figs. 5.10 (c) and (d) are the same as Figs. 5.10 (a) and (b), respectively, but for the $d_{\text{CC}} = 2.94 \mu\text{m}$ device.

A region of Fig. 5.10 (a) was defined by q in the range $0.15 \times 10^5 - 4.15 \times 10^5 \text{ rad cm}^{-1}$ and ω in the range $\omega_{\text{V},0}(q) \pm 88 \text{ cm}^{-1}$. $|E_z(q, \omega)|$ was integrated over this region to yield the quantity Σ_{V} . Similarly, a region of Fig. 5.10 (b) was defined by q in the range $0.8 \times 10^5 - 4.8 \times 10^5 \text{ rad cm}^{-1}$ and ω in the range $\omega_{\text{Au},1}(q) \pm 88 \text{ cm}^{-1}$. $|E_z(q, \omega)|$ was integrated over this region to yield the quantity Σ_{Au} . This process was repeated for devices with values of d_{CC} in the range $2.06 - 2.94 \mu\text{m}$. $\Sigma_{\text{Au}}(d_{\text{CC}})$ was normalized to its maximum value which occurred at $d_{\text{CC}} = 2.70 \mu\text{m}$ and is plotted in red in Fig. 5.10 (e). $\Sigma_{\text{V}}(d_{\text{CC}})$, which is plotted in green in Fig. 5.10 (e), was also normalized to the maximum value of $\Sigma_{\text{V}}(d_{\text{CC}})$, so that the relative strengths of these two quantities could be directly compared. $\Sigma_{\text{V}}(d_{\text{CC}})$ is approximately half the strength of $\Sigma_{\text{Au}}(d_{\text{CC}})$, but exhibits a similar dependence on d_{CC} .

For comparison, the far-field coupled device (CD) absorptance spectra of Fig. 5.4 (c) were integrated over the reststrahlen band to yield the quantity Σ_{Abs} , which was normalized to its maximum value, which occurred at $d_{\text{CC}} = 2.70 \text{ nm}$. Σ_{Abs} is plotted in blue in Fig. 5.10 (f).

A careful examination of Fig. 5.10 (a), (b), (c) and (d) reveals that, similar to the devices in Chapter 3, but unlike the devices in Chapter 4, the phonon-polaritons excited in the $d_{\text{CC}} = 2.94 \mu\text{m}$ device are downshifted in both frequency and wave-vector compared to the corresponding phonon-polariton in the $d_{\text{CC}} = 2.70 \mu\text{m}$ device. This behavior is systematic as is demonstrated by the data in Fig. 5.10 (g), which shows both a plot of the frequency at which the maximum Vacuum/hBN/Vacuum/SiO₂/Au/Si phonon-polariton signal occurs (plotted in green) and a plot of the frequency at which the maximum Vacuum/hBN/Au/SiO₂/Au/Si phonon-polariton signal occurs (plotted in red) as a function of d_{CC} . The dependence of the value of q at which the maximum phonon-polariton signals

occur as function of d_{CC} (not shown) follow a similar trend to the frequency data. The data (plotted in blue) in Fig. 5.10 (h) shows the peak of the high frequency far-field absorptance band from Fig. 5.5. The above data and associated discussion indicates that, similar to the device in Chapter 3, the frequency/wavevector of the phonon-polariton can be tuned over a limited spectral region by varying d_{CC} .

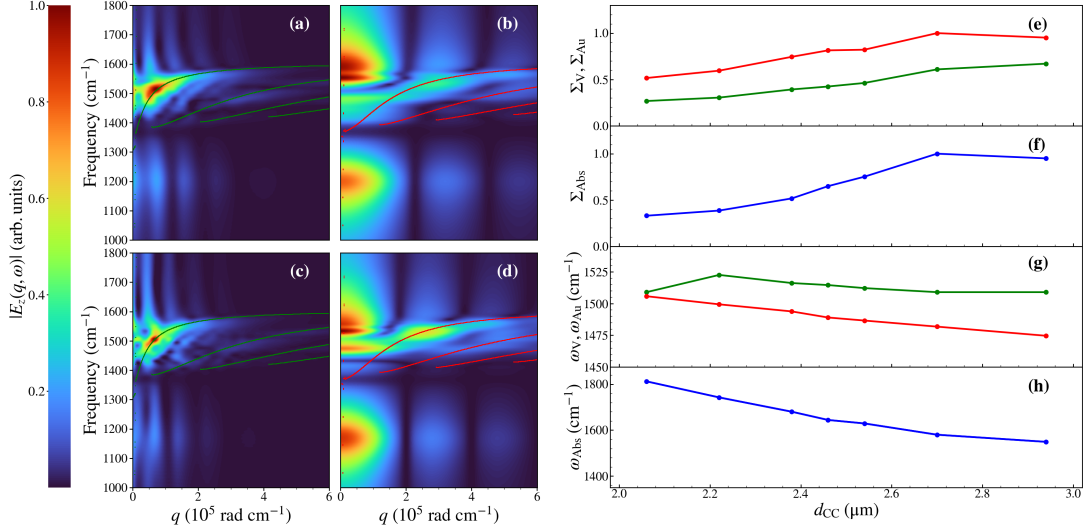


Figure 5.10: Vacuum/hBN/Vacuum/SiO₂/Au/Si and Vacuum/hBN/Au/SiO₂/Au/Si phonon-polariton signal strength and frequency dependence in the CDs as a function of d_{CC} . (a) The spatial Fourier transform of the Vacuum/hBN/Vacuum/SiO₂/Au/Si masked data from pane Fig. 5.9 (b). The green theoretical dispersion curves are for the Vacuum/hBN/Vacuum/SiO₂/Au/Si system. (c) The spatial Fourier transform of the Vacuum/hBN/Vacuum/SiO₂/Au/Si masked data from pane Fig. 5.9 (b). The red theoretical dispersion curves are for the Vacuum/hBN/Vacuum/SiO₂/Au/Si system. Pane (c) and (d) are the same as pane (a) and (b), but for the $d_{CC} = 2.94 \mu\text{m}$ device. (e) Green: The integrated Vacuum/hBN/Vacuum/SiO₂/Au/Si phonon-polariton signal strength plotted as a function of d_{CC} . Red: The integrated Vacuum/hBN/Vacuum/SiO₂/Au/Si phonon-polariton signal strength plotted as a function of d_{CC} . (f) Blue: The far-field absorptance spectra from Fig. 5.5 integrated over the spectral region of the reststrahlen band plotted as a function of d_{CC} . (g) Green: The frequency at which the peak of the Vacuum/hBN/Vacuum/SiO₂/Au/Si phonon-polariton signal strength occurs plotted as a function of d_{CC} . Red: The frequency at which the peak of the Vacuum/hBN/Vacuum/SiO₂/Au/Si phonon-polariton signal strength occurs plotted as a function of d_{CC} . (h) Blue: The peak of the high frequency far-field absorptance band from Fig. 5.5. The lines in panes (e), (f), (g) and (h) are guides to the eye.

5.5 Conclusions

The excitations that occur in a hBN/nanopatterned Au cross “perfect” absorber device have been investigated using the Finite-Difference Time-Doman (FDTD) method. In order to gain a more detailed understanding of the coupling between the phonon-polaritons in the hBN layer and the plasmon-polaritons in the Au nanostructures, the far- and near-field properties of this coupled device (CD) were compared with the properties of three other uncoupled devices denoted BD (supports plasmon-polaritons only), UCDI (supports plasmon-polaritons only) and UCDII (supports phonon-polaritons only). An examination of the far-field absorptance spectra of the above devices show that in the coupled device the absorptance peak, associated with the plasmon-polariton in UCDI, splits due to the interaction with the bulk phonon-polariton in hBN, while an examination of the absorptance fine-structure provides evidence of slab phonon-polaritons in hBN. Furthermore the addition of the Au grounding sheet greatly increases the ability to observe the TO phonon-polaritons with far-field methods. This addition also eliminates the existence of rayleigh anomalies within the spectral range studied.

An investigation of the near-field electric field distributions enables the slab phonon-polaritons to be identified and categorized according to mode number per Eq. 3.1 and supporting layer, *i.e.*, vacuum or Au. A comparison of the field maps for the CD and UCDII show that the presence of the plasmon-polaritons in the CD increases the contrast in the spatial electric field variation indicating that the plasmon plays a key role in both coupling energy into the hBN phonon-polaritons and in launching phonon-polaritons into different directions within the hBN layer.

By examining the dependence of the phonon-polariton excitation on the device periodicity, d_{CC} , it was observed that the frequency/wavevector of the phonon-polariton can be tuned by varying d_{CC} . Furthermore the strength of the phonon-polariton signal varies with d_{CC} and that variation is dominated by the spectral overlap of the far-field absorptance spectrum with the reststrahlen band.

Chapter 6

Conclusions

In this dissertation, plasmon-polaritons, phonon-polaritons and their interactions were investigated in a suite of devices that combine a hexagonal boron nitride (hBN) thin film with a nanopatterned metal film in a layered device. Three classes of device geometries were investigated in this dissertation: (i) an hBN layer on a nanopatterned square array of cross apertures in a gold layer; (ii) an hBN layer on a nanopatterned hexagonal array of circular apertures in a silver layer and (iii) an hBN layer on a nanopatterned square array of gold crosses separated from a ground plane by a dielectric spacer.

These devices were simulated using the Finite-Difference Time-Domain (FDTD) method as implemented by an in-house code that was developed specifically for the research projects described in this dissertation. The in-house code was written in the C programming language and implemented the following capabilities that were necessary for the successful completion of this study: Periodic boundary conditions, convolution perfectly matched layers (CPML), isotropic dielectric (Si , SiO_2) and metallic (Ag , Au) materials and anisotropic frequency dependent materials (hBN). In order to perform the required calculations, with both sufficient spatial resolution and an adequate number of timesteps, it was essential to parallelize the code. The code was therefore written to leverage the Nvidia OpenACC and CUDA frameworks in order to implement parallel execution on a graphical processing unit (GPU). When

run on an Nvidia P100 GPU with 3584 cores, this resulted in a speed-up of the code by a factor of ~ 70 compared with single threaded execution on an Intel Xeon Broadwell CPU. This speed-up was sufficient to perform the simulations necessary to complete this dissertation research.

Both far-field and near-field properties were investigated. In particular, the far-field properties investigated were the reflectance, transmittance and absorptance spectra. The following general far-field properties were observed for the three classes of device geometries: (i) The hBN layer on a nanopatterned square array of cross apertures in a gold layer exhibited smooth Gaussian-like absorption spectra with well separated Rayleigh anomalies in most cases. The simplicity of the spectra made the far-field data from this class of device clearer and easier to interpret than some of the other device classes. As a consequence, the near-field data from this device provided a framework by which the other device classes could be evaluated. (ii) The hBN layer on a nanopatterned hexagonal array of circular apertures in a silver layer exhibited highly assymmetric absorptance line shapes due to the overlap of the Rayleigh anomalies with the plasmonic absorptance bands. (iii) The hBN layer on a nanopatterned square array of gold crosses separated from a ground plane by a dielectric spacer exhibited behavior similar that in (i) but with all devices exhibiting zero transmission and some devices exhibiting perfect absorptance peaks as expected for this geometry. Furthermore, this device structure appeared to completely suppress the occurrence of Rayleigh anomalies.

For all three device geometries studied in this dissertation, multiple control devices were also studied, these were (i) a bare device in which the hBN layer was removed, (ii) an uncoupled device in which the hBN layer was replaced by a dielectric layer, and (iii) a second uncoupled device in which the metal in the plasmonic layer was replaced by a high index dielectric material. For all three device geometries, the bare device showed reflectance, transmittance (*n.b.*, the transmittance of the “perfect” absorber device was zero) and absorption spectra that red shifted as the device periodicity, d_{CC} was increased. The spectra for the un-

coupled device in which the hBN layer was replaced by a dielectric layer, exhibited a slightly greater red shift when compared to the bare device. However, in the case of the coupled device, the reflectance transmittance and absorption peaks split into two peaks, one either side of the hBN transverse optical phonon frequency. Multiple additional small features were observed in the coupled device spectra and this fine-structure provides evidence of slab phonon-polaritons in hBN. Rayleigh anomalies were observed in the first two of the above device classes, but not the third.

An investigation of the near-field electric field distributions enables the slab phonon-polaritons to be identified and categorized according to mode number and the immediate supporting layer, *i.e.*, vacuum or metal. The transverse magnetic slab phonon-polariton modes in hBN agree with those predicted by theory and demonstrate both strong confinement to the hBN layer and slow group velocity. A comparison of the field maps for the coupled device and the second uncoupled device, in which the metal in the plasmonic layer was replaced by a high index dielectric material, shows that the presence of the plasmon-polaritons in the coupled device increases the contrast in the spatial electric field variation indicating that the plasmon plays a key role in both coupling energy into the hBN phonon-polaritons and in launching phonon-polaritons into different directions within the hBN layer. By examining the dependence of the phonon-polariton excitation on the device periodicity, d_{CC} , it was observed that for the first and third device classes, the frequency/wavevector of the phonon-polariton could be tuned by varying d_{CC} . Furthermore, it was observed that for all three device classes, the strength of the phonon-polariton signal varied with d_{CC} and that variation is dominated by the spectral overlap of the far-field absorptance spectrum with the reststrahlen band. Thus the frequency/wavevector of the phonon-polariton can be tuned over a limited spectral region by varying d_{CC} .

More generally, the combination of the field enhancement and tunability afforded by the plasmonic nanostructured layer combined with the field confinement and slow group velocity exhibited by the hBN layer, suggests that the devices studied in this dissertation could find

applications as an interesting platform for high sensitivity sensor development. It is hoped that the detailed simulations presented in this dissertation will be helpful in informing future experimental investigations of these interesting and technologically relevant systems.

Bibliography

- [1] Jipeng Wu, Hengliang Wang, Leyong Jiang, Jun Guo, Xiaoyu Dai, Yuanjiang Xiang, and Shuangchun Wend. Critical coupling using the hexagonal boron nitride crystals in the mid-infrared range. *J. Appl. Phys.*, 119:203107, 2016.
- [2] P. Pons-Valencia, F. J. Alfaro-Mozaz, M. M. Wiecha, V. Biolek, I. Dolado, S. Vélez, P. Li, P. Alonso-González, F. Casanova, L. E. Hueso, L. Martín-Moreno, R. Hillenbrand, and A. Y. Nikitin. Launching of hyperbolic phonon-polaritons in h-bn slabs by resonant metal plasmonic antennas. *Nat. Commun.*, 10:3242, 2019.
- [3] Stefan A. Maier and Harry A. Atwater. Plasmonics: Localization and guiding of electromagnetic energy in metal/dielectric structures. *Journal of Applied Physics*, 98(1):011101, 2005.
- [4] Maria Losurdo, Fernando Moreno, Christoph Cobet, Mircea Modreanu, and Wolfram Pernice. Plasmonics: Enabling functionalities with novel materials. *J. Appl. Phys.*, 129:220401, 2021.
- [5] K. B. Tolpygo. Physical properties of a rock salt lattice made up of deformable ions. *Zh. Eksp. Teor. Fiz.*, 20:497–509, 1950.
- [6] K. U. N. Huang. Lattice vibrations and optical waves in ionic crystals. *Nature*, 167(4254):779–780, 1951.

- [7] A. J. Huber, B. Deutsch, L. Novotny, and R. Hillenbrand. Focusing of surface phonon polaritons. *Appl. Phys. Lett.*, 92(20):203104, 2008.
- [8] William L. Barnes, Alain Dereux, and Thomas W. Ebbesen. Surface plasmon subwavelength optics. *Nature*, 424(6950):824–830, 2003.
- [9] R. H. Ritchie. Plasma losses by fast electrons in thin films. *Phys. Rev.*, 106(5):874–881, 1957.
- [10] David Pines and David Bohm. A collective description of electron interactions: II. collective vs individual particle aspects of the interactions. *Phys. Rev.*, 85(2):338–353, 1952.
- [11] W. Andrew Murray and William L. Barnes. Plasmonic mater. *Adv. Mater.*, 19:3771–3782, 2007.
- [12] John Pendry. Playing tricks with light. *Science*, 285(5434):1687–1688, 1999.
- [13] Joshua D. Caldwell, Andrey V. Kretinin, Yiguo Chen, Vincenzo Giannini, Michael M. Fogler, Yan Francescato, Chase T. Ellis, Joseph G. Tischler, Colin R. Woods, Alexander J. Giles, Minghui Hong, Kenji Watanabe, Takashi Taniguchi, Stefan A. Maier, and Kostya S. Novoselov. Sub-diffractive volume-confined polaritons in the natural hyperbolic material hexagonal boron nitride. *Nat. Commun.*, 5(1):5221, 2014.
- [14] R. Estevâm da Silva, R. Macêdo, T. Dumelow, J. A. P. da Costa, S. B. Honorato, and A. P. Ayala. Far-infrared slab lensing and subwavelength imaging in crystal quartz. *Phys. Rev. B*, 86(15):155152, 2012.
- [15] Nicholas Fang, Hyesog Lee, Cheng Sun, and Xiang Zhang. Sub-diffraction-limited optical imaging with a silver superlens. *Science*, 308(5721):534–537, 2005.

- [16] Katrin Kneipp, Yang Wang, Harald Kneipp, Lev T Perelman, Irving Itzkan, Ramachandra R Dasari, and Michael S Feld. Single molecule detection using surface-enhanced raman scattering (sers). *Phys. Rev. Lett.*, 78(9):1667, 1997.
- [17] Chad E Talley, Joseph B Jackson, Chris Oubre, Nathaniel K Grady, Christopher W Hollars, Stephen M Lane, Thomas R Huser, Peter Nordlander, and Naomi J Halas. Surface-enhanced raman scattering from individual au nanoparticles and nanoparticle dimer substrates. *Nano. Lett.*, 5(8):1569–1574, 2005.
- [18] Daniel Rodrigo, Odetta Limaj, Davide Janner, Dordaneh Etezadi, F. Javier García de Abajo, Valerio Pruneri, and Hatice Altug. Mid-infrared plasmonic biosensing with graphene. *Science*, 349(6244):165–168, 2015.
- [19] Alireza Fali, Samuel T. White, Thomas G. Folland, Mingze He, Neda A. Aghamiri, Song Liu, James H. Edgar, Joshua D. Caldwell, Richard F. Haglund, and Yohannes Abate. Refractive index-based control of hyperbolic phonon-polariton propagation. *Nano. Lett.*, 19(11):7725–7734, 2019.
- [20] DE Chang, Anders Søndberg Sørensen, PR Hemmer, and MD Lukin. Quantum optics with surface plasmons. *Phys. Rev. Lett.*, 97(5):053002, 2006.
- [21] A Gonzalez-Tudela, Diego Martin-Cano, Esteban Moreno, Luis Martin-Moreno, C Tejedor, and Francisco J Garcia-Vidal. Entanglement of two qubits mediated by one-dimensional plasmonic waveguides. *Phys. Rev. Lett.*, 106(2):020501, 2011.
- [22] Ganesh R Bhimanapati, Zhong Lin, Vincent Meunier, Yeonwoong Jung, Judy Cha, Saptarshi Das, Di Xiao, Youngwoo Son, Michael S Strano, and Valentino R Cooper. Recent advances in two-dimensional materials beyond graphene. *ACS Nano.*, 9(12):11509–11539, 2015.

- [23] Frank HL Koppens, Darrick E Chang, and F Javier Garcia de Abajo. Graphene plasmonics: a platform for strong light–matter interactions. *Nano. Lett.*, 11(8):3370–3377, 2011.
- [24] S Dai, Z Fei, Q Ma, AS Rodin, M Wagner, AS McLeod, MK Liu, W Gannett, W Regan, and K Watanabe. Tunable phonon polaritons in atomically thin van der waals crystals of boron nitride. *Science*, 343(6175):1125–1129, 2014.
- [25] Anshuman Kumar, Tony Low, Kin Hung Fung, Phaedon Avouris, and Nicholas X. Fang. Tunable light–matter interaction and the role of hyperbolicity in graphene–hbn system. *Nano. Lett.*, 15(5):3172–3180, 2015.
- [26] S. A. Biehs, M. Tschikin, and P. Ben-Abdallah. Hyperbolic metamaterials as an analog of a blackbody in the near field. *Phys. Rev. Lett.*, 109(10):104301, 2012.
- [27] Yu Guo, Ward Newman, Cristian L Cortes, and Zubin Jacob. Applications of hyperbolic metamaterial substrates. *Adv. OptoElectron.*, 2012.
- [28] C. L. Cortes, W. Newman, S. Molesky, and Z. Jacob. Quantum nanophotonics using hyperbolic metamaterials. *J. Opt.*, 14(6):063001, 2012.
- [29] F. Bonaccorso, Z. Sun, T. Hasan, and A. C. Ferrari. Graphene photonics and optoelectronics. *Nat. Photon.*, 4(9):611–622, 2010.
- [30] Zubin Jacob, Igor I. Smolyaninov, and Evgenii E. Narimanov. Broadband purcell effect: Radiative decay engineering with metamaterials. *Appl. Phys. Lett.*, 100(18):181105, 2012.
- [31] Zhaowei Liu, Hyesog Lee, Yi Xiong, Cheng Sun, and Xiang Zhang. Far-field optical hyperlens magnifying sub-diffraction-limited objects. *Science*, 315(5819):1686–1686, 2007.
- [32] A. V. Kretinin, Y. Cao, J. S. Tu, G. L. Yu, R. Jalil, K. S. Novoselov, S. J. Haigh, A. Gholinia, A. Mishchenko, M. Lozada, T. Georgiou, C. R. Woods, F. Withers,

- P. Blake, G. Eda, A. Wirsig, C. Hucho, K. Watanabe, T. Taniguchi, A. K. Geim, and R. V. Gorbachev. Electronic properties of graphene encapsulated with different two-dimensional atomic crystals. *Nano. Lett.*, 14(6):3270–3276, 2014.
- [33] C. R. Dean, A. F. Young, I. Meric, C. Lee, L. Wang, S. Sorgenfrei, K. Watanabe, T. Taniguchi, P. Kim, K. L. Shepard, and J. Hone. Boron nitride substrates for high-quality graphene electronics. *Nat. Nanotechnol.*, 5(10):722–726, 2010.
- [34] C. R. Dean, L. Wang, P. Maher, C. Forsythe, F. Ghahari, Y. Gao, J. Katoch, M. Ishigami, P. Moon, M. Koshino, T. Taniguchi, K. Watanabe, K. L. Shepard, J. Hone, and P. Kim. Hofstadter’s butterfly and the fractal quantum hall effect in moiré superlattices. *Nature*, 497(7451):598–602, 2013.
- [35] B. Hunt, J. D. Sanchez-Yamagishi, A. F. Young, M. Yankowitz, B. J. LeRoy, K. Watanabe, T. Taniguchi, P. Moon, M. Koshino, P. Jarillo-Herrero, and R. C. Ashoori. Massive dirac fermions and hofstadter butterfly in a van der waals heterostructure. *Science*, 340(6139):1427–1430, 2013.
- [36] G. L. Yu, R. V. Gorbachev, J. S. Tu, A. V. Kretinin, Y. Cao, R. Jalil, F. Withers, L. A. Ponomarenko, B. A. Piot, M. Potemski, D. C. Elias, X. Chen, K. Watanabe, T. Taniguchi, I. V. Grigorieva, K. S. Novoselov, V. I. Fal’ko, A. K. Geim, and A. Mishchenko. Hierarchy of hofstadter states and replica quantum hall ferromagnetism in graphene superlattices. *Nat. Phys.*, 10(7):525–529, 2014.
- [37] F. D. M. Haldane and S. Raghu. Possible realization of directional optical waveguides in photonic crystals with broken time-reversal symmetry. *Phys. Rev. Lett.*, 100(1):013904, 2008.
- [38] S. Raghu and F. D. M. Haldane. Analogs of quantum-hall-effect edge states in photonic crystals. *Phys. Rev. A*, 78(3):033834, 2008.

- [39] Guorui Chen, Aaron L. Sharpe, Patrick Gallagher, Ilan T. Rosen, Eli J. Fox, Lili Jiang, Bosai Lyu, Hongyuan Li, Kenji Watanabe, Takashi Taniguchi, Jeil Jung, Zhiwen Shi, David Goldhaber-Gordon, Yuanbo Zhang, and Feng Wang. Signatures of tunable superconductivity in a trilayer graphene moiré superlattice. *Nature*, 572(7768):215–219, 2019.
- [40] Guorui Chen, Aaron L. Sharpe, Eli J. Fox, Ya-Hui Zhang, Shaoxin Wang, Lili Jiang, Bosai Lyu, Hongyuan Li, Kenji Watanabe, Takashi Taniguchi, Zhiwen Shi, T. Senthil, David Goldhaber-Gordon, Yuanbo Zhang, and Feng Wang. Tunable correlated chern insulator and ferromagnetism in a moiré superlattice. *Nature*, 579(7797):56–61, 2020.
- [41] K. S. Novoselov, A. Mishchenko, A. Carvalho, and A. H. Castro Neto. 2d materials and van der waals heterostructures. *Science*, 353(6298):aac9439, 2016.
- [42] A. K. Geim and I. V. Grigorieva. Van der waals heterostructures. *Nature*, 499(7459):419–425, 2013.
- [43] Achim Woessner, Mark B. Lundeberg, Yuanda Gao, Alessandro Principi, Pablo Alonso-González, Matteo Carrega, Kenji Watanabe, Takashi Taniguchi, Giovanni Vignale, Marco Polini, James Hone, Rainer Hillenbrand, and Frank H. L. Koppens. Highly confined low-loss plasmons in graphene–boron nitride heterostructures. *Nat. Mater.*, 14(4):421–425, 2015.
- [44] Bo Zhao and Zhuomin M. Zhang. Perfect mid-infrared absorption by hybrid phonon-plasmon polaritons in hbn/metal-grating anisotropic structures. *Int. J. Heat Mass Transf.*, 106:1025–1034, 2017.
- [45] Jiong Yang, Mohannad Mayyas, Jianbo Tang, Mohammad B. Ghasemian, Honghua Yang, Kenji Watanabe, Takashi Taniguchi, Qingdong Ou, Lu Hua Li, Qiaoliang Bao, and Kourosh Kalantar-Zadeh. Boundary-induced auxiliary features in scattering-type near-field fourier transform infrared spectroscopy. *ACS Nano*, 14(1):1123–1132, 2020.

- [46] F. J. Alfaro-Mozaz, P. Alonso-González, S. Vélez, I. Dolado, M. Autore, S. Mastel, F. Casanova, L. E. Hueso, P. Li, A. Y. Nikitin, and R. Hillenbrand. Nanoimaging of resonating hyperbolic polaritons in linear boron nitride antennas. *Nat. Commun.*, 8(1):15624, 2017.
- [47] Marta Autore, Peining Li, Irene Dolado, Francisco J. Alfaro-Mozaz, Ruben Esteban, Ainhoa Atxabal, Félix Casanova, Luis E. Hueso, Pablo Alonso-González, Javier Aizpuru, Alexey Y. Nikitin, Saül Vélez, and Rainer Hillenbrand. Boron nitride nanoresonators for phonon-enhanced molecular vibrational spectroscopy at the strong coupling limit. *Light Sci. Appl.*, 7(4):17172–17172, 2018.
- [48] T. G. Folland, A. Fali, S. T. White, J. R. Matson, S. Liu, N. A. Aghamiri, J. H. Edgar, R. F. Haglund, Y. Abate, and J. D. Caldwell. Reconfigurable infrared hyperbolic metasurfaces using phase change materials. *Nat. Commun.*, 9(1):4371, 2018.
- [49] Fei Cheng, Xiaodong Yang, and Jie Gao. Ultrasensitive detection and characterization of molecules with infrared plasmonic metamaterials. *Sci. Rep.*, 5(1):14327, 2015.
- [50] Weiwei Wan, Xiaodong Yang, and Jie Gao. Strong coupling between mid-infrared localized plasmons and phonons. *Opt. Express*, 24(11):12367–12374, May 2016.
- [51] R. A. Shelby, D. R. Smith, and S. Schultz. Experimental verification of a negative index of refraction. *Science*, 292(5514):77–9, 2001.
- [52] Kang Yang, Jingyu Wang, Xu Yao, Danya Lyu, Jinfeng Zhu, Zhilin Yang, Bowen Liu, and Bin Ren. Large-area plasmonic metamaterial with thickness-dependent absorption. *Advanced Optical Materials*, 9(1):2001375, 2021.
- [53] Na Liu, Martin Mesch, Thomas Weiss, Mario Hentschel, and Harald Giessen. Infrared perfect absorber and its application as plasmonic sensor. *Nano Letters*, 10(7):2342–2348, 2010. PMID: 20560590.

- [54] D. J. Shelton, I. Brener, J. C. Ginn, M. B. Sinclair, D. W. Peters, K. R. Coffey, and G. D. Boreman. Strong coupling between nanoscale metamaterials and phonons. *Nano Letters*, 11(5):2104–2108, 2011.
- [55] Xuejin Zhang, Dongmin Wu, Cheng Sun, and Xiang Zhang. Artificial phonon-plasmon polariton at the interface of piezoelectric metamaterials and semiconductors. *Phys. Rev. B*, 76:085318, Aug 2007.
- [56] Alexander Benz, Salvatore Campione, John F. Klem, Michael B. Sinclair, and Igal Brener. Control of strong light–matter coupling using the capacitance of metamaterial nanocavities. *Nano Letters*, 15(3):1959–1966, 2015. PMID: 25625404.
- [57] Yee Kane. Numerical solution of initial boundary value problems involving maxwell’s equations in isotropic media. *IEEE Trans. Antennas Propag.*, 14(3):302–307, 1966.
- [58] A. Nemirovski, M. Gonidec, J. M. Fox, P. Jean-Remy, E. Turnage, and G. M. Whitesides. Engineering shadows to fabricate optical metasurfaces. *ACS Nano*, 8:11061–11070, 2014.
- [59] Xianliang Liu, Tatiana Starr, Anthony F. Starr, and Willie J. Padilla. Infrared spatial and frequency selective metamaterial with near-unity absorbance. *Phys. Rev. Lett.*, 104:207403, May 2010.
- [60] Fei Cheng, Xiaodong Yang, and Jie Gao. Enhancing intensity and refractive index sensing capability with infrared plasmonic perfect absorbers. *Opt. Lett.*, 39(11):3185–3188, Jun 2014.
- [61] H. A. MacLeod. *Thin-Film Optical Filters*. CRC Press, 2001.
- [62] Peter P. Sylvester and Ronald L. Ferrari. *Finite Elements for Electrical Engineers*. Cambridge University Press, 3 edition, 1996.
- [63] David B. Davidson. *Computational Electromagnetics for RF and Microwave Engineering*. Cambridge University Press, 2 edition, 2010.

- [64] A. D. Grigoriev, R. V. Salimov, and R. I. Tikhonov. A finite element method in electrodynamics. problems and solutions. In *2006 International Conference on Actual Problems of Electron Devices Engineering*, pages 281–287, 2006.
- [65] K. Mei and J. Van Bladel. Scattering by perfectly-conducting rectangular cylinders. *IEEE Transactions on Antennas and Propagation*, 11(2):185–192, 1963.
- [66] Luis E. Tobón, Qiang Ren, and Qing Huo Liu. A new efficient 3d discontinuous galerkin time domain (dgtd) method for large and multiscale electromagnetic simulations. *Journal of Computational Physics*, 283:374–387, 2015.
- [67] Paul Kinsler. Optical pulse propagation with minimal approximations. *Phys. Rev. A*, 81:013819, Jan 2010.
- [68] Raymond C. Rumpf. The Perfectly Matched Layer, EMPossible, 2020. [Online; accessed 10-7-2021].
- [69] J. B. Schneider and C. L. Wagner. Fdtd dispersion revisited: faster-than-light propagation. *IEEE Microwave and Guided Wave Letters*, 9(2):54–56, 1999.
- [70] A. Taflove and S.C. Hagness. *Computational Electrodynamics: The Finite-difference Time-domain Method*. Artech House, 2005.
- [71] Sh. J. Huang and F. Li. Fdtd simulation of electromagnetic propagation in magnetized plasma using z transforms. *Int. J. Infrared Milli. Waves*, 25(5):815–825, 2004.
- [72] Dennis M. Sullivan. Z-transform theory and the fdtd method. *IEEE Trans. Antennas Propag.*, 44(1):28–34, 1996.
- [73] Dennis M. Sullivan. *Electromagnetic Simulation Using the FDTD Method, Second Edition*. Wiley, 2013.

- [74] Arkadiusz Ciesielski, Lukasz Skowronski, Marek Trzcinski, Ewa Górecka, Paweł Trautman, and Tomasz Szoplik. Evidence of germanium segregation in gold thin films. *Surf. Sci.*, 674:73–78, 2018.
- [75] Yuyu Jiang, Xiao Lin, Tony Low, Baile Zhang, and Hongsheng Chen. Group-velocity-controlled and gate-tunable directional excitation of polaritons in graphene-boron nitride heterostructures. *Laser Photonics Rev.*, 12(5):1800049, 2018.
- [76] Norman Ricker. Further developments in the wavelet theory of seismogram structure. *Bulletin of the Seismological Society of America*, 33(3):197–228, 1943.
- [77] Yang Hao and Raj Mittra. *FDTD Modeling of Metamaterials: Theory and Applications*. Artech House, 2008.
- [78] J. D. Joannopoulos S. G. Johnson. Introduction to photonic crystals: Bloch’s theorem, band diagrams, and gaps (but no defects), 2003.
- [79] John D. Joannopoulos, Steven G. Johnson, Joshua N. Winn, and Robert D. Meade. *Photonic Crystals: Molding the Flow of Light (Second Edition)*. Princeton University Press, 2 edition, 2008.
- [80] A. Taflove. *Advances in Computational Electrodynamics: The Finite-difference Time-domain Method*. Artech House antenna library. Artech House, 1998.
- [81] Raymond C. Rumpf. Formulation of Plane Wave Expansion Method, EMPossible, 2020. [Online; accessed 7-July-2021].
- [82] Andrei Bylinkin, Martin Schnell, Marta Autore, Francesco Calavalle, Peining Li, Javier Taboada-Gutiérrez, Song Liu, James H. Edgar, Fèlix Casanova, Luis E. Hueso, Pablo Alonso-Gonzalez, Alexey Y. Nikitin, and Rainer Hillenbrand. Real-space observation of vibrational strong coupling between propagating phonon polaritons and organic molecules. *Nat. Photon.*, 15:197–202, 2021.

- [83] PGI Compilers and Tools: OpenACC Getting Started Guide, NVIDIA, 11/19/2020 2020.
- [84] D. E. Merewether, R. Fisher, and F. W. Smith. On implementing a numeric huygen's source scheme in a finite difference program to illuminate scattering bodies. *IEEE Trans. Nucl. Sci.*, 27(6):1829–1833, 1980.
- [85] Branko D Gvozdic and Dusan Z Djurdjevic. Performance advantages of cpml over upml absorbing boundary conditions in fdtd algorithm. *J. Electr. Eng.*, 68(1):47–53, 2017.
- [86] Zachary S Sacks, David M Kingsland, Robert Lee, and Jin-Fa Lee. A perfectly matched anisotropic absorber for use as an absorbing boundary condition. *IEEE Trans. Antennas Propag.*, 43(12):1460–1463, 1995.
- [87] R. W. Wood. On a remarkable case of uneven distribution of light in a diffraction grating spectrum. *Lond. Edinb. Dublin Philos. Mag. J. Sci.*, 4:396–402, 1902.
- [88] L. Rayleigh. On the dynamical theory of gratings. *Proc. R. Soc. Lond. A.*, 79:399–416, 1907.
- [89] H. Gao, J. M. McMahon, M. H. Lee, J. Henzie, S. K. Gray, G. C. Schatz, and T. W. Odom. Rayleigh anomaly-surface plasmon polariton resonances in palladium and gold subwavelength hole arrays. *Opt. Express*, 17:2334–2340, 2009.
- [90] Angela E. Klein, Norik Janunts, Michael Steinert, Andreas Tünnermann, and Thomas Pertsch. Polarization-resolved near-field mapping of plasmonic aperture emission by a dual-snom system. *Nano. Lett.*, 14:5010–5015, 2014.
- [91] William H. Press, Saul A. Teukolsky, William T. Vetterling, and Brian P. Flannery. *Numerical Recipes: The Art of Scientific Computing*. Cambridge University Press, 3rd edition, 2007.
- [92] S. J. Orfanidis. *Electromagnetic Waves and Antennas*. Rutgers University, 2016.

- [93] P. Bloomfield. *Fourier Analysis of Time Series: An Introduction*. Wiley-Interscience, 2nd edition, 2000.
- [94] Yasa Ekşioğlu, Arif E. Cetin, and Jiří Petráček. Optical response of plasmonic nanohole arrays: Comparison of square and hexagonal lattices. *Plasmonics*, 11(3):851–856, 2016.
- [95] Edward D. Palik. *Handbook of optical constants of solids*. Academic Press, Orlando, 1985.

Appendix A

The Z -Transform

The Z -transform converts a discrete-time signal into a complex frequency-domain representation. It can be viewed both as the Laplace transform of a discrete-time signal and as the Laurent expansion of an analytic function. The application of the Z -transform to the finite-difference time-domain (FDTD) method is detailed in Appendix I of the book by Sullivan [73]. In this appendix, the Z -transform is used to derive the update equations for the Debye-Drude model. Update equations for other materials models can be derived in a similar manner.

The Z -transform applies to discrete-time functions, which are represented mathematically as sequences of numbers. *i.e.*, $x = \{x[n]\}$, where $x[n]$ can be written in terms of the corresponding continuous function $x(t)$ as $x[n] = x(n\Delta t)$. The utility of the Z -transform to the finite-difference time-domain (FDTD) method is that it can be used to directly generate a set of difference equations from a constitutive relation defined in the Fourier domain, such as

$$\mathbf{D}(\omega) = \varepsilon(\omega)\mathbf{E}(\omega). \quad (\text{A.1})$$

In the time domain this relation becomes a convolution

$$\mathbf{D}(t) = \int_{-\infty}^{\infty} \varepsilon(t - \tau)\mathbf{E}(\tau)d\tau. \quad (\text{A.2})$$

For a discrete-time function this becomes

$$\mathbf{D}[m] = \Delta t \sum_{n=0}^{\infty} \varepsilon[m-n] \mathbf{E}[n]. \quad (\text{A.3})$$

Note the inclusion of the time step Δt in this definition of the convolution. This form of the convolution is required to explicitly include the time step, Δt , in the update equations.

For a discrete-time signal $x[n]$ the Z -transform is defined by

$$X(z) = Z\{x[n]\} = \sum_{n=-\infty}^{\infty} x[n]z^{-n} \quad (\text{A.4})$$

A useful feature of the Z -transform is the shifting property

$$Z\{x[n-m]\} = z^{-m}X(z), \quad (\text{A.5})$$

this property provides the connection between the Z -transform and difference equations.

The dielectric function for the Debye-Drude model is given by the following response function in the time-domain

$$\varepsilon(t) = \varepsilon_{\infty} + \frac{(\varepsilon_s - \varepsilon_{\infty})}{\tau_0} \Theta(t) e^{-t/\tau_0} + \frac{\sigma}{\omega \varepsilon_0} \Theta(t), \quad (\text{A.6})$$

in the Fourier domain Debye-Drude model becomes

$$\varepsilon(\omega) = \varepsilon_{\infty} + \frac{(\varepsilon_s - \varepsilon_{\infty})}{\tau_0} \frac{1}{1/\tau_0 - i\omega} - \frac{\sigma}{i\omega \varepsilon_0}. \quad (\text{A.7})$$

As will be derived below, the Debye-Drude model in the Z -domain is given by

$$\varepsilon(z) = \varepsilon_{\infty} + \frac{(\varepsilon_s - \varepsilon_{\infty})}{\tau_0} \frac{1}{1 - e^{-\Delta t/\tau_0} z^{-1}} + \frac{\sigma}{\varepsilon_0} \frac{1}{1 - z^{-1}}. \quad (\text{A.8})$$

In the Z -domain the constitutive relation becomes

$$\mathbf{D}(z) = \varepsilon_\infty \mathbf{E}(z) + \Delta t \left(\frac{(\varepsilon_s - \varepsilon_\infty)}{\tau_0} \frac{1}{1 - e^{-\Delta t/\tau_0} z^{-1}} + \frac{\sigma}{\varepsilon_0} \frac{1}{1 - z^{-1}} \right) \mathbf{E}(z), \quad (\text{A.9})$$

which can be written in the more useful form using the identity $1/(1-x) = 1 + x/(1-x)$

$$\begin{aligned} \mathbf{D}(z) &= \left(\varepsilon_\infty + \frac{(\varepsilon_s - \varepsilon_\infty)\Delta t}{\tau_0} + \frac{\sigma\Delta t}{\varepsilon_0} \right) \mathbf{E}(z) \\ &\quad + \left(\frac{(\varepsilon_s - \varepsilon_\infty)\Delta t}{\tau_0} \frac{e^{-\Delta t/\tau_0} z^{-1}}{1 - e^{-\Delta t/\tau_0} z^{-1}} + \frac{\sigma\Delta t}{\varepsilon_0} \frac{z^{-1}}{1 - z^{-1}} \right) \mathbf{E}(z), \end{aligned} \quad (\text{A.10})$$

which can be written

$$\mathbf{D}(z) = C \mathbf{E}(z) + \frac{(\varepsilon_s - \varepsilon_\infty)\Delta t}{\tau_0} \frac{e^{-\Delta t/\tau_0} z^{-1}}{1 - e^{-\Delta t/\tau_0} z^{-1}} \mathbf{E}(z) + \frac{\sigma\Delta t}{\varepsilon_0} \frac{z^{-1}}{1 - z^{-1}} \mathbf{E}(z), \quad (\text{A.11})$$

where

$$C = \varepsilon_\infty + \frac{(\varepsilon_s - \varepsilon_\infty)\Delta t}{\tau_0} + \frac{\sigma\Delta t}{\varepsilon_0}. \quad (\text{A.12})$$

It is useful to introduce two auxiliary functions $\mathbf{S}(z)$ and $\mathbf{I}(z)$ such that

$$\mathbf{D}(z) = C \mathbf{E}(z) + z^{-1} \mathbf{S}(z) + z^{-1} \mathbf{I}(z), \quad (\text{A.13})$$

where

$$\mathbf{S}(z) = \frac{(\varepsilon_s - \varepsilon_\infty)\Delta t}{\tau_0} \frac{e^{-\Delta t/\tau_0}}{1 - e^{-\Delta t/\tau_0} z^{-1}} \mathbf{E}(z), \quad (\text{A.14})$$

and

$$\mathbf{I}(z) = \frac{\sigma\Delta t}{\varepsilon_0} \frac{1}{1 - z^{-1}} \mathbf{E}(z), \quad (\text{A.15})$$

which become

$$\mathbf{S}(z) - e^{-\alpha\Delta t} z^{-1} \mathbf{S}(z) = \frac{(\varepsilon_s - \varepsilon_\infty)\Delta t}{\tau_0} \mathbf{E}(z), \quad (\text{A.16})$$

and

$$\mathbf{I}(z) - z^{-1}\mathbf{I}(z) = \frac{\sigma\Delta t}{\varepsilon_0}\mathbf{E}(z), \quad (\text{A.17})$$

respectively.

Transforming back to the discrete-time domain and using the shifting property (Eq. A.5), Eqs. A.13, A.16 and A.17 become,

$$\mathbf{E}[n] = \frac{1}{C}(\mathbf{D}[n] - \mathbf{S}[n-1] - \mathbf{I}[n-1]), \quad (\text{A.18})$$

$$\mathbf{S}[n]) = e^{-\alpha\Delta t}\mathbf{S}[n-1] + \frac{(\varepsilon_s - \varepsilon_\infty)\Delta t}{\tau_0}\mathbf{E}[n], \quad (\text{A.19})$$

$$\mathbf{I}[n] = \mathbf{I}[n-1] + \frac{\sigma\Delta t}{\varepsilon_0}\mathbf{E}[n] \quad (\text{A.20})$$

the Debye-Drude update equations in Section 2.2.3.

In order to derive Eq. A.8, the second term, denoted $f(t)$, of Eq. A.6 is considered, *i.e.*,

$$f(t) = \frac{(\varepsilon_s - \varepsilon_\infty)}{\tau_0}\Theta(t)e^{-t/\tau_0} \quad (\text{A.21})$$

The discrete-time version of this function is

$$f[n] = \frac{(\varepsilon_s - \varepsilon_\infty)}{\tau_0}\Theta[0]e^{-n\Delta t/\tau_0}, \quad (\text{A.22})$$

and the Z -transform is simply

$$f(z) = Z\{f[n]\} = \sum_{n=-\infty}^{\infty} \frac{(\varepsilon_s - \varepsilon_\infty)}{\tau_0}\Theta[0]e^{-n\Delta t/\tau_0}z^{-n}, \quad (\text{A.23})$$

which can be simplified to

$$f(z) = \frac{(\varepsilon_s - \varepsilon_\infty)}{\tau_0} \sum_{n=0}^{\infty} (e^{-\Delta t/\tau_0} z^{-1})^n. \quad (\text{A.24})$$

This is a geometric series $S = \sum_{n=0}^{\infty} x^n$ that can be summed using $S = 1/(1-x)$ to give

$$f(z) = \frac{(\varepsilon_s - \varepsilon_\infty)}{\tau_0} \frac{1}{1 - e^{-\Delta t/\tau_0} z^{-1}} \quad (\text{A.25})$$

i.e., the second term in Eq. 8. The third term in Eq. 8 can be calculated in the same manner or by taking the limit as $\tau_0 \rightarrow \infty$.